Active Infrared Nanophotonics in van der Waals Materials

Thesis by

Michelle Caroline Sherrott

In Partial Fulfillment of the Requirements for

the degree of

Doctor of Philosophy

CALIFORNIA INSTITUTE OF TECHNOLOGY

Pasadena, California

2018

Defended January 12, 2018

Michelle Caroline Sherrott
ORCID: 0000-0002-7503-9714

ACKNOWLEDGEMENTS

No thesis is ever completed without the support and input of a great number of people, and I count myself incredibly lucky to have been surrounded by an amazing group of individuals these past five years. I am so fortunate to have met the people I have met, and to be leaving this place makes me profoundly sad, if excited for a new adventure.

First and foremost, none of this would exist without the endless support of my advisor, Professor Harry Atwater. Harry is a truly unique advisor, and his unwavering enthusiasm and passion for science has been inspirational. He has challenged me to always do my best, and has provided me with the freedom to try new things, to fail, and to learn. But more than this, Harry is a kind and compassionate person. He treats his students and postdocs with respect and he always has their back. It has been a great honor to work with him.

Alongside Harry, I have a fantastic thesis committee to thank: Professor Julia Greer, who is a great teacher, whose positive energy is contagious, and who is a fantastic role model for women in science; Professor George Rossman, who exemplifies what it means to educate, and who has taught me so much about materials science, infrared spectroscopy, and doing thoughtful research; and Professor Austin Minnich, who has provided a great number of ideas and support, particularly for near-field heat transfer collaborations.

Next, I will forever be grateful to my mentor, Victor Brar, the patient postdoc who somehow turned me into a real grad student when I could barely hold a pair of tweezers. Victor, shuffling about the lab in his many-pocketed vest, was a source of never-ending ideas and insights, and pushed me to become a better scientist. I have met few people as brilliant as Victor, and I have learned so much from him.

There are so many other scientists, postdocs, and grad students that I have been fortunate to work with, listed here in no particular order. Other co-authors on the works in Chapter 2 and 3: Min Seok Jang, Seyoon Kim, Laura Kim, Josue Lopez, Luke Sweatlock. Chapter 4: Philip Hon, Juan Garcia, Sam Ponti, Kate Fountaine. Chapter 5 and 6: Will Whitney, Deep Jariwala, Wei-Hsiang Lin, Joeson Wong, Cora Went. Chapter 7: Nate Thomas. All of these individuals have taught me so much, and none of this would have happened without them. It would take pages upon pages of text to describe what they have all brought to this thesis, and to my life. Many are not just collaborators, but also wonderful friends.

Sharing an office with Will, Deep, and Joeson these past few years has been a true pleasure, and I have learned so much working and spending time with them. I also thank Matt Escarra, Naomi Coronel, and Anna Beck, my original officemates, for all they did to introduce me to Caltech and the Atwater Group.

I also want to thank all the staff members of the KNI for support, training, and friendship: Guy de Rose, Melissa Melendes, Matt Sullivan-Hunt, Nils Asplund, Steven Martinez, Bert Mendoza, Nathan Lee, Alex Wertheim, and Barry Baker. They have helped me immensely, and have made the many hours I spent in the subbasement so much more enjoyable.

So much appreciation additionally needs to be given to the incredible administrators who hold everything together: Jennifer, Tiffany, Liz, Lyann, Jonathan, and Christy. I have to especially thank Christy, who was my first point of contact with Caltech, and who made it so easy to embrace this place as my home.

Outside of scientific works, I have been so lucky in friendship here. Greg: I am so happy you were a part of this, and you brightened my day each day. My amazing friend of nearly 10 years, Dagny: words cannot express my gratitude for your friendship. Heather, my wonderful and supportive friend and roommate: I'm so happy to have met you. The entire Atwater Group: in addition to scientific support and insights, you have all been excellent friends and made me feel like I was part of a great community.

Finally, I have been endlessly supported by my family: my mom and dad who were always there with words of love and encouragement, and without whom this never would have happened; and my sister who has been one of my biggest cheerleaders.

ABSTRACT

Two-dimensional van der Waals materials have recently been introduced into the field of nanophotonics, creating opportunities to explore novel physics and realize first-of-their kind devices. By reducing the thickness of these materials, novel optical properties emerge due to the introduction of vertical quantum confinement. Unlike most materials, which suffer from a reduction in quality as they are thinned, layered van der Waals materials have naturally passivated surfaces that preserve their performance in monolayer form. Moreover, because the thickness of these materials is below typical charge carrier screening lengths, it is possible to actively control their optical properties with an external gate voltage. By combining these unique properties with the subwavelength control of light-matter interactions provided by nanophotonics, new device architectures can be realized.

In this thesis, we explore van der Waals materials for active infrared nanophotonics, focusing on monolayer graphene and few-layer black phosphorus. Chapter 2 introduces gate-tunable graphene plasmons that interact strongly with their environment and can be combined with an external cavity to reach large absorption strengths in a single atomic layer. Chapter 3 builds on this, using graphene plasmons to control the spectral character and polarization state of thermal radiation. In Chapter 4, we complete the story of actively controlling infrared light using graphene-based structures, introducing graphene into a resonant gold structure to enable active control of phase. By combining these resonant structures together into a multi-pixel array, we realize an actively tunable meta-device for active beam steering in the infrared. In Chapters 5 and 6, we present few layer black phosphorus (BP) as a novel material for active infrared nanophotonics. We study the different electro-optic effects of the material from the visible to mid-infrared. We additionally examine the polarization-dependent response of few-layer BP, observing that we can tune its optical response from being highly anisotropic to nearly isotropic in plane. Finally, Chapter 7 comments on the challenges and opportunities for graphene- and BP-integrated nanophotonic structures and devices.

PUBLISHED CONTENT AND CONTRIBUTIONS

Portions of this thesis have been drawn from the following publications with permission from the publisher:

Michelle C. Sherrott*, William S. Whitney*, Deep Jariwala, George R. Rossman, Harry A. Atwater, "Electrical Control of Linear Dichroism in Black Phosphorus from the Visible to Mid-Infrared", (***Equal author contributors)**
arXiv:1710.00131
M.C.S. and W.S.W. conceived the experiment along with co-authors, designed and fabricated the structure, and performed the measurements. The manuscript was prepared by M.C.S. and W.S.W. with input from co-authors.

Michelle C. Sherrott*, Philip W. C. Hon*****, Katherine T. Fountaine, Juan C. Garcia, Samuel M. Ponti, Victor W. Brar, Luke A. Sweatlock, Harry A. Atwater, "Experimental Demonstration of >230° Phase Modulation in Gate-Tunable Graphene-Gold Reconfigurable Mid-Infrared Metasurfaces", Nano Lett., **2017**, *17* (5), pp 3027–3034
(*Equal author contributors)
DOI: 10.1021/acs.nanolett.7b00359
M.C.S. conceived the experiment along with co-authors, designed and fabricated the structure, and participated in the measurements. The manuscript was prepared by M.C.S. with input from co-authors.

William S. Whitney*****, **Michelle C. Sherrott***, Deep Jariwala, Wei-Hsiang Lin, Hans A. Bechtel, George R. Rossman, Harry A. Atwater, "Field Effect Optoelectronic Modulation of Quantum-Confined Carriers in Black Phosphorus", *Nano Lett.*, **2017**, *17* (1), pp 78–84
(*Equal author contributors)
DOI: 10.1021/acs.nanolett.6b03362
M.C.S. and W.S.W. conceived the experiment along with co-authors, designed and fabricated the structure, and performed the measurements. The manuscript was prepared by M.C.S. and W.S.W. with input from co-authors.

Excerpts are also included from the below:

Victor W. Brar, **Michelle C. Sherrott**, Min Seok Jang, Laura Kim, Mansoo Choi, Luke A. Sweatlock, Harry A. Atwater, "Electronic modulation of infrared radiation in graphene plasmonic resonators", *Nature Communications*, **6**, 7032 (2015)
DOI: 10.1038/ncomms8032 (Open Access)
M.C.S. and V.W.B. conceived the experiment along with coauthors. M.C.S. assisted with experiments, performed calculations to analyze the experimental data, and prepared the manuscript alongside V.W.B and co-authors.

Min Seok Jang, Victor W. Brar, **Michelle C. Sherrott**, Josue J Lopez, Laura K Kim, Seyoon Kim, Mansoo Choi, Harry A. Atwater, "Tunable Large Resonant Absorption in a Mid-IR Graphene Salisbury Screen", *Phys Rev B* **90**, 165409 (2014)

DOI: 10.1103/PhysRevB.90.165409
M.C.S. assisted in data analysis and the preparation of the manuscript.

Victor W. Brar, Min Seok Jang, **Michelle Sherrott**, Seyoon Kim, Josue L. Lopez, Laura B Kim, Mansoo Choi, Harry A. Atwater, "Hybrid Surface-Phonon-Plasmon Polariton Modes in Graphene/Monolayer h-BN Heterostructures", *Nano Lett.,* **2014,** 14 (7), pp 3876 – 3880
DOI: 10.1021/nl501096s
M.C.S. performed some of the experimental characterization and assisted in data analysis and the preparation of the manuscript.

Victor W. Brar, Min Seok Jang, **Michelle Sherrott**, Josue L. Lopez, Harry A. Atwater, "Highly Confined Tunable Mid-Infrared Plasmonics in Graphene Nanoresonators", *Nano Lett., **2013***,13 (6), pp 2541-2547
DOI: 10.1021/nl400601c
M.C.S. performed some of the experimental characterization and assisted in data analysis and the preparation of the manuscript.

These manuscript excerpts are included to provide important background to the remainder of the thesis with support from advisor Professor Harry Atwater.

TABLE OF CONTENTS

LIST OF ILLUSTRATIONS

Chapter 1

INTRODUCTION

1.1 Nanophotonics

The field of nanophotonics is concerned with the nature of interactions between light and materials at a scale comparable to, or smaller than, the wavelength of light, i.e., at the nanoscale. In particular, there is a focus on controlling these interactions by nanostructuring metals, dielectrics, or semiconductors in order to realize novel functions (for example the focusing of light to very small volumes[1, 2], spectrally selective transmission or reflection[3], or the deterministic accumulation of phase[4, 5]). Modern nanophotonics seeks to control fully the complex electromagnetic field: amplitude, phase, and polarization in the near- and far-field. In this way, light can be manipulated in ways not allowed by conventional optical components, and we can replace traditional bulky optics with wavelength-scale structures. This is of great technological interest in a number of different fields: chemical sensing[6, 7], holographic displays[8], hyper-spectral imaging[9], and others, which take advantage of the ways we can control light-matter interactions at the nanoscale.

1.1.1 Plasmonics

The study of plasmons is concerned with the excitation of resonant oscillations of charge in a heavily doped material (traditionally associated with metals, but more recently expanded into heavily doped semiconductors and semimetals). A surface plasmon polariton is an electromagnetic excitation that propagates at the interface between a dielectric and a conductor, confined in the direction perpendicular to the propagation vector.[10] In the most general case, we consider propagating modes at the interface between conductors and dielectrics, which can be solved for exactly starting from Maxwell's equations, below.

$$\nabla \cdot \mathbf{D} = \rho_{ext}$$
$$\nabla \cdot \mathbf{B} = 0$$
$$\nabla \times \mathbf{E} = -\frac{\partial \mathbf{B}}{\partial t} \qquad (1.1a\text{-}d)$$
$$\nabla \times \mathbf{H} = \mathbf{J}_{ext} + \frac{\partial \mathbf{D}}{\partial t}$$

These equations link the four macroscopic fields – **D** (the dielectric displacement), **E** (the electric field), **H** (the magnetic field), and **B** (the magnetic induction) – with charge carrier density ρ_{ext} and current density $\mathbf{J}_{ext}$. We can then write down additional relationships to polarization, **P**, and magnetization, **M**, defined in regards to the permittivity and permeability of free space, ε_0 and μ_0, respectively.

$$\mathbf{D} = \varepsilon_0 \mathbf{E} + \mathbf{P} = \varepsilon \varepsilon_0 \mathbf{E} \qquad (1.2a,b)$$
$$\mathbf{H} = \frac{1}{\mu_0}\mathbf{B} - \mathbf{M} = \frac{\mathbf{B}}{\mu_0 \mu}$$

where we assume non-magnetic, linear, isotropic media with relative permittivity ε and permeability μ (and from here onwards ignore the magnetic response). The full derivation is omitted here for conciseness, but instead we write down the main governing equation that is drawn from Maxwell's equations in the absence of external charge and current, the *wave equation*:

$$\nabla \times \nabla \times \mathbf{E} = -\mu_0 \frac{\partial^2 \mathbf{D}}{\partial t^2} \qquad (1.3a,b)$$
$$\mathbf{K}(\mathbf{K} \cdot \mathbf{E}) - K^2 \mathbf{E} = -\varepsilon(\mathbf{K}, \omega)\frac{\omega^2}{c^2}\mathbf{E}$$

in the time and momentum domains, respectively. This can be simplified to the key governing equation of propagating waves by using a few mathematical identities and setting a permittivity ε that is invariable with position:

$$\nabla^2 \mathbf{E} - \frac{\varepsilon}{c^2}\frac{\partial^2 \mathbf{E}}{\partial t^2} = 0 \qquad (1.4)$$

From here, if we assume a harmonic time dependence of the electric field

$\mathbf{E}(\mathbf{r},t) = \mathbf{E}(\mathbf{r})e^{-i\omega t}$, we arrive at the *Helmholtz equation*:

$$\nabla^2\mathbf{E} + k_0^2\varepsilon\mathbf{E} = 0 \tag{1.5}$$

where k_0 is the wave vector of a propagating wave in vacuum, $k_0 = \omega/c$. From this equation, applying appropriate boundary conditions at material interfaces (and using Maxwell's equations where needed), the fundamental properties of propagating plasmons for numerous geometries can be defined. Most importantly, this allows us to define the dispersion relation for surface plasmon polaritons (SPPs); the relationship between frequency ω and wavevector k based on the geometry and permittivity of the conductive medium and surrounding dielectric. And indeed, a very interesting and powerful aspect of the study of nanophotonics is that all of the complex structures we explore can be fully described by Maxwell's equations: commercial software packages self-consistently solve these equations at different points in space (and sometimes time), and analytic solutions for the optical response of a wide variety of geometries can be derived. This allows us to design nanophotonic structures with incredible precision.

An example of relevance is plotted below, adapted from an exercise presented in S. Maier, *Plasmonics: Fundamentals and Applications*[10], considering the case of an insulator-metal-insulator stack. This geometry is of particular relevance in the ultrathin limit for the discussion of plasmons in two-dimensional materials, as will be elaborated on later. We note the presence of odd and even modes as different solutions to the above equations, wherein the confinement of modes behaves differently as a function of thickness. For even modes, the confinement factor increases dramatically as the metal layer thickness decreases, and the mode remains allowed, a feature that becomes particularly interesting in the zero-thickness limit of 2D materials.

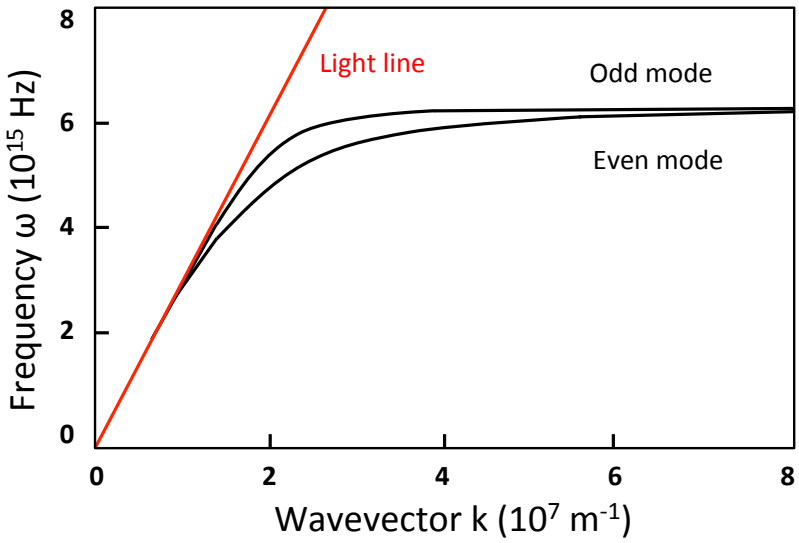

Figure 1.1: Dispersion relation of the coupled odd and even modes for an air/silver/air multilayer with a metal core of thickness 50 nm. Silver is modeled as a Drude metal with negligible damping. Modeled after [6].

While the formal derivation of plasmons in 2D materials will follow a slightly modified approach, this shows us the nature of the plasmons that we observe in the ultrathin limit, in particular the large momentum mismatch with respect to the light line and resulting large confinement factor. This confinement factor is one of the unique features of plasmons: whereas bulk optical components are restricted in how much they can focus light by the diffraction limit, plasmonic materials can squeeze light down into extremely small volumes, with interesting implications for enhancing the strength of light-matter interactions under high field strengths.

1.1.2 Metasurfaces

Since the year 2011, subwavelength nanophotonic structures have been employed to expand how we write Snell's Law, classically written as below:

$$\frac{\sin\theta_1}{\sin\theta_2} = \frac{v_1}{v_2} = \frac{\lambda_1}{\lambda_2} = \frac{n_2}{n_1} \tag{1.6}$$

where $\theta_{1,2}$ are the incident and refracted angle of propagation of light, $v_{1,2}$ are the speed of light in each medium 1, 2, $\lambda_{1,2}$ are the wavelengths of light in each medium, and $n_{1,2}$ are the refractive indices of the media, illustrated in Figure 1.2:

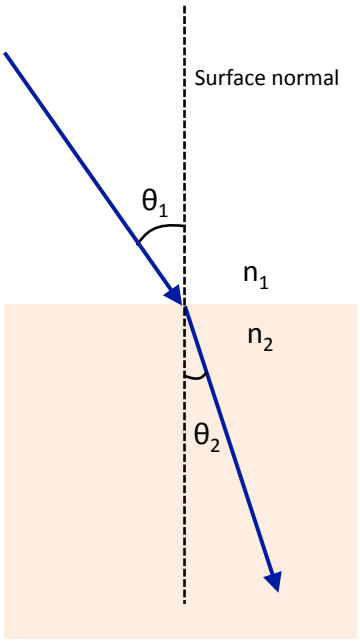

Figure 1.2: Schematic illustration of Snell's law for refracted light passing from medium 1 to medium 2.

By incorporating a phase gradient at an interface, we rewrite this equation to account for the accumulated phase as a function of position. This yields the generalized law of refraction (1.7) and reflection (1.8).

$$n_t \sin(\theta_t) - n_i \sin(\theta_i) = \frac{1}{k_0}\frac{d\Phi}{dx}$$
$$\cos(\theta_t)\sin(\varphi_t) = \frac{1}{n_t k_0}\frac{d\Phi}{dy} \tag{1.7}$$

$$\sin(\theta_r) - \sin(\theta_i) = \frac{1}{n_i k_0}\frac{d\Phi}{dx}$$
$$\cos(\theta_r)\sin(\varphi_r) = \frac{1}{n_t k_0}\frac{d\Phi}{dy} \tag{1.8}$$

where $d\Phi/dx$ and $d\Phi/dy$ are phase gradients in the x and y dimensions, $\theta_{i,t,r}$ are the incident, transmitted, and reflected angles in the x dimension, and $\phi_{t,r}$ are the transmitted and reflected angles along the y dimension, where the light has been reflected/refracted away from the incident plane (defined as the x-z plane here).[11] In this way, light can be redirected in the far-field in almost arbitrary ways, as long as we have access to a full 2π (360°) phase range in continuous increments. By carefully selecting the accumulated phase as well as polarization at each position on the metasurface, far-field beam profiles can be generated at will (we are not bounded to simply reflecting/refracting light to different angles as written in equations 1.7 and 1.8). This has been taken advantage of for applications including anomalous reflection and refraction, focusing/lensing[4, 5], and more complex functionalities such as polarization conversion, cloaking, and three-dimensional image reconstruction[12-16], among others[11, 17-21].

In order to realize this 'designer' phase gradient, resonant nanophotonic elements are required. By controlling the geometry of the element, different scattered phases are realized. In the seminal work from Yu et al[11], v-shaped metallic structures are used, which result in different phases of light based on the angle between arms of the resonator. This can be generalized as shown in Figure 1.3, below: by changing the geometry of the resonant element (which can be plasmonic or dielectric) as well as its surroundings (which will be the focus of our work), different phases can be achieved[20, 22-24].

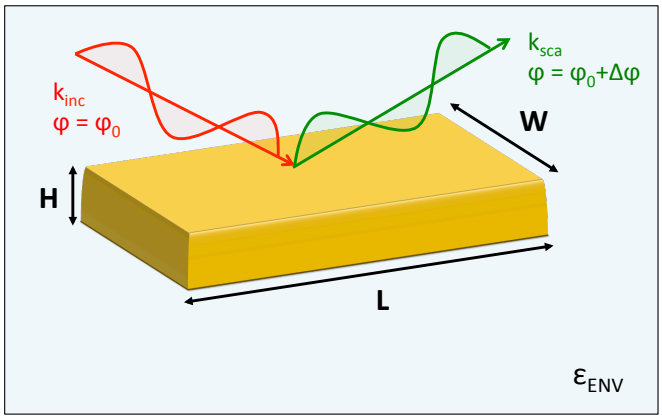

Figure 1.3: Metasurface element: By controlling the geometric parameters and dielectric environment of a resonant antenna, the reflected or transmitted phase of light can be controlled. The interference between each scattering element then results in a propagating wavefront that has been redirected.

These elements can then be arrayed together as desired to control propagating phase fronts. This can therefore be used to create wavelength-scale thickness versions of bulk optical components, and additionally enables the possibility of realizing novel functions that are otherwise challenging or impossible. In this thesis, we take advantage of actively tunable materials to control the reflected phase from a resonant element and array these together to design a reconfigurable metasurface.

1.2 van der Waals Materials

Van der Waals materials are a class of materials defined by a strong in-plane bonding character, and weak (van der Waals) out of plane interactions between layers. These have attracted a substantial amount of attention in recent years because their weak van der Waals interactions allow for the isolation of individual atomic layers, which are naturally passivated and therefore stable in the ultrathin limit. Early studies of these materials have been done by mechanically exfoliating bulk crystals down to ultrathin and even monolayer thicknesses. Using Scotch tape, layers of the material are sequentially removed, leaving behind ultrathin samples that are then 'stamped' onto a substrate of choice. In this way, research has been performed on a wide range of ultrathin van der Waals materials, enabled by this straightforward experimental methodology. In this thesis, we focus on the optical response of monolayer graphene and few-layer black phosphorus.

1.2.1 Graphene

Discovered experimentally in 2004 by Nobel laureates Andre Geim and Konstantin Novoselov, graphene is a monolayer of sp^2-bonded carbon atoms arranged in a honeycomb lattice (a three-fold symmetric lattice composed of a two-atom basis, shown below)[25, 26].

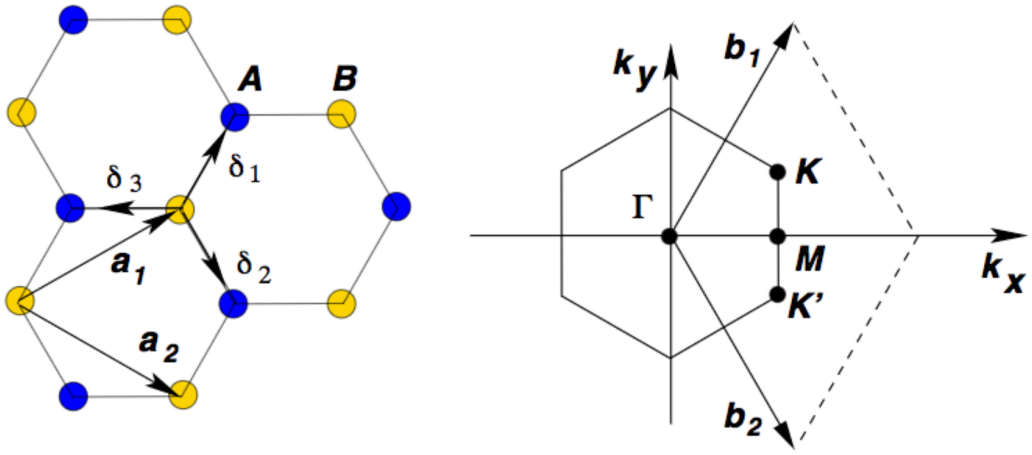

Figure 1.4: Honeycomb lattice of graphene with two atoms per unit, A and B, defined by lattice vectors $\mathbf{a_1}$ and $\mathbf{a_2}$ and with nearest neighbor vectors δ_i, i = 1,2,3. Corresponding Brillouin Zone. Dirac points are located at the K and K' points. Adapted from [27].

Due to its unique atomic structure, it possesses exotic optical, electronic, thermal, and mechanical properties, all of which have been studied extensively in recent years[25, 28, 29]. It is also completely stable in monolayer form, giving researchers new opportunities for understanding physics at the atomic scale. The most unique feature of monolayer graphene in the context of this work is its band structure, which about the k and k' point in the low-energy limit is linear, $E \propto |k|$.

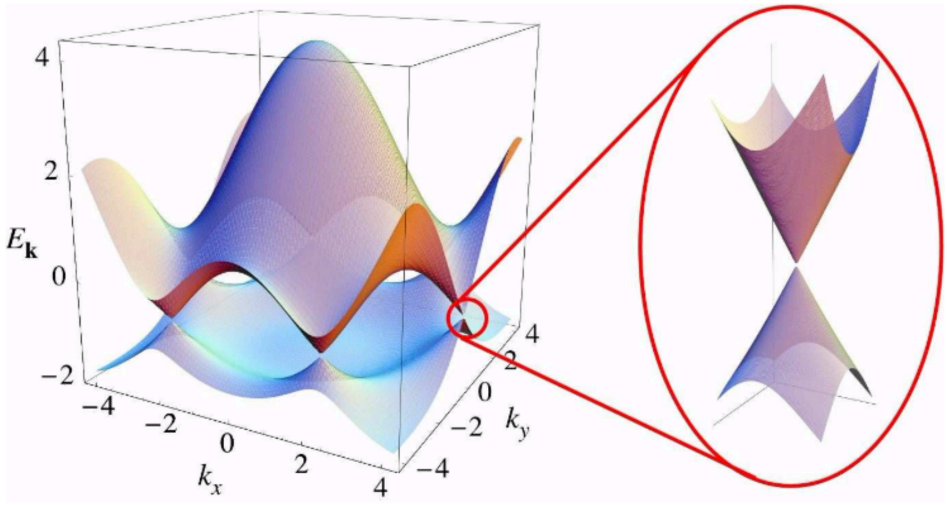

Figure 1.5: Calculated band structure of graphene, from [27], with linear dispersion near the K point highlighted.

Correspondingly, the charge carriers are characterized at massless Dirac fermions. This results in the unique plasmon dispersion that has been studied in this thesis. We adapt the formalism developed in ref [30] to model the optical response of monolayer graphene. Plasmonic modes are identified by inserting the graphene between two dielectric layers at x = 0, assuming the electric field is of the form:

$$E_z = Ae^{ikz-K_1x},\ E_y = 0,\ E_x = Be^{ikz-K_1x},\ for\ x>0$$
$$E_z = Ce^{ikz+K_2x},\ E_y = 0,\ E_x = De^{ikz+K_2x},\ for\ x<0 \qquad (1.9a,b)$$

and inserting these into Maxwell's equations and matching the boundary conditions. We use the surface conductance of graphene σ(ω,k) to define the boundary at x = 0. This gives us the dispersion relation

$$\frac{\varepsilon_{r1}}{\sqrt{k^2-\frac{\varepsilon_{r1}\omega^2}{c^2}}}+\frac{\varepsilon_{r2}}{\sqrt{k^2-\frac{\varepsilon_{r2}\omega^2}{c^2}}}=\frac{\sigma(\omega,k)i}{\omega\varepsilon_0} \qquad (1.10)$$

which simplifies in the limit of k>>ω/c to

$$k \approx \varepsilon_0 \frac{\varepsilon_{r1} + \varepsilon_{r2}}{2} \frac{2i\omega}{\sigma(\omega,k)} \tag{1.11}$$

where ε_{r1} and ε_{r2} are the optical frequency permittivity of the materials above and below the graphene sheet, k is the momentum vector of light, ω the frequency, c the speed of light, and σ the 2D optical conductivity of the graphene.

By utilizing the methods described by Falkovsky in "the Optical Properties of Graphene"[31, 32], we can define the intra- and interband contributions to the optical conductivity of graphene, which we sum in order to fully describe the material response. The intraband contribution is expressed as:

$$\sigma^{\text{intra}}(\omega) = \frac{2ie^2T}{\pi\hbar(\omega + i\tau^{-1})} \ln[2\cosh(\mu / 2T)] \tag{1.12}$$

which takes the form:

$$\sigma^{\text{intra}}(\omega) = \frac{ie^2|\mu|}{\pi\hbar(\omega + i\tau^{-1})} \tag{1.13}$$

for $\mu >> T$. The second component, the interband contribution, is presented as a step function wherein transitions below $2\mu = 2E_F$ are Pauli-blocked and above result in an optical absorption characteristic of the linear band structure. This is explicitly written as:

$$\sigma^{\text{inter}}(\omega) = \frac{e^2}{4\hbar}\left[\theta(\omega - 2\mu) - \frac{i}{2\pi}\ln\frac{(\omega + 2\mu)^2}{(\omega - 2\mu)^2}\right] \tag{1.14}$$

where we introduce τ the characteristic scattering time of the carriers, and $\theta(\omega-2\mu)$ is a step function defied by the chemical potential μ of the graphene. It is particularly of note that the optical conductivity depends strongly on the graphene Fermi energy, indicating a plasmon dispersion that can be tuned with this parameter. Because graphene is a single atomic layer thick, we can use an external gate voltage to modulate its carrier concentration and therefore its optical response. This provides us with new opportunities for realizing

actively tunable plasmonics, as the short screening length and high carrier concentration in bulk plasmonic materials prevents the use of an electric field for modulating this response. By inserting these optical conductivities into the analytic expression 1.11 above, or into full-wave simulations, we can accurately map out the plasmon resonances of graphene as a function of wavelength and of Fermi energy with excellent agreement to experiment.

1.2.2 Black Phosphorus

A newer addition to the 2D materials family, black phosphorus (BP) is the layered allotrope of phosphorus, possessing a buckled lattice structure that is nominally stable under ambient conditions.[33] However, due to the relatively weak in-plane bonding character of the material, it is highly sensitive to oxidation and degradation, requiring encapsulation for device fabrication.

Unlike graphene, with its linear band structure, black phosphorus is a direct band gap semiconductor. By varying the number of layers of BP, the change in quantum confinement in the vertical direction widely tunes the band gap energy. In monolayer form, BP has a band gap of approximately 2 eV, which steadily decreases to the bulk value of 0.3 eV as more layers are added. Unlike transition metal dichalcogenides (TMDCs), which undergo a direct-to-indirect band gap transition from monolayer to bilayer, the band gap remains direct at all thicknesses.

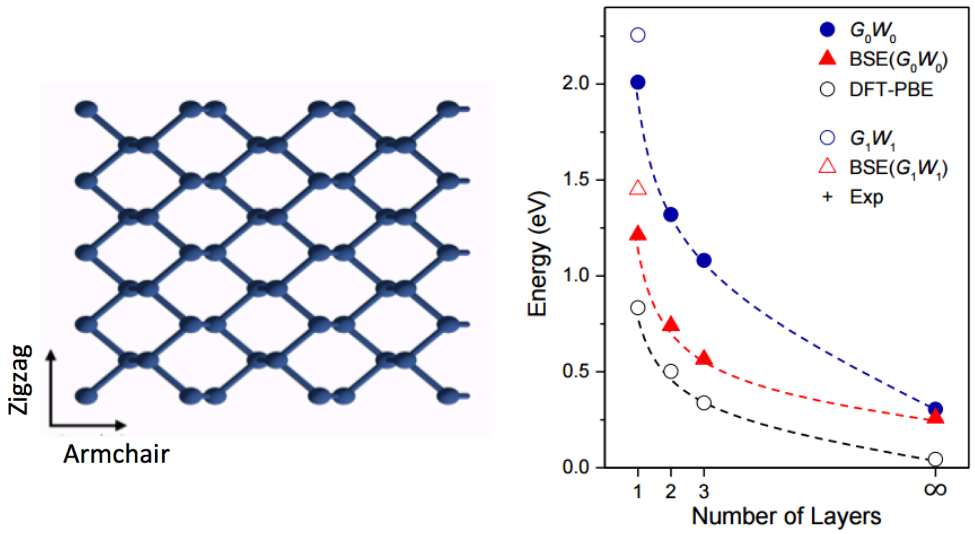

Figure 1.6: Lattice structure of black phosphorus (left). Calculated electronic band gap of black phosphorus as a function of number of layers (right, from [34].)

Black phosphorus is a particularly promising material system for study, then, because it spans the gap between graphene, a material of greatest relevance in the mid-to-far infrared, and TMDCs, semiconducting van der Waals materials with band gaps in the visible. While it does not have the very high electronic mobility of graphene, it has favorable transport properties with typical mobilities observed in experiments of a few hundred $cm^2\ V^{-1}\ s^{-1}$, making it of interest for optoelectronic devices.

In addition to this, BP's in-plane structural anisotropy makes it a unique materials system for taking advantage of materials properties that vary with crystal direction. This impacts its thermal, mechanical, electrical, and optical properties[34]. It can be thought of as a naturally occurring quantum well, with the additional interesting feature of large in-plane anisotropy, something not seen in any other materials. This suggests that electro-optic effects typically seen in III-V quantum wells, such as the quantum-confined Stark effect[35], should be observed in BP, with different consequences along each crystallographic direction. Because BP can be easily exfoliated from bulk crystals, and van der Waals materials can be integrated into devices without lattice-matching constraints or the need for

ultra-high vacuum growth chambers, this may be a promising material for future electro-optic modulator devices.

1.3 The Scope of this Thesis

This thesis explores the intersection of the two topics identified above: van der Waals materials and nanophotonics. By taking advantage of the unique properties of quantum-confined, ultrathin, layered materials, we introduce new functions into existing nanophotonic designs as well as exploring the unique physics that emerge in the monolayer limit. We use plasmonic nanostructures to focus infrared light into small volumes, enabling strong light-matter interactions as the nanoscale. This not only allows use to incorporate ultrathin materials for electrically tunable structures, but also introduces new types of coupled quasiparticles not typically observed in bulk materials.

Chapter 2 of this thesis introduces highly confined, electrically tunable graphene plasmons in nanoresonators. We observe record-breaking confinement factors in nanostructured monolayer graphene, and utilize an external gate voltage to tune this across the mid-infrared, also introducing tunable coupling between plasmons and phonon-polaritons of another monolayer material, hexagonal boron nitride (h-BN). We also introduce an external cavity structure for enhancing the light-matter interactions in a monolayer material. Chapter 3 presents work on utilizing graphene plasmons to actively modulate the amplitude and polarization state of thermal radiation. Due to the reciprocity between absorptivity and emissivity dictated by Kirchoff's Law, we tune the emissivity of our graphene structures, something that is typically thought of as a fixed materials property. Chapter 4 builds on the ways in which graphene can be used to actively control infrared light by integrating it into a different type of resonant geometry to modulate reflected phase and realize a reconfigurable meta-device for beam steering. In this way, we complete the graphene 'tool-kit' for control of infrared light.

Chapters 5 and 6 focus on the electro-optic effects in few layer black phosphorus (BP). In Chapter 5, the different mechanisms for the tunable optical response of BP which result from its narrow band gap and quantum well electronic structure are identified. From this,

we suggest the black phosphorus is a promising material for actively tunable infrared nanophotonics. In Chapter 6, we build on this work, carefully separating the different contributions to this tunability and their influence on the polarization-dependent optical response of BP. We observe that this anisotropic tunability is present from the visible to mid-infrared, something not seen in conventional electro-optic materials.

Finally, in Chapter 7 we discuss the outlook for the emerging field of van der Waals nanophotonics. We comment on promising research directions for graphene-integrated structures, including extensions of controlling thermal emission in the near- and far-field, and the possibility of taking advantage of the fast response time of graphene plasmons to detect chemical species as they are evolved. We also propose novel nanophotonic designs that take advantage of the unique optical properties of few-layer black phosphorus. While more fundamental studies of BP are still needed to design such structures, we suggest that by taking advantage of the in-plane optical anisotropy, steering of propagating waves and control of reflected polarization may be realized.

Detailed experimental methods for these works are described in the Appendix.

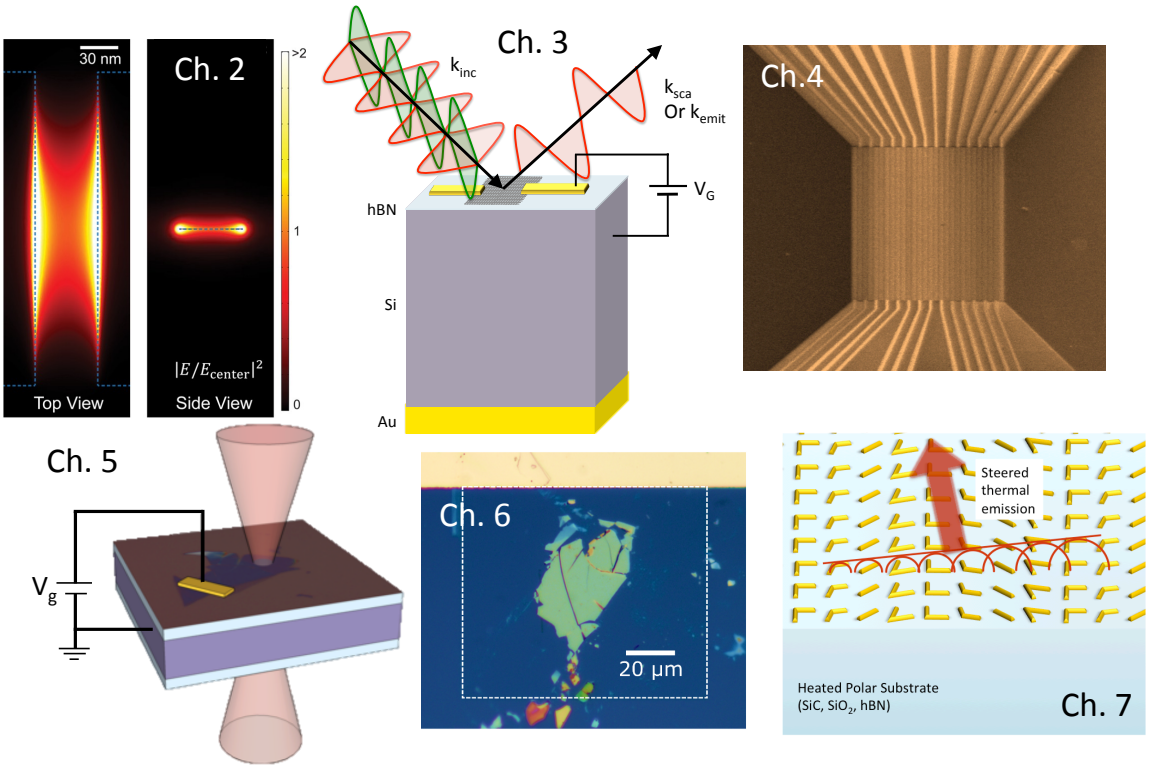

Figure 1.7: A pictorial representation of this thesis. Chapter 2 presents tightly confined graphene plasmons. Chapter 3 discusses control of the amplitude and polarization of thermal emission. Chapter 4 introduces a gate-tunable graphene-gold metasurface for active beam steering. Chapter 5 examines the electro-optic effects in few-layer black phosphorus, and Chapter 6 extends this to the polarization-dependent tunable optical response from the visible to mid-infrared. Chapter 7 proposes future experiments based on graphene and black phosphorus, including the steering of thermal radiation.

C h a p t e r 2

GRAPHENE PLASMONS FOR TUNABLE LIGHT-MATTER INTERACTIONS

"Graphene is dead; long live graphene"

– Andre Geim (Nobel Laureate who discovered graphene)

"When one dares to try, rewards are not guaranteed, but at least it is an adventure"

– (Also) Andre Geim

Single-layer graphene has been shown to have intriguing prospects as a plasmonic material, as modes having plasmon wavelengths ~20 times smaller than free space ($\lambda_p \sim \lambda_0/20$) have been observed in the 2−6 THz range, and active graphene plasmonic devices operating in that regime have been explored. However there is great interest in understanding the properties of graphene plasmons across the infrared spectrum, where applications in thermal radiation and molecular sensing are very interesting. We use infrared microscopy to observe the modes of tunable plasmonic graphene nanoresonator arrays as small as 15 nm. We map the wavevector-dependent dispersion relations for graphene plasmons at mid-infrared energies from measurements of resonant frequency changes with nanoresonator width. By tuning resonator width and charge density, we probe graphene plasmons with $\lambda_p \leq \lambda_0/100$ and plasmon resonances as high as 310 meV (2500 cm^{-1}, 4 μm) for 15 nm nanoresonators. Electromagnetic calculations suggest that the confined plasmonic modes have a local density of optical states more than 10^6 larger than free space (a record at the time) and thus could strongly increase light-matter interactions at infrared energies. We take advantage of this enhancement of light-matter interactions to observe semi-classical strong coupling between graphene and another monolayer material, hexagonal boron nitride (h-BN), which supports a surface phonon polariton in the mid-infrared. We then fabricate graphene resonators on an external cavity (a quarter-wavelength thick dielectric resonator) to enhance its absorption up to 25%, an improvement of a factor of 10.

2.1 Highly Confined Tunable Mid-Infrared Plasmonics in Graphene Nanoresonators

2.1.1 Introduction

Surface plasmon polaritons (SPPs) are optical modes consisting of a decaying evanescent wave in a dielectric coupled to an oscillating wave of surface charge (i.e., a surface plasmon) on the surface of a conductor.[36] These modes have remarkable properties including large wavelength reductions relative to free space, and optical dispersion relations that can be engineered via metal/dielectric nanoarchitectural design. Such properties have led to interest in using SPPs for on-chip optical signal routing, visible frequency metamaterials, and as a means of increasing light-matter interactions.[37, 38] While much progress has been made in achieving these goals, the use of metals as plasmonic materials has limited the capabilities of the devices. Noble metal films and nanostructures exhibit high losses due to low carrier mobilities, surface roughness, grain micro-structure and impurities,[39] and the large electronic density of states in metals restricts the possibility of dynamically tuning the plasmon energy via externally applied electrostatic fields. These limitations have led to a search for alternative plasmonic materials, including transparent conducting oxides, transition metal nitrides, superconductors, and graphene.[40, 41]

Single layer graphene has interesting prospects as a plasmonic material, as discussed in Chapter 1. It has been shown theoretically and experimentally that SPPs excited in finite thickness metal films embedded in dielectrics or metal-clad dielectric slots display smaller mode volumes as the middle layer becomes thinner.[42-48] A single atomic layer of material, such as graphene, represents the ultimate limit of this trend, and theoretical predictions have shown that the mode volumes of SPPs in graphene can be 10^6 times smaller than those in free space.[49-51] Furthermore, the optical properties of graphene can be dynamically tuned by chemical or electrostatic changes to the charge density of the graphene sheet.[51, 52] This allows for the creation of SPP-based devices that can be effectively turned on and off or tuned to be active at different wavelengths. Such devices have recently been demonstrated in the THz regime on graphene samples patterned at micrometer length scales, demonstrating plasmonic wavelengths ~20 times smaller than free space (λ_p ~

$\lambda_0/20$) and 0.3 decades of tunability in the 2−6 THz range[53-55]. In the infrared regime some progress has also been made in imagining plasmons using 10 μm wavelength scattering NSOM techniques, revealing graphene plasmons 50−60 times smaller than the free space wavelength[56, 57], and very recently graphene nanostructures with ion gel top gates on indium tin oxide substrates were investigated in the mid- infrared regime.[58] However, there is still great interest in understanding the properties of graphene plasmons across the infrared spectrum. Some theoretical work has predicted that graphene plasmons in the infrared should display long lifetimes and high mode confinement,[50] while another work has predicted that graphene is too lossy to exhibit strong plasmonic properties in the mid-infrared, especially at energies above the 200 meV optical phonon energy of graphene.[41]

In this work we use infrared microscopy to measure the plasmon resonances of graphene nanoresonator arrays patterned down to 15 nm length scales on a back-gated graphene device. By probing how the resonant frequency changes with nanoresonator width, we are able to map the wavevector-dependent dispersion relations of graphene plasmons in the mid-infrared regime. We further show how the graphene plasmon dispersion relation changes as the charge density is continuously varied, and we find that the mode volume, intensity, and frequency of plasmon modes depend strongly on the graphene charge density. By tuning these parameters (nanoresonator width and charge density) we create and probe plasmons in graphene with $\lambda_p \leq \lambda_0/100$, and resonant energies as high as 310 meV (2500 cm^{-1}, 4 μm) for 15 nm nanoresonators. By comparing our results to finite element electromagnetic simulations, we find that these confined plasmonic modes have mode densities more than 10^6 larger than free space and thus could serve and an effective means for increased light−matter interactions. Finally, we observe additional and unexpected resonances in the graphene nano- resonator spectrum around 110 meV (900 cm^{-1}, 11.1 μm). These features can be effectively modeled as surface plasmon phonon polaritons (SPPPs),[59, 60] new fundamental excitations that arise due to strong coupling between the graphene plasmons and the optical phonons of the SiO_2 substrate.

2.1.2 Experimental Measurement of Tunable Infrared Graphene Plasmons

A schematic of our experimental setup is shown in Figure 1a. Our measurements were performed on graphene grown on 25 μm thick copper foil using established chemical vapor deposition (CVD) growth techniques.[61, 62] After being transferred to SiO_2/Si wafers, nanoresonator arrays were patterned in the graphene using 100 keV electron beam lithography in PMMA followed by an oxygen plasma etch. Fabrication techniques are described in depth in Appendix A. Using this process we were able to fabricate graphene nanoresonators over 80 × 80 μm^2 areas with widths varying from 80 nm to 15 nm. These large area samples are required for measurements performed in a Fourier Transform Infrared (FTIR) microscope, and are made possible by the use of CVD graphene sheets. The aspect ratio of the nanoresonators was 5−8:1 and the period was 2−3 × (width). Figure 2.1b shows scanning electron microscope (SEM) and atomic force microscope (AFM) images of the graphene nanoresonators after fabrication. A typical gate- dependent resistance curve for one of our devices is shown in Figure 2.1c. The peak in the resistance corresponds to the charge neutral point (CNP) of the graphene, when the Fermi level is aligned with the Dirac point and the carrier density is minimized.[63] After the CNP for each device was measured, a capacitor model was used to determine the Fermi level position for each applied gate voltage.

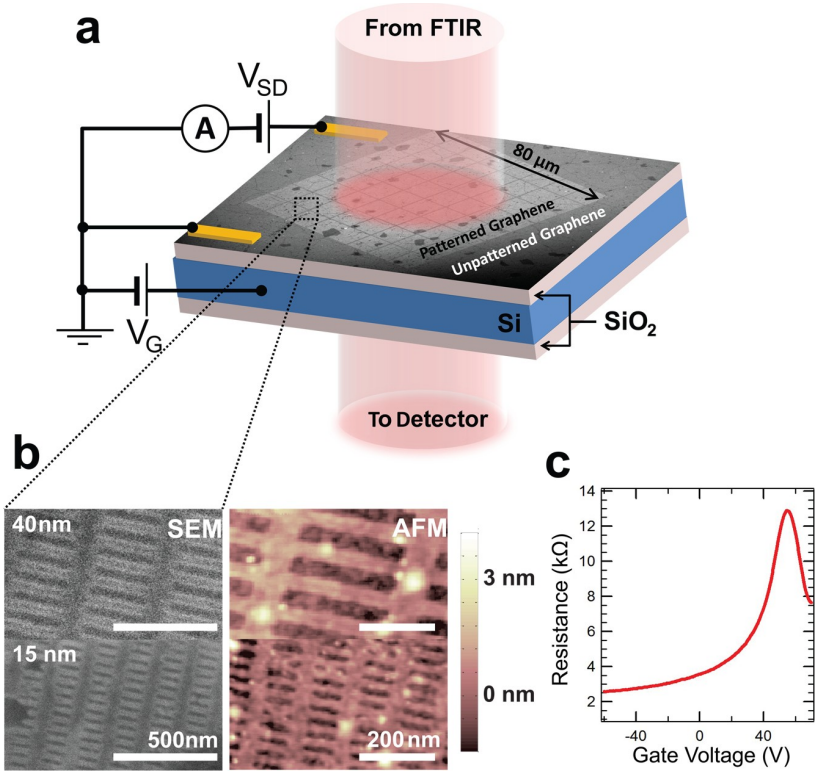

Figure 2.1: Schematic of experimental device. (a) SEM image of a 80 × 80 um^2 graphene nanoresonator array etched in a continuous sheet of CVD graphene. The graphene sheet was grounded through Au(100 nm)/Cr(3 nm) electrodes that also served as source−drain contacts, allowing for in situ measurements of the graphene sheet conductivity. A gate bias was applied through the 285 nm SiO_2 layer between the graphene sheet and the doped Si wafer (500 um thick). FTIR transmission measurements were taken over a 50 μm diameter spot. (b) SEM and AFM images of 40 and 15 nm graphene nanoresonator arrays. A nanoresonator width uncertainty of ±2 nm was inferred from the AFM measurements. (c) A resistance vs gate voltage curve of the graphene sheet showing a peak in the resistance at the charge neutral point (CNP), when the Fermi level (E_F) is aligned with the Dirac point.

Transmission measurements were done in an FTIR microscope using a 50 μm diameter spot size and with light polarized perpendicular to the graphene nanoresonators. In order to probe carrier-dependent optical properties of the graphene nanoresonators all spectra were normalized to spectra taken at the charge neutral point, isolating the plasmonic response of the graphene. Figure 2.2a shows normalized spectra taken from nanoresonator arrays with widths varying from 80 to 15 nm while the Fermi level is held at −0.37 eV, corresponding to a carrier density of 8.8 × 10^{12} holes per cm^2. These spectra contain two different types of features. The first is a surface plasmon phonon polaritons, labeled SPPP, which is a sharp

resonance that appears near 0.12eV for the 80 nm and 50 nm nanoresonators but is not visible for nanoresonators with widths <40 nm. The second feature is the graphene plasmon, labeled GP, which is a broader peak that appears for all nanoresonator widths. As the width of the nanoresonators is decreased, the energy and width of the GP peak increase, while the intensity of this feature decreases. For example, for 80 nm nanoresonators this feature appears as a narrow peak at 0.16 eV, while for 15 nm nanoresonators it appears as a very weak and broad peak at 0.29 eV.

To better understand the origin of these two features, we monitored how they changed as we varied the carrier density of the graphene sheet. Figure 2.2b shows a series of spectra taken in this manner from 50 nm nanoresonator arrays. For low carrier densities, when E_F is only 0.22 eV below the Dirac point, both SPPP and GP peaks appear very weakly in the nanoresonator spectrum, at 0.114 and 0.166 eV, respectively. As more carriers are added to the graphene sheet, both SPPP and GP peaks gain intensity and shift to higher frequencies, with the SPPP and GP reaching 0.126 and 0.203 eV, respectively, when E_F is increased to 0.52 eV below the Dirac point. In Figure 2.3a we plot the SPPP and GP peak energies for all nanoresonator widths as a function of E_F. Here we observe that the energy of the GP feature shows a stronger dependence on carrier density for smaller nanoresonator widths.

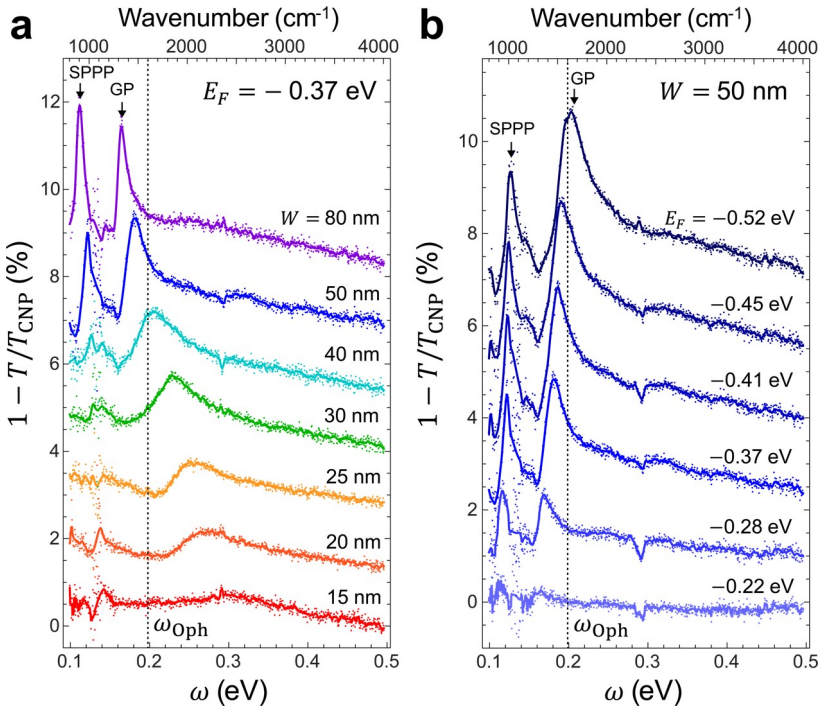

Figure 2.2: Gate-induced modulation of transmission through graphene nanoresonator arrays normalized to transmission spectra obtained at the CNP. (a) Width dependence of optical transmission through graphene nanoresonator arrays with $E_F = -0.37$ eV. The width of the nanoresonators is varied from 15 to 80 nm. (b) Fermi level dependence of optical transmission through 50 nm wide graphene nanoresonators, with E_F varying from −0.22 to −0.52 eV. The dotted vertical line in both (a) and (b) indicates the zone-center energy of the in-plane optical phonons of graphene.

2.1.3 Theoretical Description of Graphene Plasmons

These two experimentally observed resonances can be understood using a simple Fabry−Perot model of plasmons bound in graphene nanoresonators patterned on SiO_2. When incident light is coupled to a graphene plasmon mode of the wavevector k_p, the plasmon undergoes multiple reflections between the two edges of the nanoresonator. Constructive interference occurs when the reflected plasmons are in phase, which occurs when $2\,\mathrm{Re}(k_p)W + 2\phi = 2m\pi$, where W is the width of the nanoresonator and ϕ is the phase shift of the plasmons upon reflection. We estimated ϕ by performing electromagnetic simulations using a finite element method and for the first-order resonance ($m = 1$), ϕ is calculated to be 0.30π to 0.35π depending on the width to period ratio. This implies that the plasmon wavelength $\lambda_p = 2\pi/\mathrm{Re}(k_p)$ is almost three times that of the nanoresonator width.

Interestingly, we note that ϕ is scale-invariant, as long as the system is in the electrostatic limit ($k_p \gg \omega_p/c$).[64] Recognizing that the wavevector k_p can be approximated as $i\varepsilon\omega_p/[2\pi\sigma(\omega_p)]$ in the electrostatic limit[15], the condition for the first-order plasmon resonance is reduced to:

$$\frac{\omega_p W}{2\pi}\mathrm{Im}\left\{-\frac{\varepsilon(\omega_p)}{\sigma(\omega_p)}\right\} = \pi - \phi \tag{2.1}$$

Here, $\varepsilon(\omega) = (1 + \varepsilon_{SiO_2}(\omega))/2$ is the average dielectric function of the air−SiO_2 interface. In our calculations, we used an analytic expression for the graphene conductivity $\sigma(\omega)$ evaluated within the local random phase approximation,[65] and the complex dielectric function of SiO_2, $\varepsilon_{SiO_2}(\omega)$, was taken from Palik[66]. Upon solving eq 2.1 we find that for some graphene nanoresonator widths multiple first-order plasmon modes can be supported. This effect is due to the dispersive permittivity of SiO_2, which varies greatly near its transverse optical phonon at 0.13 eV. This results in two separate bands in the graphene/SiO_2 plasmon dispersion relation, both of which can create plasmon resonances in the patterned graphene. In Figure 2.3a we plot as solid and dashed lines the resonant energies of these two modes for different nanoresonator widths and E_F values, showing that one of the modes (solid line) has a width and carrier density dependence that correlates well with the GP feature, while the other mode (dashed line) behaves like the SPPP feature. We note that, in principle, there can be a third solution to eq 2.1 that would occur almost right at the SiO_2 phonon energy; however, this mode is heavily damped by the substrate lattice oscillations.

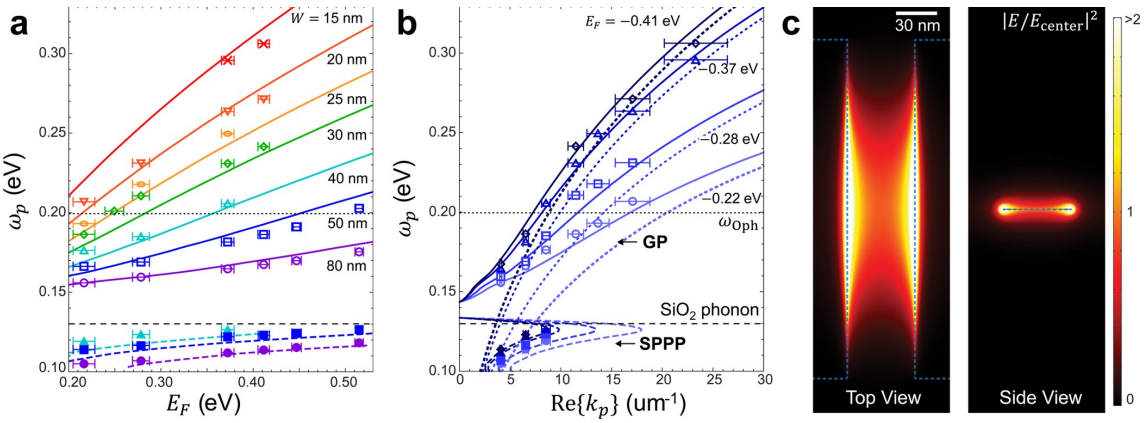

Figure 2.3: Dispersion of GP and SPPP plasmonic resonances in graphene nanoresonator arrays. (a) Fermi level dependence of the measured energy of "GP" (open colored symbols) and "SPPP" (filled colored symbols) features observed in nanoresonators with varying widths. Solid and dashed colored lines indicate the two solutions to eq. 2.1 using the same experimental widths and continuously varying E_F. (b) Theoretical dispersion of bare graphene/SiO_2 plasmons (solid) and SPPPs (dashed), for different E_F values. Open and filled symbols plot the measured energy of "GP" and "SPPP" features (respectively) from graphene nanoresonators at equivalent E_F values. Wavevector values for experimental points are obtained from AFM measurements of the nanoresonator widths followed by a finite elements simulation to calculated the wavelength of the first order supported plasmon modes. The dotted blue lines indicate the theoretical plasmon dispersion of graphene on a generic, nondispersive dielectric with $\varepsilon_\infty = 2.1$, which is the high frequency permittivity of SiO_2. Dashed and dotted black lines in (a) and (b) indicate the energy of the TO optical phonon of SiO_2 and the zone-center energy of the in-plane optical phonons of graphene, respectively. (c) Mode profile of the GP mode of a 50 nm graphene nanoresonator with $E_F = -0.37$ eV, obtained from a finite element electromagnetic simulation.

From these calculations, we can now explain the physical origins of the GP and SPPP features observed in our data. The graphene plasmon mode corresponds to a confined plasmon excitation of a monolayer graphene sheet in a nearly constant dielectric environment. As described in previous work,[50, 51, 55, 56] when the frequency (ω_p) of such modes are sufficiently lower than the interband transition energy ($2|E_F|$), ω_p should depend on both carrier density and nanoresonator width through the relationship $\omega_p \propto |E_F|^{1/2} W^{-1/2}$. This behavior is demonstrated by the graphene plasmon mode in Figure 2.3a, although it

deviates slightly at lower energies. At energies sufficiently far from the SiO_2 phonon energy, the dispersion relation of this mode (Figure 2.3b, solid lines) is seen to asymptotically approach the dispersion of graphene plasmons on a generic and nondispersive dielectric substrate.

The SPPP modes can be understood by considering that lattice oscillations in the SiO_2 lead to a sharp increase in the SiO_2 dielectric constant below its phonon energy. Because the graphene plasmon wavelength depends on the surrounding dielectric environment (see eq 2.1), the high dielectric constant of the SiO_2 within the small energy range below the phonon can compress graphene plasmons and allow for the graphene nanoresonators to support additional low energy plasmon oscillations. Thus this mode represents a composite excitation that consists of a SPP on the graphene coupled to a phonon excitation in the SiO_2, hence the term surface plasmon phonon polariton (SPPP). Signatures of such plasmon−phonon coupling have previously been observed in NSOM measurements of graphene on SiO_2 surfaces[67]. In Figure 2.3b we plot the dispersion relation for this SPPP (dashed lines) for different Fermi energies, revealing that the SPPP mode displays less dispersion than the graphene plasmon mode. Another notable feature of the SPPP that can be observed in the dispersion is that modes with high k-vectors are not supported. This can be understood by considering that, while the SiO_2 phonon changes the dielectric function of the substrate, it also introduces loss. Thus as the energy of the SPPP moves closer to the SiO_2 phonon energy, the system becomes too lossy due to substrate absorption, and the modes can no longer propagate.

The most remarkable feature of both the graphene plasmon and the SPPP resonances is how small the supported plasmon wavelengths are compared to the free space wavelength λ_0. For example, when E_F = -0.22 eV, we observe for the graphene plasmon feature that λ_0/λ_p = 49 for the 50 nm wide nanoresonators, and λ_0/λ_p becomes as large as 106 in the 20 nm nanoresonators. This factor is seen to decrease as the carrier density of the graphene sheet is increased and the graphene nanoresonators support higher energy resonances, such that for E_F = -0.41 eV, we measure λ_0/λ_p of 43 and 81 for 50 and 20 nm resonators,

respectively. These results are largely consistent with the theoretical predictions of infrared graphene plasmons.

2.2 Hybrid Surface-Plasmon-Phonon Polariton Modes in Graphene/Monolayer h-BN Heterostructures

2.2.1 Introduction

The results presented in Section 2.1 are consistent with the expectation that graphene plasmons should couple more strongly to their local environment than normal metal plasmons. In addition to our own work, other experiments performed on graphene devices on SiO_2[68, 69] and SiC[70, 71] substrates have shown that the graphene dispersion relation is indeed modified due to the substrate phonons, with extra modes appearing due to plasmon-phonon coupling which have been described as surface-plasmon-phonon-polaritons, or SPPPs.[68] In those experiments, however, the substrates used were much thicker than the plasmonic wavelengths, and thus did not test whether the graphene plasmons were coupling to a large volume of phonons spread throughout the dielectric environment, or only to the phonons in the immediate vicinity of the graphene sheet. Recently, experiments have been performed to investigate the coupling between graphene plasmons and thin layers of PMMA, showing that the PMMA phonon spectral signature can be enhanced through graphene plasmon coupling for PMMA layers as thin as 8 nm.[72] Here we fabricate graphene nanoresonator devices on a monolayer h-BN sheet in order to test the ability of graphene plasmons to couple to optical excitations that occupy an atomically thin slice of volume near the graphene. We find that the small mode volume of the graphene plasmons combined with the high oscillator strength of the h-BN phonons allows the two modes to strongly couple, forming two clearly separated hybridized SPPP modes that display an anti-crossing behavior.

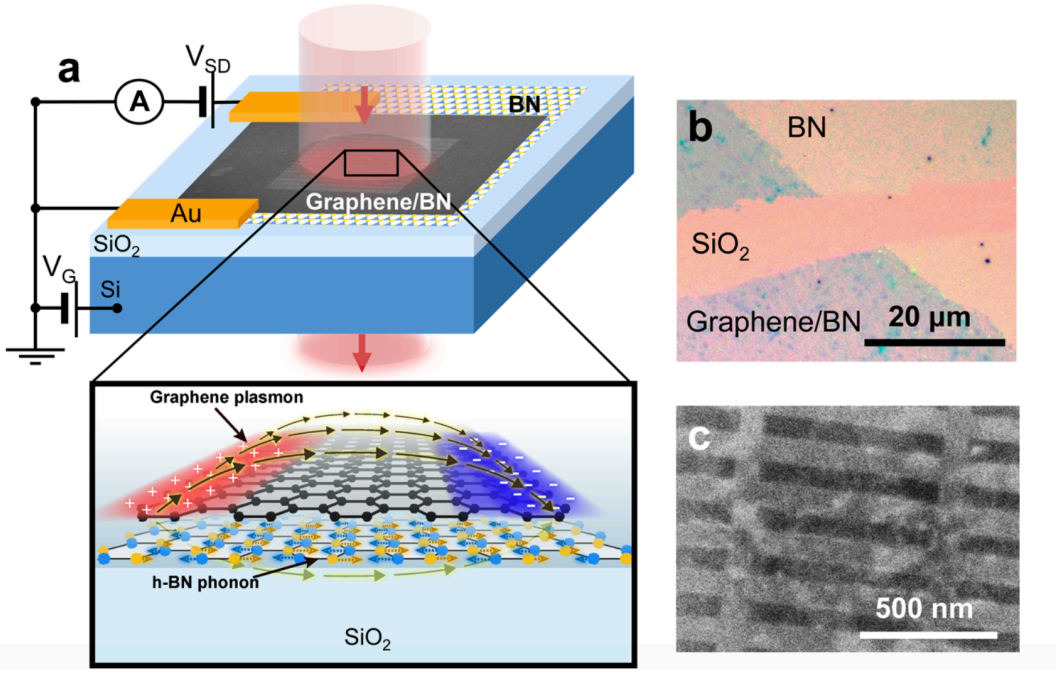

Figure 2.4: (a) Schematic of device measured and modeled in this paper. Graphene nanoresonators are fabricated on a monolayer h-BN sheet on a SiO_2 (285 nm)/Si wafer. Gold contact pads are used to contact the graphene sheet and the Si wafer is used to apply an in situ backgate voltage (V_G). Zoom-in shows cartoon of graphene plasmon coupling to h-BN optical phonon. (b) Optical image of unpatterned area of device where both the graphene and h-BN monolayers have been mechanically removed. (c) Scanning electron microscope image of the 80 nm graphene nanoresonators (light regions).

2.2.2 Experimental Measurement of Coupled 2D Phonon-Plasmon Polaritons

A schematic of our experimental device is shown in Figure 2.4. A monolayer h-BN sheet grown using chemical vapor deposition (CVD) on copper foil (Purchased from Graphene Supermarket #CVD-2X1-BN) is transferred to a SiO_2 (285 nm)/Si wafer and a CVD-grown graphene sheet is subsequently transferred onto the h-BN. Nanoresonators are patterned into the graphene surface using 100 keV electron beam lithography in PMMA, followed by an oxygen plasma etch, as previously (see also Appendix A). Infrared spectroscopy analysis reveals that the h-BN layer is also degraded in the lithographed areas. The resonators are patterned into electronically continuous bar array patterns with widths ranging from 30 nm to 300 nm, and a 1:2 width-to-pitch ratio, as shown if Fig. 2.4c. The dimensions of patterned nanoresonators are later precisely measured by using atomic force microscope (AFM). The Si layer was contacted and used as a back-gate electrode, and Cr(2

nm)/Au(100 nm) contacts were evaporated onto the nearby graphene surface such that the conductivity of the graphene could be monitored *in situ*. The charge neutral (zero carrier density) point was determined by the applied gate voltage that gave maximum resistance of the graphene sheet, and the carrier density at different gate voltages was determined by monitoring the cutoff energy of interband transitions in the graphene, which occurs at $2\times E_F$.[73, 74] As observed in previous work,[68] the charge neutral point is offset from zero gate voltage due to impurities introduced during the sample fabrication that hole dope the sample as well as charges donated by the surface of the SiO_2 substrate. The device was then placed in a Fourier transform infrared spectroscopy (FTIR) microscope and measured in transmission mode with light polarized perpendicular to the nanoresonators. All graphene nanoresonator spectra were normalized relative to spectra taken with zero carrier density as before. For reference, a transmission spectrum was taken on a bare h-BN area of the sample, as shown at the bottom of Figure 2.5. As can be seen in the figure, the h-BN spectrum is flat except for a narrow (19 cm^{-1}) resonance near 1370 cm^{-1}, which has been assigned in previous studies as an in-plane optical phonon of the h-BN.[75]

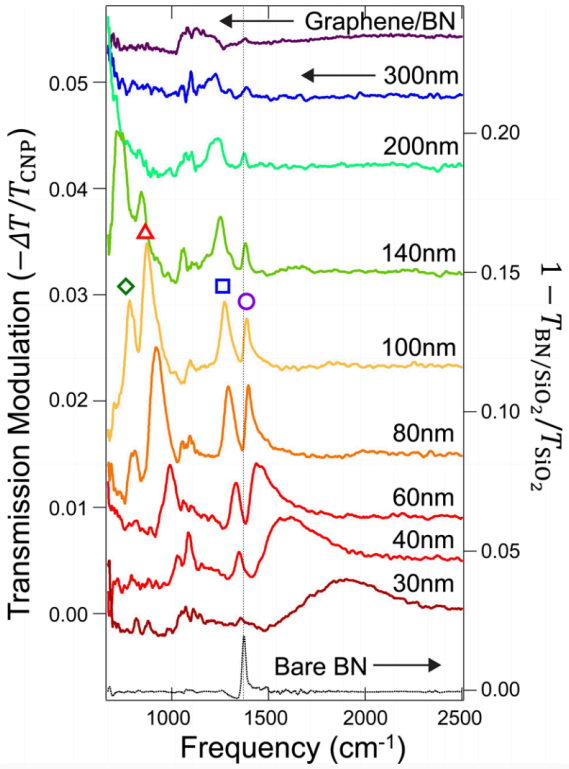

Figure 2.5: (Left axis) Normalized transmission spectra of graphene nanoresonators with width varying from 30 to 300 nm, as well as transmission through the unpatterned graphene/h-BN sheet. Spectra are measured at carrier densities of 1.0 x 10^{13} cm^{-2} and normalized relative to zero carrier density. For 80 nm ribbons, the four different observable optical modes are labeled with the symbols used to indicate experimental data points in Figure 3. (Right axis, bottom spectrum) Infrared transmission of the bare monolayer h-BN on SiO_2 normalized relative to transmission through the SiO_2 (285 nm)/Si wafer. The narrow (~19 cm^{-1}) peak that occurs at 1370 cm^{-1} has previously been assigned to an optical phonon in h-BN. The dotted vertical line indicates this peak position as a reference for the other spectra.

Figure 2.5 illustrates the dependence of transmission spectra on graphene nanoresonator width at 1.0 × 10^{13} cm^{-2} carrier density. As can be seen in this figure multiple features appear in the spectra, namely, two distinct set of optical modes can be observed appear above and below 1200 cm^{-1}. The two modes below 1200 cm^{-1} have previously been observed in graphene plasmonic devices on SiO_2, and have been assigned to SPPP modes associated with two SiO_2 phonons.[68, 69] The two modes above 1200 cm^{-1}, however, represent new optical features not observed in graphene/SiO_2 or graphene/SiC structures, which contained only a single dispersive mode above 1200 cm^{-1}. A close analysis of these

two features reveals an anti-crossing behavior near the 1370 cm^{-1} optical phonon energy of the h-BN, with the lower (upper) mode approaching that energy for small (large) ribbon widths. Furthermore, there is a relative shift in intensity between the upper and lower modes as the ribbon width varies, with the upper mode being more intense for small ribbon widths, and vice versa. Significantly, the intensity between the two features drops nearly to zero for 80 nm resonator widths, when the two features have equivalent intensities.

2.2.3 Modeling of Coupled Plasmon-Phonon Dispersion

In order to better understand the characteristics of each mode, we calculate the transmission spectrum of graphene nanoresonators for various widths using a finite element method within a local random phase approximation.[76] Here, the in-plane dielectric function of monolayer h-BN is described using Lorentz oscillator model with parameters fitted from transmission measurement of the bare h-BN on SiO_2[75], and its thickness is modeled to be 0.34 nm, the interlayer spacing of bulk h-BN. The scale-invariant plasmon phase shift upon reflection at the nanoresonator edges is calculated to be $\varphi \approx 0.35\pi$.[68] This implies that the plasmon wavevector $k_p = (\pi - \varphi)/W$ for the first-order plasmon resonance, with the width, W, extracted from AFM measurements. The resulting carrier-induced change in transmission is plotted in Figure 2.6 for varying wavevector and energy at 1.0×10^{13} cm^{-2} carrier density. The dispersion of the graphene/h-BN/SiO_2 nanoresonator optical modes can be observed in this plot as the maxima in the transmission modulation, $-\Delta T/T_{CNP}$. These features show a strong correspondence with the experimentally measured features, with modes appearing above and below the h-BN optical phonon energy that display a clear anti-crossing behavior.

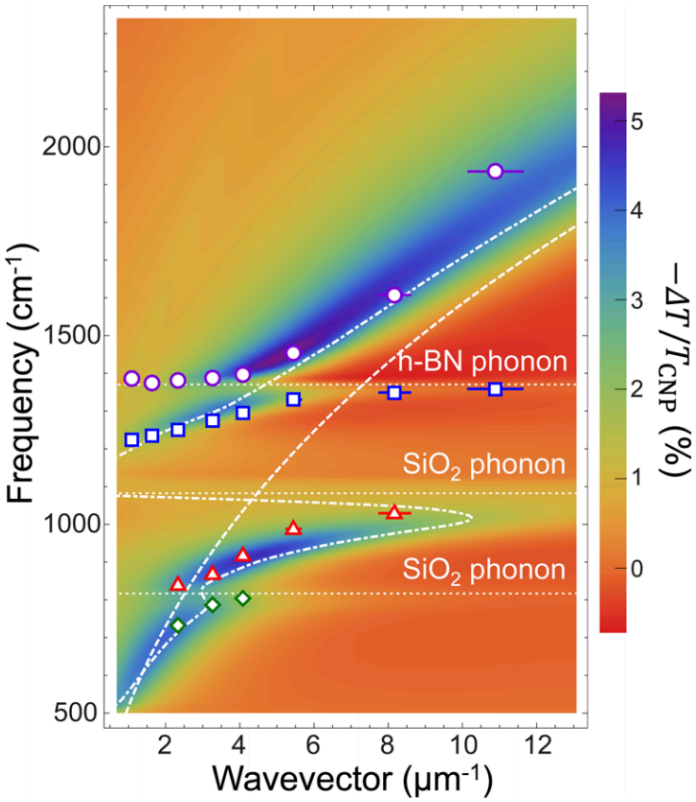

Figure 2.6: Calculated change in transmission for graphene/monolayer h-BN/SiO_2 nanoresonators of varying width at a carrier density of 1.0 x 10^{13} cm^{-2}, normalized relative to zero carrier density. The wavevector is determined by considering the ribbon width, W, as well as the phase of the plasmon scattering off the graphene ribbon edge, as described in the text. Experimental data is plotted as symbols indicating optical modes assigned in Figure 2.5. The error bars represent uncertainty in the resonator width that is obtained from AFM measurements. For small k-vectors (large resonators), this uncertainty is smaller than the symbol size. The dashed line indicates the theoretical dispersion for bare graphene plasmons, while the dash-dot line indicates the dispersion for graphene/SiO_2 The three horizontal dotted lines indicate the optical phonon energies of h-BN and SiO_2.

The behavior displayed experimentally and theoretically in Figures 2.5 and 2.6 is indicative of a hybridization between the graphene plasmons modes and the h-BN optical phonon modes that creates two new SPPP modes with dispersion relations that are distinctly different from the original graphene plasmon dispersion (dashed line, Fig. 2.6) as well as the graphene/SiO_2 dispersion (dashed-dot line, Fig. 2.6). This hybridization can be understood through an electromagnetic coupled oscillator model where the local polarization field created by lattice displacement in the h-BN exerts a force on the free

carriers in the overlying graphene resonators via near field interaction, and, likewise, the polarization due to displaced carriers in the graphene exerts a force on the h-BN lattice. When this coupling becomes sufficiently strong, the lifetimes and the energies of the two constitutive optical modes can be significantly shifted and the resulting optical features are hybrid modes, or SPPPs. These new optical modes contain both plasmon-like and phonon-like character, with the relative contribution of each constitutive mode dependent on the graphene ribbon width and carrier density. Recognizing that each spectrum displayed in Fig. 2.5 shows the relative difference in transmission while varying the carrier density in graphene, the relative intensity of two resonances roughly indicates how much the graphene plasmon contributes to each hybrid SPPP mode. Therefore, we know that the upper(lower) SPPP mode is more plasmon-like for small(large) ribbon widths from the relative shift in peak intensity, and that for 80 nm graphene/h-BN resonators, the two modes are both equally plasmon-like and phonon-like. This behavior is consistent with the extracted dispersion properties of each mode shown in Fig. 2.6.

In combination with the hybridization behavior described above, we observe a pronounced minimum in absorption near the h-BN phonon energy for 60, 80, and 100 nm resonators, for which the bare graphene plasmon mode would typically overlap the h-BN phonon energy. We interpret this phenomenon as a classical, phonon-based analogue to electromagnetically induced transparency (EIT) experiments performed on atomic gases. In this description, it is observed that when the graphene plasmon mode is brought into resonance with the h-BN phonon, the polarizations of the two modes cancel each other out, creating a transparency window where no absorption occurs in the plasmonic modes. The clearly separated resonance peaks also indicate that the coupling between graphene plasmons and the h-BN phonons enters a classical “strong-coupling” regime, where the associated electromagnetic interaction can fully transfer energy between the plasmon and phonon states before decaying via damping. This regime is characterized by a large splitting between the two hybridized modes, such that the minimum energy separation is more than the sum of the two linewidths, and the spectral intensity between the two modes approaches zero.[77] For the experimental data shown here, the minimum splitting we

observe between the two graphene/h-BN SPPPs is 100 cm^{-1} (for 80 nm resonators) which is more than the sum of the two associated peak widths of 25 and 55 cm^{-1}, indicating that the system is in a strong coupling regime.[77] This phenomenon has been explored in conventional metal plasmonics experiments using molecular vibrations or dyes coupled to metallic plasmons.[78-83] In those experiments, however, a thick (>20 nm) layer of optically active material was required for strong coupling to be achieved. Here, we observe that the high confinement of graphene plasmons allows them to strongly couple to optical phonons in an atomically thin layer.

2.3 Tunable Enhanced Absorption in a Graphene Salisbury Screen

2.3.1 Introduction

While the emergence of the SPPP modes in graphene nanoresonators demonstrates the strong interaction of the material with its surroundings, the absolute magnitude of these effects is limited by the amount of light absorbed by the graphene sheet, which is typically 2.3% at infrared and optical frequencies[84, 85] – a small value that reflects the single atom thickness of graphene. To increase the total graphene-light interaction, a number of novel light scattering and absorption geometries have recently been developed. These include coupling graphene to resonant metal structures[86-90] or optical cavities where the electromagnetic fields are enhanced[91-93], or draping graphene over optical waveguides to effectively increase the overall optical path length along the graphene[94, 95]. While those methods rely on enhancing interband absorption processes, we are interested in enhancing the absorption in graphene plasmon modes to take advantage of their unique properties and high confinement factors. These modes have been shown to display large absorption when embedded in liquid salts or by sandwiching dopants between several graphene layers[96-98]. However without blocking the transmission of light, it is not possible to achieve unity absorption in these previously demonstrated geometries[96-98]. Moreover, in order to access nonlinear or high frequency modulation as well as the high confinement factors characteristic of graphene plasmons, device geometries with open access to the graphene surface that operate with field effect gating at low doping are desirable.

Plasmonically active metallic and semiconductor structures can achieve near-perfect absorption of radiation at specified frequencies using a resonant interference absorption method.[99-103] The electromagnetic design of these structures derives in part from the original Salisbury screen design[104], but with the original resistive sheet replaced by an array of resonant metal structures used to achieve a low surface impedance at optical frequencies. The high optical interaction strength of these structures has made them useful in such applications as chemical sensing,[101, 105] and it was recently proposed that similar devices could be possible using graphene to achieve near perfect absorption from THz to Mid-IR.[106, 107] Such a device would offer an efficient manner of coupling micron-scale free-space light into nanoscale plasmonic modes, and would further allow for electronic control of that in-coupling process. In this work, we construct a device based on that principle, using tunable graphene nanoresonators placed a fixed distance away from a metallic reflector to drive a dramatic increase in optical absorption into the graphene.

2.3.2 Experimental Demonstration of Enhanced Absorption

A schematic of our device is shown in Figure 2.7a. A graphene sheet grown using chemical vapor deposition on copper foil is transferred to a 1 μm thick low stress silicon nitride (SiN_x) membrane with 200nm of Au deposited on the opposite side that is used as both a reflector and a backgate electrode. Nanoresonators with widths ranging from 20-60 nm are then patterned over 70 × 70 μm^2 areas into the graphene using 100 keV electron beam lithography. An atomic force microscope (AFM) image of the resulting graphene nanoresonators is shown in the inset of Fig. 2.7b. The device was placed under a Fourier transform infrared (FTIR) microscope operating in reflection mode, with the incoming light polarized perpendicular to the resonators. The carrier density of the graphene sheet was varied *in situ* by applying a voltage across the SiN_x between the gold and the graphene, and the resulting changes in resistance were continuously monitored using source and drain electrodes connected to the graphene sheet (Fig 2.7b). The carrier density of the graphene nanoresonators was determined from experimentally measured resonant peak frequencies.

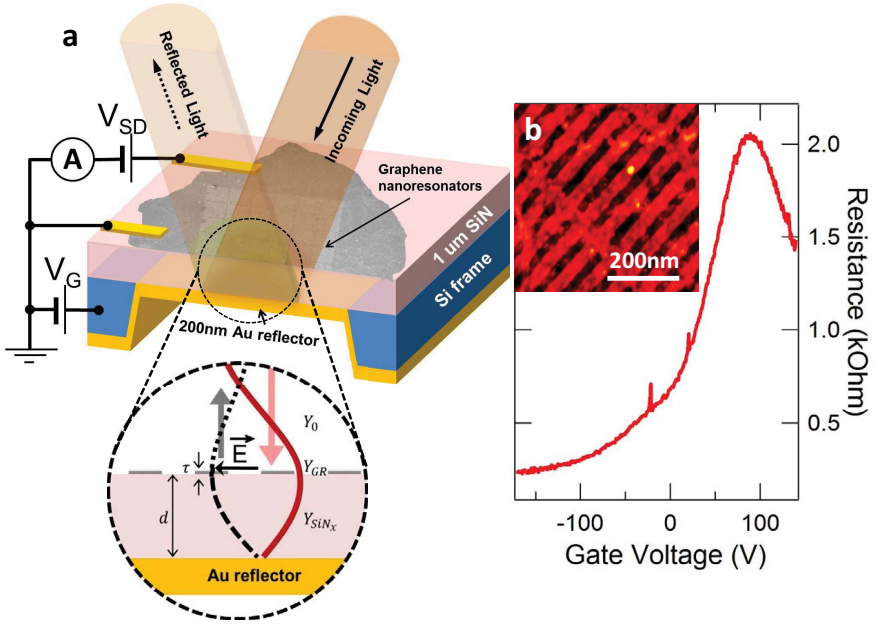

Figure 2.7: (a) Schematic of experimental device. 70 × 70 μm^2 graphene nanoresonator array is patterned on 1 μm thick silicon nitride (SiN_x) membrane via electron beam lithography. On the opposite side, 200 nm of gold layer is deposited that serves as both a mirror and a backgate electrode. A gate bias was applied across the SiNx layer in order to modulate the carrier concentration in graphene. The reflection spectrum was taken using a Fourier Spectrum Infrared (FTIR) Spectrometer attached to an infrared microscope with a 15X objective. The incident light was polarized perpendicular to the resonators. The inset schematically illustrates the device with the optical waves at the resonance condition. (b) DC resistance of graphene sheet as a function of the gate voltage. The inset is an atomic force microscope image of 40 nm nanoresonators.

The total absorption in the device – which includes absorption in the SiN_x and the graphene resonators – is determined from the difference in the reflected light from the nanoresonator arrays and an adjacent gold mirror. For undoped and highly doped 40 nm nanoresonators, the total absorption is shown in Figure 2.8a, revealing large absorption at frequencies below 1200 cm^{-1}, as well as an absorption peak that varies strongly with doping at 1400 cm^{-1} and a peak near 3500 cm^{-1} that varies weakly with doping. In order to distill absorption features in the graphene from the environment (i.e., SiN_x and Au back reflector), we plot the difference in absorption between the undoped and doped nanoresonators, as shown in Figure 2.8b for 40 nm nanoresonators. This normalization removes the low frequency feature below 1200 cm^{-1}, which is due to the broad optical phonon absorption in the SiN_x and is independent of graphene doping. The absorption feature at 1400 cm^{-1},

however, shows a dramatic dependence on the graphene sheet carrier density, with absorption into the graphene nanoresonators varying from near 0% to 24.5% as the carrier density is raised to 1.42×10^{13} cm^{-2}. Because the absorption increases with carrier density, we associate it with resonant absorption in the confined plasmons of the nanoresonators.[30, 97, 108, 109]

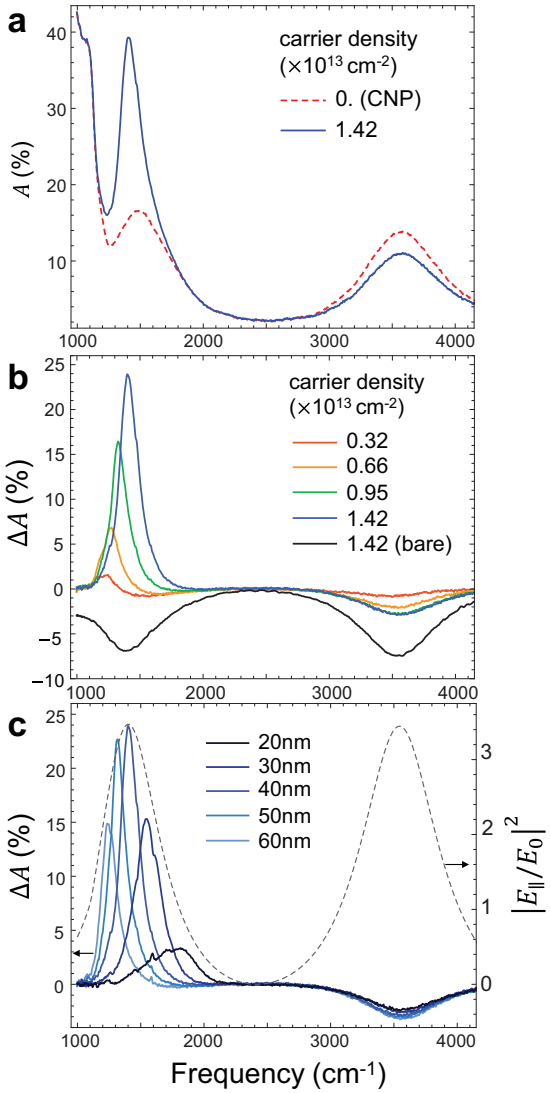

Figure 2.8: (a) The total absorption in the device for undoped (red dashed) and highly hole doped (blue solid) 40 nm nanoresonators. Absorption peaks at 1400 cm^{-1} and a peak at 3500 cm^{-1} are strongly modulated by varying the doping level, indicating these features are originated from graphene. On the other hand, absorption below 1200 cm^{-1} is solely due to optical phonon loss in SiN_x layer. (b) The change in absorption with respect to the absorption at the charge neutral point (CNP) in 40 nm wide graphene nanoresonators at various doping levels. The solid black curve represents the absorption difference spectrum

of bare (unpatterned) graphene. (c) Width dependence of the absorption difference with the carrier concentration of 1.42×10^{13} cm^{-2}. The width of the resonators varies from 20 to 60 nm. The dashed curve shows the theoretical intensity of the surface parallel electric field at SiN_x surface when graphene is absent. Numerical aperture of the 15X objective (0.58) is considered.

In Figure 2.8b we also see that absorption at 3500 cm^{-1} exhibits an opposite trend relative to the lower energy peak, with graphene-related absorption decreasing with higher carrier density. This higher energy feature is due to interband graphene absorption where electronic transitions are Pauli blocked by state filling at higher carrier densities.[74] For spectra taken from the bare, gate-tunable graphene surface, this effect leads to ~8% absorption, roughly twice the intensity observed from patterned areas. Finally, in Figure 2.8c, we investigated the graphene nanoresonator absorption as the resonator width is varied from 20 to 60 nm at fixed carrier density. This figure shows that the lower energy, plasmonic absorption peak has a strong frequency and intensity dependence on resonator width, with the maximum absorption occurring in the 40 nm ribbons.

The observed resonance frequency varies from 1150 - 1800 cm^{-1}, monotonically increasing with larger carrier densities and smaller resonator widths. The plasmon energy asymptotically approaches ~1050 cm^{-1} due to a polar phonon in the SiN_x that strongly reduces the dielectric function of the substrate at that energy.[110] This coupling between the substrate polar phonon and the graphene plasmon has also been previously observed in back-gated SiO_2 devices and was commented on in Chapter 2.1.[109, 111]

2.4 Conclusions and Outlook

In summary, this chapter has presented results on the gate-tunable plasmonic response of monolayer graphene. We have observed that by utilizing an applied gate voltage, it is possible to tune the plasmonic absorption across the mid-infrared. In addition, this tuning allows us to actively control the coupling between the graphene and its environment, including the presence of composite surface plasmon-phonon polaritons. These modes are observed in bulk substrates (e.g. SiO_2) as well as in the monolayer limit (e.g. h-BN). Finally, we have demonstrated that by matching the plasmon resonance of the graphene to

an external cavity resonance – a quarter wavelength thick Salisbury Screen design – we can enhance the absorption in the graphene to 24.5%. These results provide insights into tightly confined quasiparticles in the monolayer limit, as well as suggesting that nanophotonic devices based on graphene plasmons could be useful as tunable 'perfect absorber' devices, with implications for thermal emission that will be discussed in Chapter 3. Finally, we suggest that the highly confined nature and resulting ultra-small mode volume of graphene plasmons may enable strong Purcell enhancement of emitters in the mid-infrared that could be actively controlled.

C h a p t e r 3

GRAPHENE-BASED ACTIVE CONTROL OF THERMAL RADIATION

"In this house we obey the laws of thermodynamics!"

– Homer Simpson

Chapter 3.1

1. Victor W. Brar, **Michelle C. Sherrott**, Min Seok Jang, Laura Kim, Mansoo Choi, Luke A. Sweatlock, Harry A. Atwater, "Electronic modulation of infrared radiation in graphene plasmonic resonators", *Nature Communications*, **6**, 7032 (2015)
DOI: 10.1038/ncomms8032

All matter at finite temperatures emits electromagnetic radiation due to the thermally induced motion of particles and quasiparticles. Dynamic control of this radiation could enable the design of novel infrared sources; however, the spectral characteristics of the radiated power are dictated by the electromagnetic energy density and emissivity, which are ordinarily fixed properties of the material and temperature. Here we experimentally demonstrate tunable electronic control of blackbody emission from graphene plasmonic resonators. It is shown that the graphene resonators produce antenna-coupled blackbody radiation, which manifests as narrow spectral emission peaks in the mid-infrared. By continuously varying the nanoresonator carrier density, the frequency and intensity of these spectral features can be modulated via an electrostatic gate. We extend this work to show that we can control not just the spectral distribution of thermal radiation, but also its polarization state. This opens the door for future devices that may control blackbody radiation at timescales beyond the limits of conventional thermo-optic modulation. Multi-pixel devices composed of the deep-sub-wavelength graphene resonators may enable 'designer' thermal radiation profiles that can be switched at MHz speeds or faster[89].

3.1 Electronic Modulation of Thermal Radiation in a Graphene Salisbury Screen

3.1.1 Introduction

Thermal radiation is commonly viewed to be broadband, incoherent and isotropic, with a spectral profile and intensity that are dependent on the emissivity of a material, and that vary only with changes in temperature. Recent experiments on nanoengineered structures, however, have begun to challenge these notions, showing that blackbody emission can be coherent and unidirectional, with narrow spectral features. These structures have included patterned gratings on metal or silicon carbide surfaces that can control the directionality and coherence of thermal radiation,[112, 113] as well as photonic crystals,[114] size-tunable Mie resonances,[115] and frequency selective meta-surfaces[116] which can tune the spectral profile. Progress has also been made in demonstrating dynamic control of thermal radiation through *in situ* modification of material emissivity. This has been achieved with devices that incorporate phase change materials which display temperature-dependent emissivities,[117] as well as electronically controlled devices, where injected charges are used to overdampen polariton modes in quantum wells.[118] These results suggest that careful control of both the photonic and electronic structure of metasurfaces could allow for thermal emitters that have continuously variable frequency and directionality control, and that can operate at speeds much faster typical thermal cycling times, potentially approaching speeds of modern telecommunication devices.

Graphene provides a unique platform for studying and controlling thermal radiation at infrared wavelengths. The optical absorptivity/emissivity of graphene depends on two carrier density dependent terms: an intraband contribution that is characterized by a large Drude-like peak in the DC to far-IR range, and an interband contribution that manifests as a step-like feature in the absorption in the far to near-IR at 2 x E_F.[73, 74, 85, 119-121] Additionally, the linear bandstructure and two-dimensional nature of graphene allow for it to support plasmonic modes that have a unique dispersion relation, discussed in the previous chapter.[122-125] These plasmonic modes have been proposed as a means of efficiently coupling to THz radiation,[126-128] and they have been shown to create strong absorption pathways in the THz to mid-IR when the graphene is patterned to form plasmonic Fabry-

Perot resonances.[58, 69, 129, 130] The intensity and frequency of the plasmonic modes in graphene are carrier density dependent, and they display extremely large mode confinement, which allows them to efficiently couple to excitations (e.g. phonons) in their environment and create new optical modes.[68, 69, 72, 129] As the graphene sheet is heated up, these different infrared absorption pathways become thermal emission sources, with contributions that vary with the graphene carrier density and surface geometry. The graphene plasmons are particularly interesting as thermal emitters because their small mode volumes allow for extremely efficient thermal energy transfer in the near field[131, 132], and also lead to large Purcell factors that can enhance the emission rate of emitters within the plasmon mode volume[133]. These large Purcell factors suggest that electronic control of the graphene plasmonic modes could potentially control thermal radiation at time scales much faster than the spontaneous emission rate for conventional light emitting diodes and classical blackbody emission sources.

3.1.2 Experimental Realization of Dynamically Tuned Thermal Radiation

In this work, we experimentally demonstrate the dynamic tuning of blackbody emission through electronic control of graphene plasmonic nanoresonators on a silicon nitride substrate at temperatures up to 250°C. Our device is based on field effect tuning of the carrier density in nanoresonators, which act as antennas to effectively outcouple thermal energy within the resonator mode volume. We show that through this mechanism the thermal radiation generated by substrate phonons and inelastic electron scattering in graphene can be tuned on and off. By varying the charge carrier density of the graphene from ~ 0 - 1.2 × 10^{13} cm^{-2}, with resonator widths from 20 – 60 nm, we show that a narrow bandwidth emission feature may be tuned in intensity and varied in frequency across the mid-IR, from approximately 1200 – 1600 cm^{-1}.

A schematic of the measurement apparatus and device geometry are shown in Figure 3.1a. The device consists of 20 – 60 nm wide graphene nanoresonators patterned into a graphene sheet on a 1 μm SiN_x layer with a gold back reflector that also serves as a back gate electrode. This device geometry was previously used as a gate-tunable absorber in the mid-

IR, described in Chapter 2.3, where a large enhancement in absorption was observed when the graphene plasmonic resonance was matched to the energy of the $\lambda/4n_{SiN}$ 'Salisbury Screen' resonance condition in the 1 μm SiN_x layer, which occurred at 1360 cm^{-1}.[134, 135] In those experiments, the polarized absorption (aligned to the confined dimension of the graphene resonator) in the graphene nanoresonators could be tuned from 0 to up to 24.5% for large carrier densities. In this work, a similar sample displayed up to 3% total absorption when probed using our apparatus. This smaller number reflects the use of non-polarized light, the higher numerical aperture objective of the apparatus, the effect of the window of the vacuum stage, and the lower carrier densities used due to the onset of Poole-Frenkel tunneling in the SiN_x at higher temperatures and high gate biases.[134, 136]

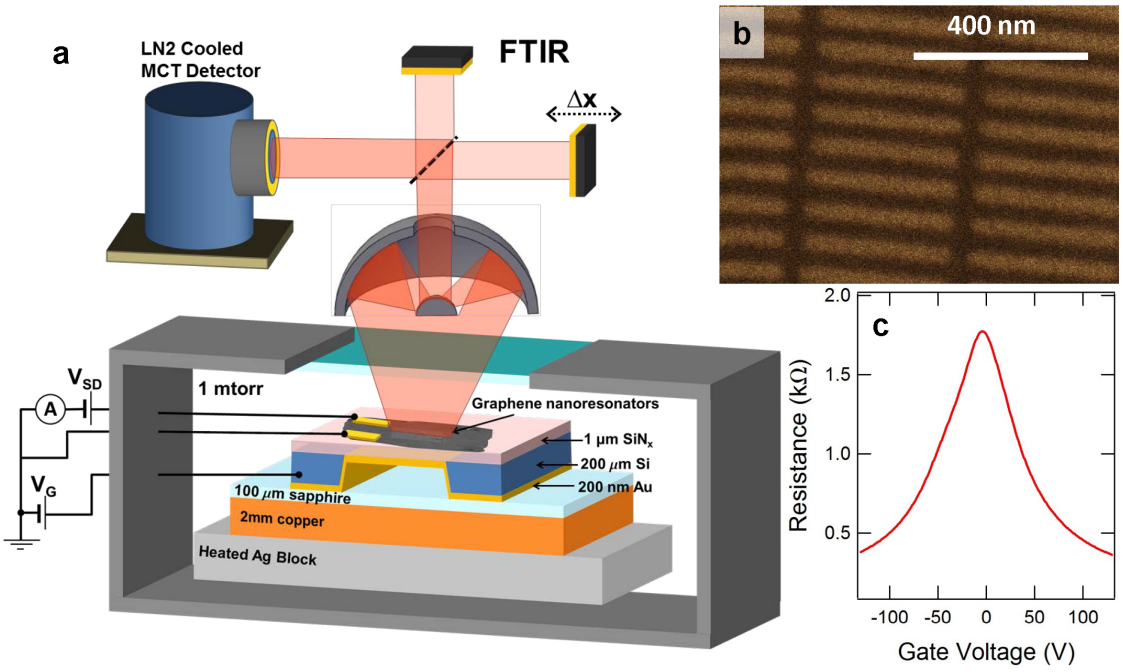

Figure 3.1: Device and experimental set-up (a) Schematic of experimental apparatus. 70 × 70 μm^2 graphene nanoresonator arrays are placed on a 1 μm thick SiN_x membrane with 200 nm Au backreflector. The graphene was grounded through Au(100 nm)/Cr(3 nm) electrodes that also served as source-drain contacts. A gate bias was applied through the SiN_x membrane between the underlying Si frame and graphene sheet. The temperature controlled stage contains a feedback controlled, heated silver block that held a 2mm thick

copper sample carrier, with a 100 μm thick sapphire layer used for electrical isolation. The temperature was monitored with a thermocouple in the block, and the stage was held at a vacuum of 1 mtorr. A 1mm thick potassium bromide (KBr) window was used to pass thermal radiation out of the stage, which was collected with a Cassegrain objective and passed into an FTIR with an MCT detector. (b) A representative SEM image of 30 nm graphene nanoresonators on a 1μm thick SiN_x membrane. (c) Source-drain resistance vs gate voltage curve of the device. The peak in the resistance occurs at the charge neutral point (CNP), when the Fermi level (E_F) is aligned with the Dirac point.

Figure 3.2 (left axis) shows the emitted radiation at 250°C from a black soot reference sample and from a 40 nm graphene nanoresonator array at 250°C under doped (1.2×10^{13} cm^{-2}) and undoped conditions. On the right axis of Fig. 3.2 we plot the change in emissivity corresponding to the observed change in emitted light from the undoped to doped graphene resonators. This change in emissivity is calculated assuming unity emissivity at all frequencies for the black soot reference and normalizing accordingly. This accounts for the non-idealities of the FTIR optics as well as giving us an accurate temperature calibration. As can be seen in the figure, increasing the carrier density of the graphene nanoresonators leads to increases in emissivity near 730 cm^{-1} and 1400 cm^{-1}.

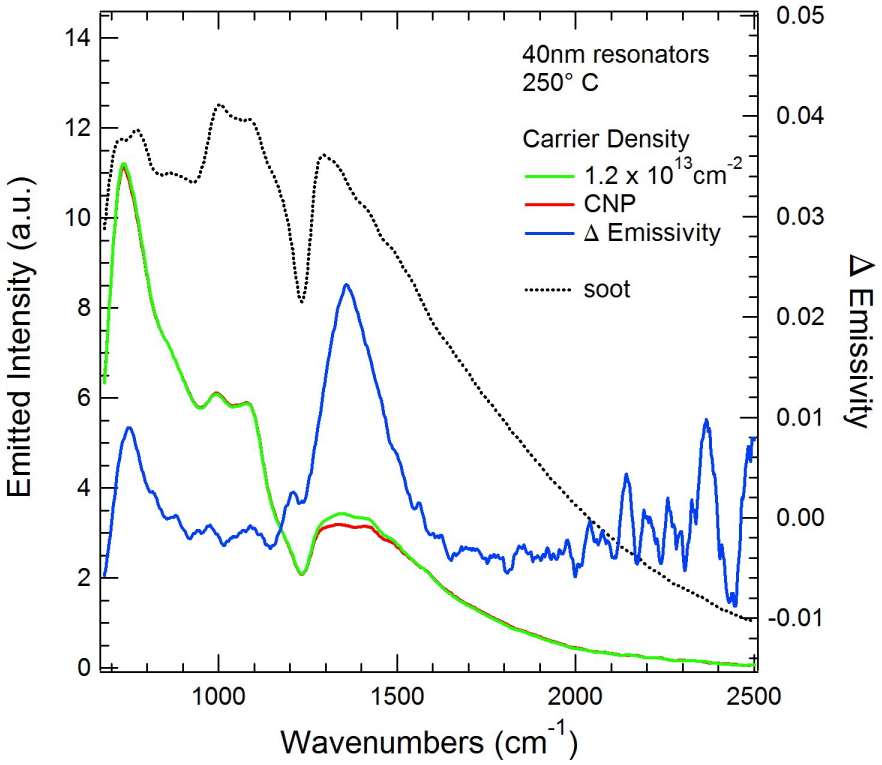

Figure 3.2: Experimental emission results (left axis) Emitted thermal radiation at 250°C from soot (black dotted line) and 40 nm graphene nanoresonators at zero (red) and 1.2 × 10^{13} cm^{-2} (green) carrier density. (right axis, blue line) Change in emissivity of 40 nm nanoresonators due to increase in carrier density. Soot reference is assumed to have emissivity equal to unity.

In order to explore these gate-tunable emissivity features, we investigate their behavior as the nanoresonator doping and width is varied, as shown in Figures 3.3a and 3.3b, as well as their polarization dependence (Fig. 3.3c). These results indicate that the intensity, width, and energetic position of the thermal radiation feature near 1360 cm^{-1} are widely tunable, and that this feature is strongly polarized. The energy of this feature increases as the nanoresonator width is decreased and as the carrier density is increased, while the intensity of this feature increases with carrier density, and is largest in 40 nm resonators, when it occurs closest to the $\lambda/4n_{SiN}$ resonance condition of the SiN_x at 1360 cm^{-1}. Because Kirchoff's Law dictates that thermal emissivity is equal to absorptivity, these observations

are consistent with previously reported absorption measurements performed on identical samples that showed a narrow absorption feature near 1360 cm^{-1}.[1,134]

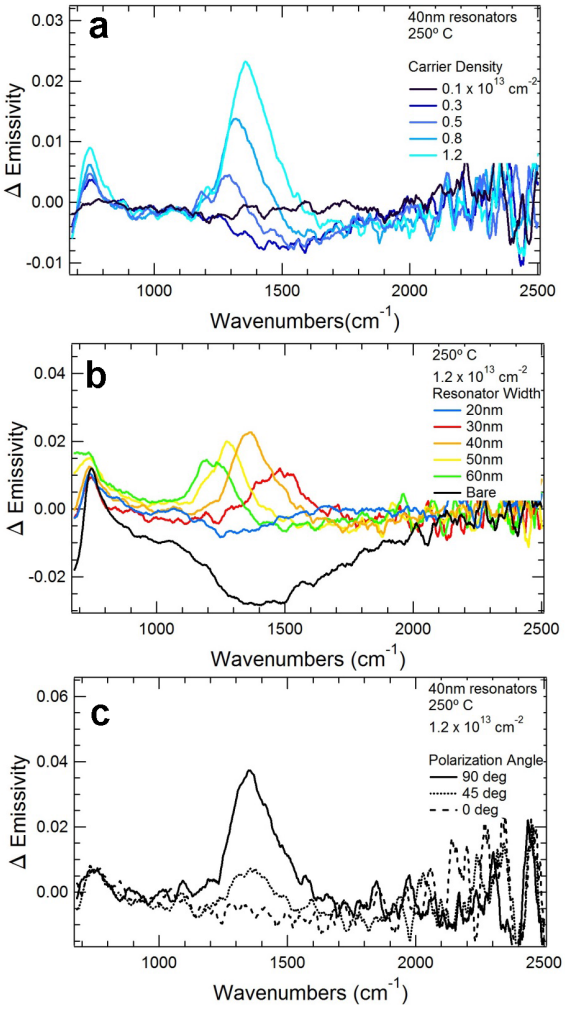

Figure 3.3: Emissivity tunability (a) Carrier density dependence of change in emissivity with respect to the CNP for 40 nm graphene nanoresonators at 250°C. (b) Width dependence of change in emissivity for 20, 30, 40, 50 and 60 nm wide nanoresonators at 250°C and for a carrier density of 1.2×10^{13} cm^{-2}. (black line) Emissivity change for a nearby region of bare, unpatterned graphene at the same carrier density and temperature. (c) Polarization dependence of the emissivity change for 40 nm graphene nanoresonators at 250°C, for a carrier density of 1.2×10^{13} cm^{-2}.

The lower energy emissivity modulation feature near 730 cm^{-1} shows different behavior than the higher energy peak. Namely, the low energy feature shows extremely weak polarization dependence, and also shows no noticeable dependence on graphene nanoresonator width. As the carrier density is increased, there is a small, non-monotonic increase in intensity for this feature, but it shows no spectral shift. Finally, unlike the higher energy peak, the lower energy peak is also observed in the bare, unpatterned graphene, where it appears as a slightly narrower feature. The absorption properties of this device near the energy range of the lower energy feature were not discussed in previously reported work in Chapter 2 due to the low energy cutoff of the detector used in that work.

3.1.3 Theoretical Interpretation of Results

We explain the above phenomena as electronic control of thermal radiation due to a combination of plasmon-phonon and plasmon-electron interactions, Pauli-blocking of interband transitions, and non-radiative transfer processes between the SiN_x and the graphene sheet. While Kirchoff's law dictates that the thermal equilibrium emissivity must be equal to the absorptivity for any material, the precise, microscopic mechanisms of thermal emission are dramatically modified in inhomogeneous artificial photonic materials with highly confined optical modes relative to homogeneous materials.

We attribute the prominent spectral feature at 1360 cm^{-1} to a Fabry-Perot plasmonic resonance from the patterned graphene. The width and doping dependence of the 1360 cm^{-1} feature follows the behavior expected for graphene plasmonic modes, and is consistent with reflection measurements.[134] Specifically, the graphene plasmon resonant frequency should vary as $\omega_p \propto n^{1/4}W^{-1/2}$, where n is the carrier density and W refers to the resonator width. This relationship was explored in depth in Chapter 2, and results from the unique dispersion relation of graphene plasmons due to their two-dimensional nature and the linear band structure of graphene. This behavior is in accord with the emission spectra in which we observe a blue shift of the plasmonic resonance at increased doping and decreased graphene nanoresonator width. The intensity of the higher energy peak increases with graphene carrier density, an effect that results from the increased polarizability of the

resonant plasmonic modes. Finally, this feature is strongly polarization dependent – as we would expect for laterally confined graphene plasmonic resonant modes – and vanishes quickly as we rotate the polarization of the probing radiation from 90° to 0° relative to the nanoresonator axis. This suggests that graphene nanoresonators may be an interesting platform for light sources with controllable polarization, to be discussed in Chapter 3.2.

In order to understand the source of thermally excited plasmons in graphene nanoresonators, we note that the microscopic processes that lead to plasmonic loss in graphene should by reciprocity correspond to plasmon-generating processes when the sample is heated. For the case of the 1360 cm^{-1} feature we observe here, the plasmonic loss (and corresponding plasmon generating) processes are attributed to the factors that limit the electron mobility of the graphene, such as defect scattering, impurity scattering, and inelastic electron-electron and electron-phonon interactions.[68, 69, 123, 134, 137] Additionally, plasmons have been shown to decay via loss channels associated with the edges of graphene nanostructures, and by coupling to substrate phonons.[68, 69] For a bare graphene sheet, the plasmons generated by thermal emission do not couple well to free space and are thus non-radiative. Upon patterning the graphene, however, the plasmonic resonances can effectively serve as antennas that out-couple radiation, and the plasmon decay processes give rise to free-space thermal emission by exciting resonant plasmonic modes, which then radiate.

The resonant enhancement of emission from plasmon generating processes is in competition with the blocking of interband transitions that act as thermal emitters in the undoped graphene, but are forbidden due to Pauli blocking when the sheet is doped.[73, 74] The role of interband transitions can be seen most clearly in the bare graphene emissivity spectra in Fig. 3.3b where there is a broad decrease in emissivity near 1360 cm^{-1} at higher carrier densities. While interband transitions should occur across a wide range of frequencies, in the back reflector geometry we use here, thermal emission from the surface can either constructively or destructively interfere with itself and is thus most prominent at 1360 cm^{-1} , the $\lambda/4n_{SiN}$ frequency of the SiN_x layer. For patterned graphene areas,

however, we find that doping the graphene allows for the resonant plasmonic modes to create an emission enhancement that outweighs the decrease in emission due Pauli blocking, and thus we get a net increase in emission near 1360 cm^{-1}.

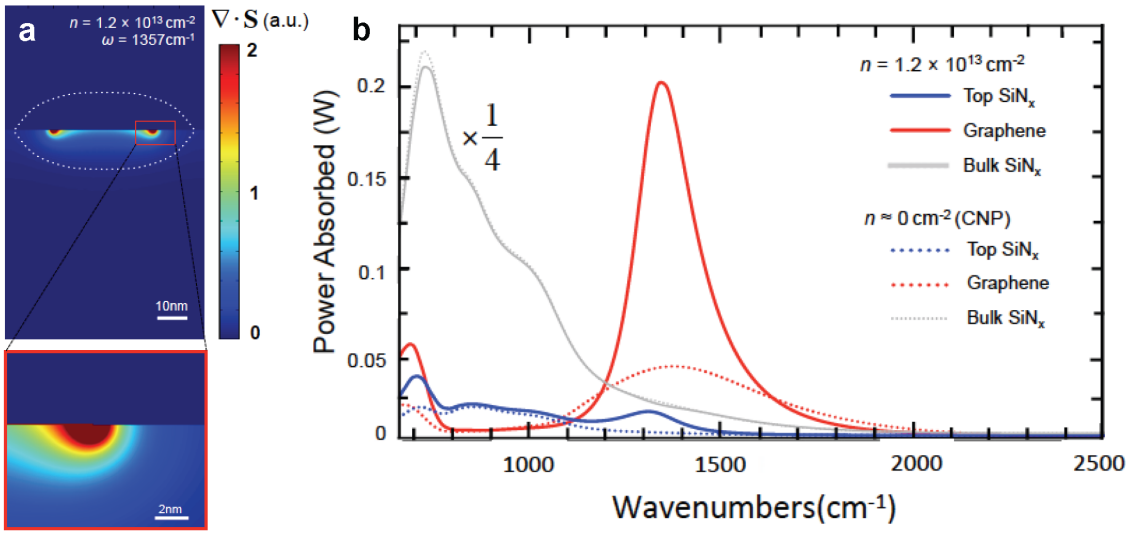

Figure 3.4: Finite element power density simulations (a) Finite element electromagnetic simulation of $\nabla \cdot \mathbf{S}$ (electromagnetic power density) in graphene/SiN_x structure for 40 nm graphene nanoresonators on 1 μm SiN_x with a gold backreflector. The simulation is performed at 1357 cm^{-1} (on plasmon resonance) at a carrier density of 1.2×10^{13} cm^{-2}. The dotted white line indicates the mode volume of the plasmon. (b) Integrated power density absorbed in the 40 nm graphene nanoresonator, the SiN_x within the plasmon mode volume (Top SiN_x), and the remaining bulk of the SiN_x (Bulk SiN_x) for carrier densities of 1.2×10^{13} cm^{-2} and ~ 0 cm^{-2} (the charge neutral point).

As mentioned above, in addition to out-coupling of radiation due to plasmon loss mechanisms in the graphene, the plasmonic resonators also interact with vibrations in the SiN_x substrate. When the SiN_x is heated, the plasmonic modes act as antennae to enhance the spontaneous thermal radiation from the nearby SiN_x. The enhancement of the spontaneous emission radiative rate and of the quantum efficiency arising from dipole emitters' proximity to a dipole optical antenna is well known,[138-140] and is attributed to increasing the probability of radiative emission by modification of the photonic mode density.[141] The rate enhancement is correlated to the strong polarizability of the graphene at its plasmonic resonance that enhances the out-coupling of thermal radiation from the SiN_x.

In particular, the radiative rate is expected to be most strongly amplified within the mode volume of the resonant graphene plasmon, which for 40 nm resonators at 1.2×10^{13} cm^{-2} roughly corresponds to the area within 10 nm of the resonator (see Fig. 3.4a). We therefore assign the net increase of thermal emission near 1360 cm^{-1} to a combination of thermal excitations in the graphene as well as thermal phonons in the SiN_x that are out-coupled through the confined plasmonic modes in the graphene nanoresonators.

In contrast to the high-energy feature, which is due to plasmons in the graphene, the low energy feature at 730 cm^{-1} is related to an optically active phonon in the SiN_x substrate. This phonon mode is strongly absorbing (emitting) and is typically located near 850 cm^{-1}. The large divergence in the SiN_x permittivity due to this phonon, however, creates an additional $\lambda/4n_{SiN}$ condition in the structure that leads to a destructive interference effect, resulting in an absorption (emission) maximum at 730 cm^{-1}. When graphene is placed on top of the SiN_x, the intraband and interband transitions in the graphene act to modify the surface impedance of the device. The result is that increasing the doping in the graphene leads to a stronger destructive interference effect, which manifests as larger emission from the SiN_x layer (see Fig. 3.4b). In addition to direct emission from the SiN_x phonon, the graphene plasmons can couple to the SiN_x phonons to create new surface phonon plasmon polariton modes (SPPPs).[68, 69, 129, 142] The formation of these modes leads to a modification of the plasmonic dispersion relation, and additional absorption (emission) pathways near and below the energy of the SiN_x phonon. Emission from the SPPP modes, however, should display some polarization dependence, which was not observed in Fig. 3.3b, and thus an increase in direct emission from the SiN_x layer likely plays the dominant role in creating the feature at 730 cm^{-1}.

To better understand and quantify the emission features observed in the graphene-SiN_x structure, we used a finite element method to calculate the electromagnetic power density ($\nabla \cdot \mathbf{S}$) associated with plane waves incident on 40 nm graphene nanoresonators on an SiN_x/Au substrate. The parameters for our computational model were equivalent to those described in Chapter 2.3, where the optical absorption of the device was modeled.[134]

Because $\nabla \cdot \mathbf{S}$ reveals where power is absorbed, it therefore also indicates where far field thermal emission originates, and an increase in $\nabla \cdot \mathbf{S}$ indicates an enhancement of the spontaneous emission intensity of the thermally excited dipoles.[134] The results of these simulations are shown in Fig. 3.4a at 1357 cm^{-1}, corresponding to the resonant energy of the graphene plasmon mode when the carrier density is set to 1.2×10^{13} cm^{-2}. It can be seen in this figure that there is a marked increase in the amplitude of $\nabla \cdot \mathbf{S}$ near the graphene nanoresonator. On resonance, there is a significant amount of power absorbed directly into the graphene, and it can also be seen that there is a large amount of absorption in the SiN_x in the immediate vicinity of the nanoresonator, where the fields of the graphene plasmon mode extend. To further distinguish the relative contributions to thermal emission, we integrate the power densities at 1357 cm^{-1} over the graphene, the SiN_x within the plasmon mode volume, and the remaining SiN_x. We calculate the mode volume of our structure as $V_{eff} = \int u dV / u_0$, where the numerator is the total stored energy and u_0 is the electromagnetic-energy density at the emitter position, chosen to be sitting directly atop the resonator. We define the boundary of the mode to be centered about the graphene resonator along a contour of constant electric field (E_x). In Fig. 3.4b, we show results for undoped and doped nanoresonators. For undoped graphene, we observe weak power absorption in the SiN_x near the graphene nanoresonator, and we see only interband transitions contributing to absorption in the graphene itself. As the carrier density is increased to 1.2×10^{13} cm^{-2}, absorption in the graphene and the nearby SiN_x increases due to excitation of the confined plasmonic mode. The absorption in the bulk of the SiN_x layer shows little dependence on graphene carrier density, except at low frequencies, near 730 cm^{-1}, where absorption decreases with carrier density due to changes in the reflection coefficient at the surface, as described above. We note that our finite element model does not account for the non-radiative processes discussed in other work.[143] Our model indicates how graphene plasmons interact with a homogenous, lossy medium but not the manner in which individual dipoles interact with the graphene sheet, which is another source of non-radiative quenching.

3.1.4 Radiated Power and Device Considerations

In order to quantify the thermally radiated power of this structure, we consider Planck's law for spectral radiance using the black soot as a reference with $\varepsilon = 1$, and including our 50 x 50 μm^2 collection area and the 1.51 steradians covered by the 0.65 NA objective. This calculation yields a maximum thermal power modulation of 50 pW/cm^{-1} at 1360 cm^{-1} (7.1 μm) for 40 nm resonators at 250°C doped to a carrier density of 1.2×10^{13} cm^{-2}. These calculations indicate that a 1 x 1 mm^2 device could act as an electronically controllable mid-IR source that would modulate 2 μW of power over 100 cm^{-1} of bandwidth. This compares favorably to commercial mid-IR LEDs at 7 μm, which emit 1.25 μW over similar bandwidths (IoffeLED, Ltd. OPLED70Sr). The percent change in emitted power at the resonant plasmonic frequency is 7.5%, a value that reflects the large background contribution due to SiN_x phonons as well as the low mobility of the graphene sheet, the polarization of the plasmon-assisted radiation, and the low dielectric strength of the SiN_x at elevated temperatures. Figure 3.4 shows that while the SiN_x phonons play some role in contributing to the plasmon-assisted radiation, the majority originates in the graphene sheet itself. Thus, by choosing a substrate with a low optical phonon density at the resonant plasmon frequency, such as diamond-like carbon (DLC),[69] the background signal could be reduced without significantly suppressing the plasmon-assisted radiation, leading to a larger modulation depth of the emitted power. We also note that the maximum temperature and gate bias applied in these experiments was not limited by the graphene but by the SiN_x dielectric, which is known to exhibit Poole-Frenkel tunneling at high temperatures.[136] By choosing a dielectric that can withstand higher temperatures, such as SiO_2 or DLC, devices displaying larger power modulation could be fabricated. Finally, devices fabricated with higher mobility graphene, less edge roughness and with circular resonator geometries (i.e. non-polarized) have been predicted theoretically[135] to exhibit tunable absorptivity/emissivity that can vary from 0 to 1 (i.e. zero to total absorption) within a narrow frequency range. Such devices would display changes in absorptivity that equal or exceed those provided by electrochromic devices,[144] while also providing potential for more operation cycles, and higher temperature and higher speeds of operation.

In addition to providing utility as a tunable mid-IR source, the physics by which this device operates is distinctly different from conventional laser or LED sources. Because thermal radiation is a form of spontaneous emission, the emission rate is increased by the presence of the plasmonic cavity, with the degree of rate enhancement is dictated by the ratio between the Q factor and mode volume of the optical cavity (i.e. the Purcell factor).[145] This effect has been explored as a means of increasing LED switching rates by placing the semiconductor emitting layer within either a plasmonic or photonic cavity.[146-150] For the case of graphene plasmonic nanoresonators that have highly confined mode volumes, the Purcell factor has been shown to be extremely high, approaching 10^7, and thus, the modulation rate of thermal emission from our device could be exceedingly fast, beyond what has been demonstrated with plasmonically enhanced LEDs or lasers.[151] For the device demonstrated here, where the switching and detection speeds are limited by a large electrical RC time constant, and the slow operation speeds of our FTIR-based detector, kHz switching speeds can be demonstrated, presented in Figure 3.5. However, careful device design, where the capacitance is minimized and lower resistance contacts are used, could allow for the creation of a mid-IR emitter with ultrafast switching times and a broad range of tunability.

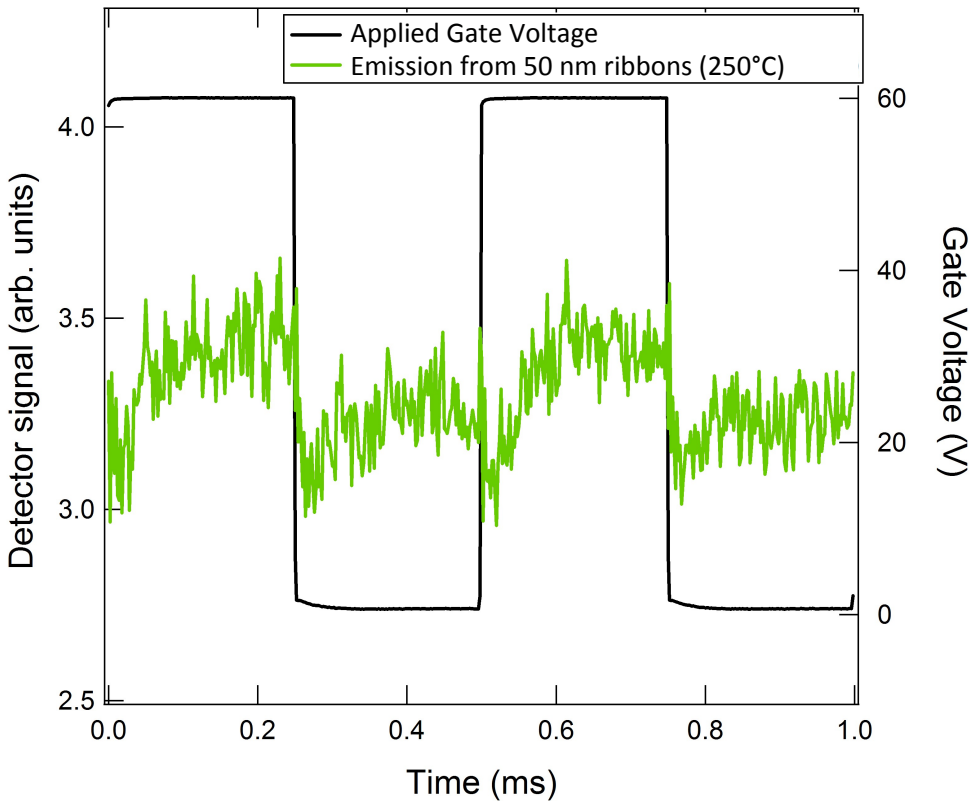

Figure 3.5: kHz modulated emission signal. Temporal waveform of applied voltage signal (black line) and detector signal of emission from 50 nm ribbons at 250°C (green line). A voltage of 60 V corresponds to a doping level of 1.2×10^{13} cm^{-2}, resulting in a positive detector signal. A voltage of 0 V corresponds to the charge neutral point of the graphene and therefore the measurement of an 'off' signal.

3.2 Electronic Control of Polarized Emission

3.2.1 Introduction

In order to gain full, active control over emitted infrared light, one would like to control not just amplitude, as discussed in the previous section, but additionally polarization and phase (the latter of which will be addressed in Chapters 4 and 7). With this additional layer of control, metasurface polarizers that filter or emit specific polarization states of light may be realized, which can be modulated in real time.

Metasurfaces have recently been utilized to selectively reflect or absorb specific polarization states of light, as well as to convert the polarization state of light[152-161]. However, none of these structures have been demonstrated to actively modulate the

polarization state of light using electrostatic gating, limiting their ultimate utility in reconfigurable photonic devices. In this work, we demonstrate that by taking advantage of the gate-tunability of graphene plasmons, and the two free parameters (width and Fermi energy), active control of the polarization state of light may be achieved in a single structure.

3.2.2 Design of Dual-Resonant Structure for Polarization Control

We design a resonant cavity inspired by the Salisbury Screen concept described in Chapter 2, wherein graphene nanoresonators of different widths are fabricated on a thick silicon cavity terminated with a gold back reflector, on which a thin insulating layer is transferred to allow active gate-tunability, shown schematically in Figure 3.6. Unlike the Salisbury screen, which takes advantage of the $\lambda/4n$ dielectric resonance (where n is the index of refraction of the cavity), we implement a design based on a thicker, high-index external cavity that supports higher order resonances that span the mid-infrared. In this way, we achieve two goals: the first to narrow the peak width of the resonance, and the second to decrease the free spectral range, both of which scale inversely with cavity thickness.

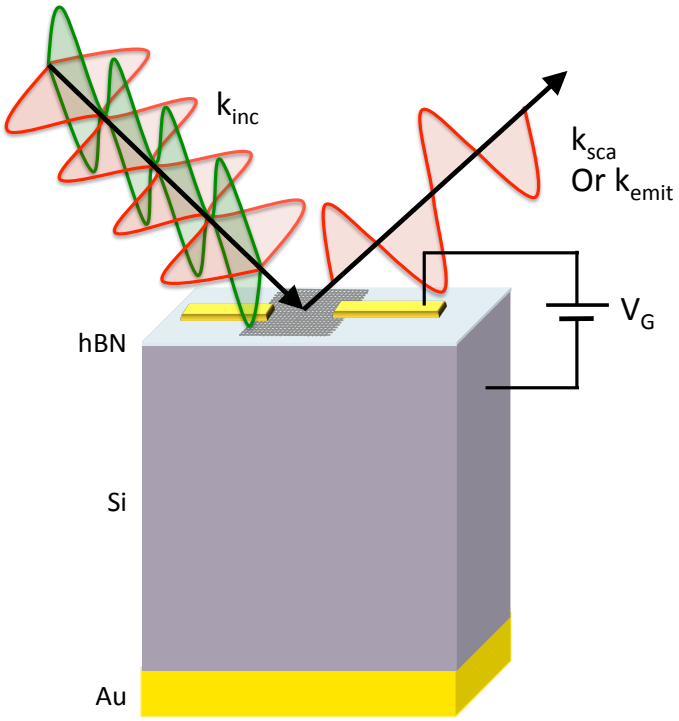

Figure 3.6: Schematic illustration of graphene-dielectric dual resonant structure for controlling the polarization state of reflected or emitted infrared light. A 7.5 μm thick Si cavity with Au back-reflector results in enhanced absorption in the graphene nanoresonators at the surface.

By carefully selecting the carrier concentration and width of the graphene resonators, it is possible to match different resonators to the $m\lambda/4n$ dielectric resonances of the cavity, where m is an integer and n the cavity index of refraction, for which simulation results are shown in Figure 3.7 (See Appendix B for simulation parameters). We use 7.5 μm thick Si as the lossless dielectric for the mid-infrared, with a 7 nm thick hexagonal boron nitride (h-BN) gate dielectric sandwiched between the graphene nanoresonators and Si. 200 nm Au serves as a near-ideal back-reflector. The use of a thin h-BN layer allows for electrostatic modulation of the graphene plasmon, in addition to providing a substrate with a decreased density of surface charges, which may increase the graphene mobility.[162, 163]

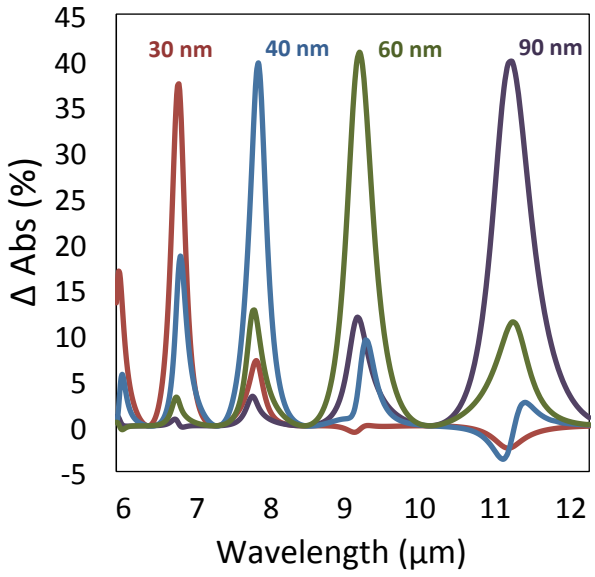

Figure 3.7: Graphene absorption at E_F = 0.4 eV normalized to E_F = 0 eV for different nanoresonator widths. High order dielectric resonances of the silicon cavity are matched to the plasmon resonances.

Of most interest in this geometry is the selective enhancement of absorption for different resonator widths matched to specific cavity modes. This enables excellent spectral control of absorption with narrow absorption/emission features that can be switched on and off on demand. Moreover, due to the strong dependence of the graphene plasmon frequency on carrier concentration described in previous chapters, it is possible to identify multiple conditions of enhanced absorption by taking advantage of the relations $\omega_p \propto W^{-1/2}$ and $\omega_p \propto |E_F|^{1/2}$. An example of this is shown in Figure 3.8, wherein a graphene resonator of 60 nm is well-matched to the external cavity resonance ($11\lambda/4n$) for E_F = 0.45 eV, but poorly matched to this for E_F = 0.3 eV. The exact opposite trend is observed for a resonator width of 40 nm: for E_F = 0.45 eV, minimal absorption is observed, but for E_F = 0.3 eV, the plasmon absorption is strongly enhanced. This suggests that we may establish a "switching" behavior between 40 nm and 60 nm ribbons by changing the graphene Fermi energy.

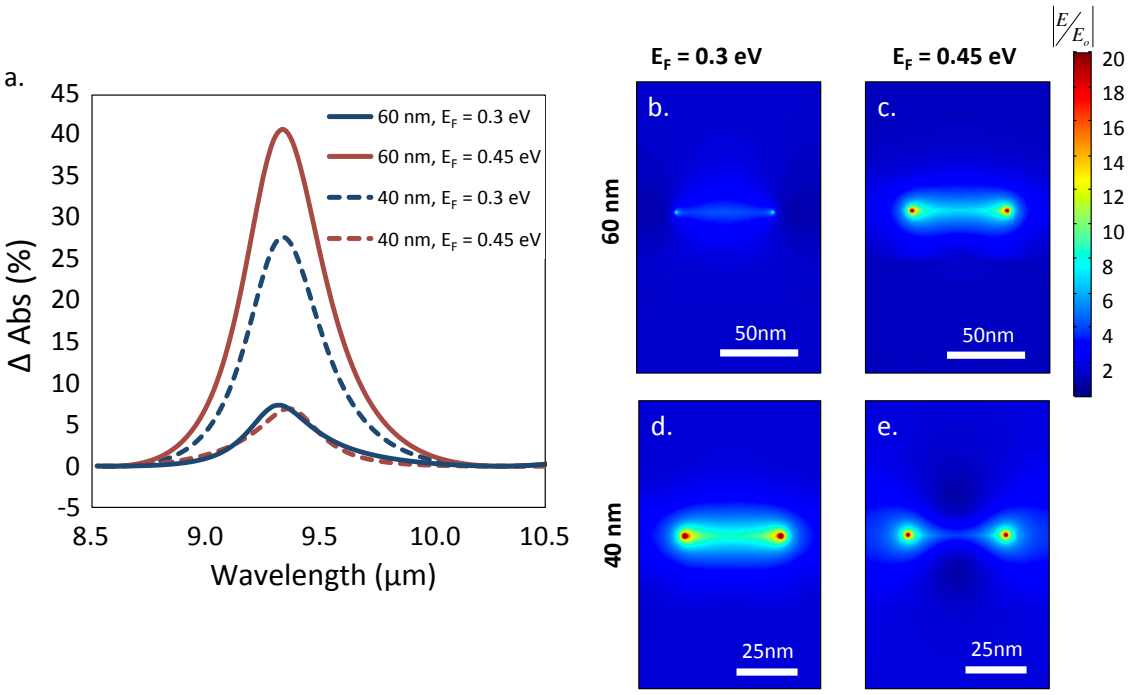

Figure 3.8: (a) Tunable absorption in graphene resonators of selected widths (40 and 60 nm) and Fermi energies (0.3 and 0.45 eV) for selectively enhanced absorption. (b – e) Field profiles for each width/E_F combination at a wavelength of 9.34 μm.

We can therefore take advantage of this Fermi energy tuning to realize active polarization control of infrared light: by designing a crossed structure comprised of 40 and 60 nm resonators, absorption (and therefore emission) can be enhanced in each arm by switching the graphene Fermi energy from 0.3 to 0.45 eV, shown in Figure 3.9. Moreover, by carefully selecting the dimensions of the unit cell, amplitude compensation can be done to create approximately equal 'on' and 'off' states for E_x and E_y polarizations.

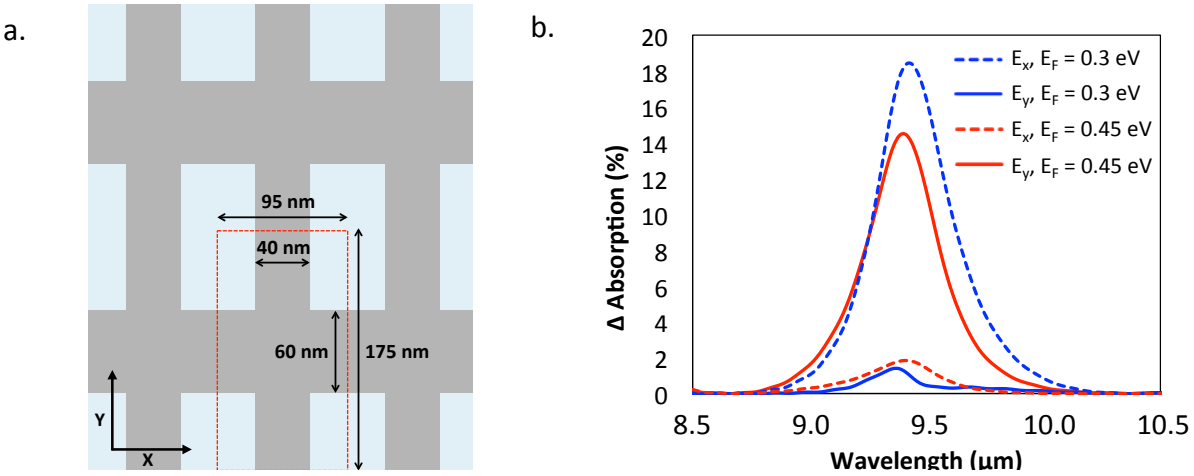

Figure 3.9: (a) Geometry of graphene crosses for polarization switching and corresponding absorption, (b), normalized to E_F = 0 eV for X and Y polarizations as defined in the reference frame of the schematic.

Samples are now being fabricated to experimentally realize these designs. Silicon-on-insulator (SOI) wafers are purchased from Ultrasil with 7.5 μm thick device layers, 200 nm SiO_2 (as an etch stop layer), and 300 μm thick handles. Electron beam lithography is used to expose a window on the backside of the handle, and XeF_2 is used to etch through to the SiO_2. Hydrofluoric acid (HF) is used to remove the SiO_2 layer, leaving a suspended Si membrane. Au is then deposited on the backside and h-BN is transferred on the top. Graphene is then transferred on top of the h-BN and 100 keV electron beam lithography is used to pattern the ribbon or crossed structures.

3.3 Conclusions and Outlook

In conclusion, we have demonstrated that by combining the width- and carrier concentration-dependent plasmon resonance of graphene nanoresonators with external cavity designs, active control of the spectral intensity and polarization state of absorbed and emitted light may be realized. We experimentally demonstrate kHz modulation of emitted intensity in the mid-infrared and present simulations and calculations to explain the emission control as arising from antenna-coupled enhancement based on graphene

plasmons. We have shown that by taking advantage of dual-resonant structures, it is possible to create devices with ‘designer’ thermal radiation profiles, useful for thermal camouflage or infrared light sources. In future works, it may be of interest to additionally control the phase of emitted radiation for emission-type metasurfaces. Moreover, these experiments suggest that graphene may also be a very interesting material for controlling near-field heat transfer.

C h a p t e r 4

PHASE MODULATION AND ACTIVE BEAM STEERING WITH GRAPHENE-GOLD METASURFACES

"To invent, you need a good imagination and a pile of junk."
– Thomas Edison

Chapter 4.1

1. Michelle C. Sherrott*, Philip W. C. Hon*, Katherine T. Fountaine, Juan C. Garcia, Samuel M. Ponti, Victor W. Brar, Luke A. Sweatlock, Harry A. Atwater, "Experimental Demonstration of >230° Phase Modulation in Gate-Tunable Graphene-Gold Reconfigurable Mid-Infrared Metasurfaces", Nano Lett., **2017**, *17* (5), pp 3027–3034
(***Equal author contributors**)
DOI: 10.1021/acs.nanolett.7b00359

Metasurfaces offer significant potential to control far-field light propagation through the engineering of amplitude, polarization, and phase at an interface. We report here phase modulation of an electronically reconfigurable metasurface and demonstrate its utility for mid-infrared beam steering. Using a gate-tunable graphene-gold resonator geometry, we demonstrate highly tunable reflected phase at multiple wavelengths and show up to 237° phase modulation range at an operating wavelength of 8.50 μm. We observe a smooth monotonic modulation of phase with applied voltage from 0° to 206° at a wavelength of 8.70 μm. Based on these experimental data, we demonstrate with antenna array calculations an average beam steering efficiency of 23% for reflected light for angles up to 30° for this range of phases, confirming the suitability of this geometry for reconfigurable mid-infrared beam steering devices. By incorporating all non-idealities of the device into the antenna array calculations, including absorption losses which could be mitigated, 1% absolute efficiency is achievable up to 30°. We design and fabricate a 28-pixel meta-device based on this design for realizing active beam steering.

4.1 Experimental Demonstration of >230° Phase Modulation in Gate-Tunable Graphene-Gold Reconfigurable Mid-Infrared Metasurfaces

4.1.1 Introduction

Metasurfaces have been demonstrated in recent years to be powerful structures for a number of applications including anomalous reflection[164], focusing/lensing[4, 5], and more complex functionalities such as polarization conversion, cloaking, and three-dimensional image reconstruction[12-16], among others[11, 17-21]. These functionalities are accomplished through careful engineering of phase fronts at the surface of a material, where geometric parameters of resonant structures are designed to scatter light with a desired phase and amplitude. However, all of these structures have functions that are fixed at the point of fabrication, and cannot be transformed in any way. Therefore, significant effort has been made in the community to develop metasurfaces that can be actively modulated. There exist numerous examples of metasurface designs which enable active control of reflected or transmitted amplitude, taking advantage of different technologies including MEMS, field-effect tunability, and phase change materials[89, 165-168], discussed further in recent reviews of the state-of-the-art in metasurfaces[20, 169-172].

For mid-infrared (mid-IR) light, graphene has been demonstrated as an ideal material for active nanophotonic structures for a number of reasons, including its low losses in the mid-IR and its intermediate carrier concentration (10^{12} - 10^{13} cm^{-2}), placing its plasma frequency in the IR – THz regime[68, 173-176]. Additionally, since it is atomically thin and has a linear density of electronic states, its charge carrier density can be easily modulated via electrostatic gating in a parallel plate capacitor configuration[63, 177-179]. Its corresponding complex permittivity can therefore be modulated over a wide range, potentially at GHz speeds. Recent works have demonstrated that the incorporation of graphene into resonant gold metasurfaces can also be used to significantly modulate absorption profiles, operating at MHz switching speeds[89]. This has been accomplished by either the un-assisted modulation of the graphene dielectric constant, or by exploiting the strong confinement of light by a graphene plasmon excited between metal edges to enhance the sensitivity of the design to the graphene's optical constants.[88, 167] Additional examples have used the tunable

permittivity of graphene to modulate the transmission characteristics of a variety of waveguide geometries[94, 180].

Despite the significant progress that has been made, an important requirement for power efficient, high-speed, active metasurfaces is electrostatic control of scattered phase at multiple wavelengths, which has not been adequately addressed experimentally in the mid-IR. In gaining active control of phase, one can engineer arbitrary phase fronts in both space and time, thereby opening the door to reconfigurable metasurface devices. This is particularly necessary as classic techniques for phase modulation including liquid crystals and acousto-optic modulators are generally poorly-suited for the IR due to parasitic absorption in the materials used[181, 182], in addition to being relatively bulky and energy-expensive in comparison to electrostatic modulators. Similarly, though 60° phase modulation based on a VO_2 phase transition has been demonstrated at 10.6 μm, the phase transition occurs over relatively long time scales and the design is limited in application due to the restricted tunability range[183]. Finally, recent works on the electrostatic control of phase in the mid-IR using graphene-integrated or ITO-integrated resonant geometries are limited to only 55° electrostatic phase tunability at 7.7 μm[184] and 180° tunability at 5.95 μm[185], respectively. In this work, we overcome these limitations and experimentally demonstrate widely-tunable phase modulation in excess of 200° with over 250 nm bandwidth using an electrostatically gate-tunable graphene-gold metasurface (see Figure 4.1). We highlight a smooth phase transition over 206° at 8.70 μm and sharper, but larger, phase modulation of 237° at 8.50 μm, opening up the possibility of designing high efficiency, reconfigurable metasurface devices with nanosecond switching times. By measuring this active tunability over multiple wavelengths in a Michelson interferometer measurement apparatus, we present evidence that this approach is suitable for devices that can operate at multiple wavelengths in the mid-IR.

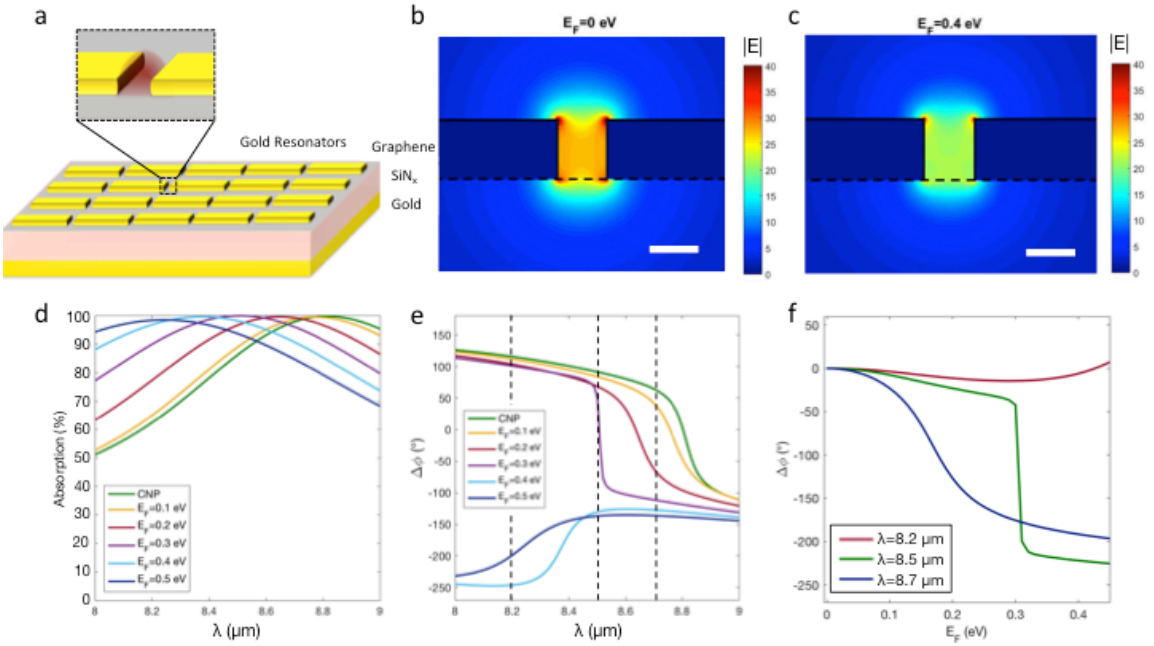

Figure 4.1: Tunable resonant gap-mode geometry. (a) Schematic of graphene-tuned antenna arrays with field concentration at gap highlighted. Resonator dimensions: 1.2 μm length by 400 nm width by 60 nm height, spaced laterally by 50 nm. SiN_x thickness 500 nm, Au reflector thickness 200 nm. (b, c) Field profile in the antenna gap shows detuned resonance at different E_F at a wavelength of 8.70 μm. Scale bar is 50 nm. (d) Simulated tunable absorption for different graphene Fermi energies. (e) Simulated tunable phase for different graphene Fermi energies. (f) Phase modulation as a function of Fermi energy for three different wavelengths – 8.2 μm, 8.5 μm, 8.7 μm.

4.1.2 Design of Resonant Phase-Shifting Structure

Our tunable phase metasurface design is based on a metasurface unit cell that supports a gap plasmon mode, also referred to as a patch antenna or 'perfect absorber' mode, which has been investigated previously by many groups[100, 186-188], shown schematically in Figure 1a. Absorption and phase are calculated as a function of Fermi energy (E_F) using COMSOL FEM and Lumerical FDTD software (see Appendix B). A 1.2 μm length gold resonator on graphene is coupled to a gold back-plane, separated by 500 nm SiN_x. At the appropriate balance of geometric and materials parameters, this structure results in near-unity absorption on resonance, and a phase shift of 2π. This may be considered from a theoretical perspective as the tuning of parameters to satisfy critical coupling to the metasurface[187]. This critical coupling occurs when the resistive and radiative damping modes of the structure are equal, thereby efficiently transforming incoming light to resistive losses and

suppressing reflection. This condition is possible at subwavelength spacing between the gold dipole resonator and back-plane, when the resonator is able to couple to its image dipole moment in the back-reflector, generating a strong magnetic moment. The magnetic moment, in turn, produces scattered fields that are out of phase with the light reflected from the ground plane, leading to destructive interference and total absorption. This may be considered the plasmonic equivalent of the patch antenna mode.

In order to enhance the sensitivity of the structure to the tunable permittivity of the graphene, these unit cells are arrayed together with a small (50 nm) gap size to result in significant field enhancement at the position of the graphene, as shown in Figures 4.1b and 4.1c. This is critical for enhancing the in-plane component of the electric field to result in sensitivity to the graphene's optical response. Therefore, as the Fermi energy of the graphene is modulated, changing both the inter- and intra-band contributions to its complex permittivity, the resonant peak position and amplitude are shifted, as shown in Figures 1d and 1e. Specifically, the intraband contribution to the permittivity is shifted to higher energies as the plasma frequency of the graphene, ω_p increases with the charge carrier density as $\omega_p \propto n^{1/4}$. Additionally, as E_F increases, Pauli blocking prevents the excitation of interband transitions to energies above $2E_F$, thereby shifting these transitions to higher energy. The net effect of these two contributions is a decrease of the graphene permittivity with increasing carrier density, leading to a shift of the gap mode resonance to shorter wavelengths.

By taking advantage of graphene's tunable optical response, we obtain an optimized design capable of a continuously shifted resonance peak from 8.81 μm at E_F = 0 eV or Charge Neutral Point (CNP) to 8.24 μm at E_F = 0.5eV; a peak shift range of 570 nm. Correspondingly, this peak shift indicates that at a fixed operation wavelength of 8.50 μm, the scattered phase can be modulated by 225°, as seen in Figure 1f. This trend persists at longer wavelengths, with greater than 180° modulation achieved between 8.50 and 8.75 μm. At shorter wavelengths, such as 8.20 μm, minimal tuning is observed because this falls outside of the tuning range of the resonance. It is noteworthy that this phase transition

occurs sharply as a function of E_F at 8.50 μm because it falls in the middle of our tuning range, and becomes smoother at longer wavelengths. We therefore illustrate this smooth resonance detuning at a wavelength of 8.70 μm in Figure 4.1b and 4.1c, wherein we plot the magnitude of the electric field at different Fermi energies of the graphene. On resonance (Figure 4.1b), the field is strongly localized to the gap, and then as the Fermi energy is increased (Figure 4.1c), this localization decreases as the gap mode shifts to shorter wavelengths. These different responses are summarized at three wavelengths (8.2, 8.5, and 8.7 μm) in Figure 4.1f, where the phase response is plotted as a function of E_F.

4.1.3 Experimental Demonstration of Phase Modulation

We experimentally demonstrate the tunable absorption and phase of our designed structure using Fourier-Transform Infrared Microscopy and a mid-IR Michelson interferometer, respectively, schematically shown in Figure 4.2a. Graphene-gold antenna arrays are fabricated on a 500 nm free-standing SiN_x membrane with a gold back-plane. A Scanning Electron Microscope (SEM) image of the resonator arrays is presented in Figure 4.2b. An electrostatic gate voltage is applied between the graphene and gold reflector via the doped silicon frame to modulate the Fermi energy. Tunable absorption results are presented in Figure 4.2c demonstrating 490 nm of tunability from a resonance peak of 8.63 μm at the CNP of the graphene to 8.14 μm at E_F = 0.42 eV, corresponding to voltages of +90 V and -80V. This blue-shifting is consistent with the decrease in graphene permittivity with increasing carrier concentration, and agrees well with simulation predictions. Discrepancies between simulation and experiment are explained by fabrication imperfections, as well as inhomogeneous graphene quality and minor hysteretic effects in the gate-modulation due to the SiN_x and atmospheric impurities[189]. The shoulder noted especially at longer wavelengths is a result of the angular spread of the FTIR beam, wherein the use of a 15X Cassegrain objective results in off-normal illumination of the sample. We note that the processing of our sample in combination with the surface charge accumulated as a result of the SiN_x surface results in a significant hole-doping of the graphene, as has been observed in previous experiments[190]. Due to this heavy doping, we are unable to experimentally observe the exact CNP of the graphene using standard gate-dependent transport

measurement techniques, and therefore determine this by comparison to simulation. We then calculate the Fermi energy at each voltage using a standard parallel plate capacitor model.

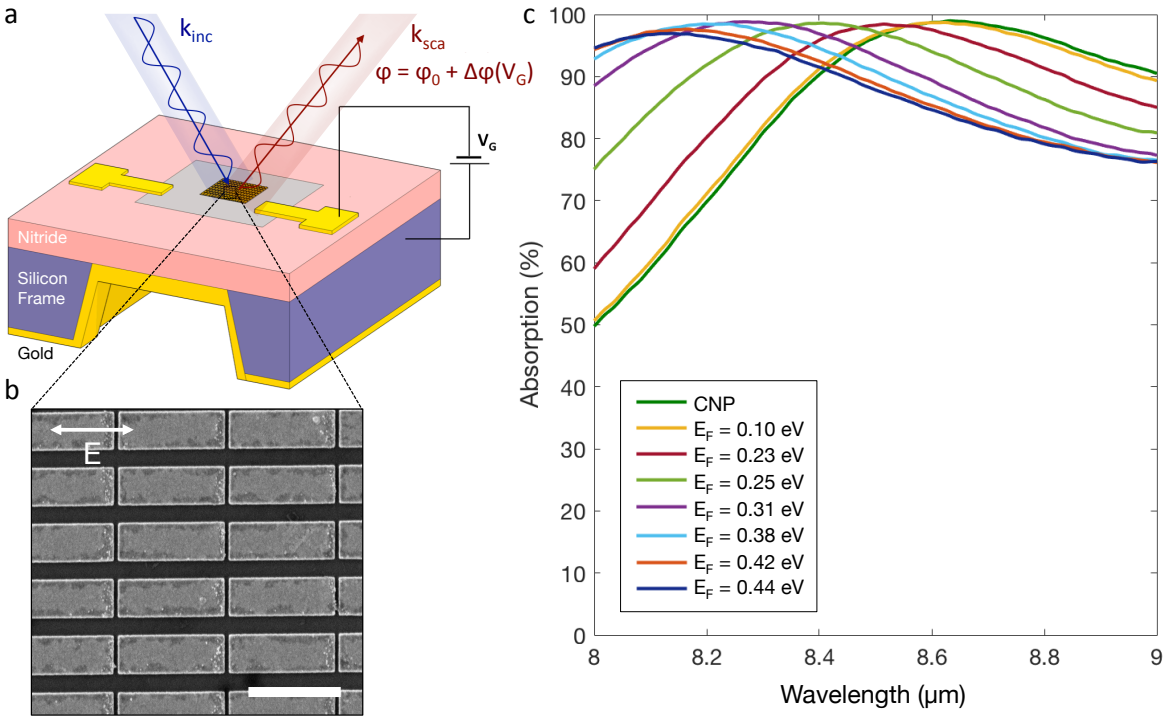

Figure 4.2: (a) Schematic of a gate-tunable device for control of reflected phase. (b) SEM image of gold resonators on graphene. Scale bar indicates 1 μm. (c) Tunable absorption measured in FTIR at different gate voltages corresponding to indicated Fermi energies. A peak shift of 490 nm is measured.

To experimentally characterize the phase modulation of scattered light achievable in our graphene-gold resonant structure, we use a custom-built mid-IR, free-space Michelson Interferometer, for which a schematic is presented in Figure 4.3a and explained in depth in the Appendix D. The integrated quantum cascade laser source, MIRcat, from Daylight Solutions provides an operating wavelength range from 6.9 μm to 8.8 μm, allowing us to characterize the phase modulation from our metasurface at multiple wavelengths. The reference and sample legs of the interferometer have independent automated translations in order to collect interferograms at each wavelength as a function of gate voltage.

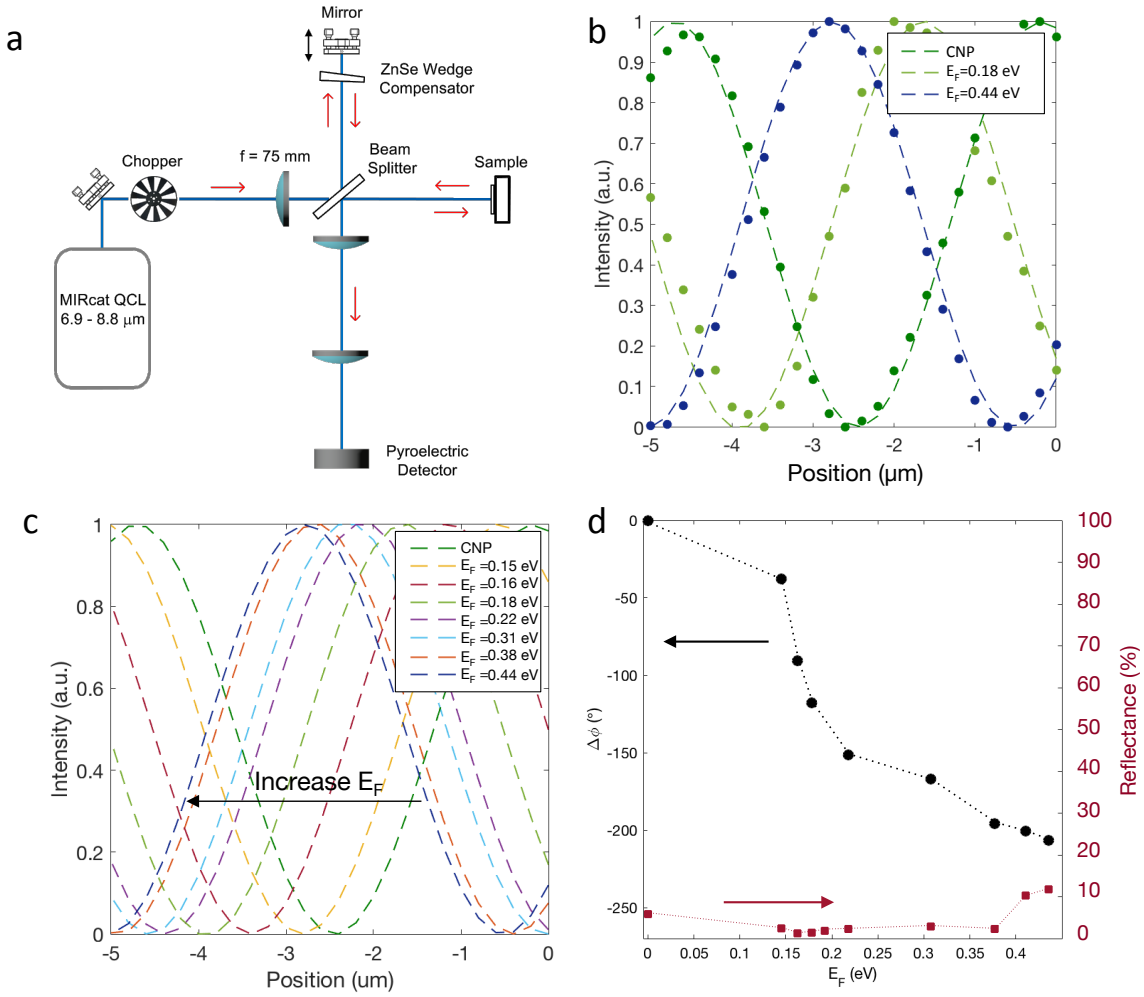

Figure 4.3: (a) Schematic of a Michelson interferometer used to measure reflection phase modulation. (b) Representative interferometer measurements for different Fermi energies with linear regression fits at a wavelength of 8.70 μm. (c) Interferometry data fitted for all E_F at 8.70 μm. (d) Extracted phase modulation as a function of E_F at 8.70 μm demonstrating 206° tuning and corresponding reflectance between 1.5 and 12%.

A comparison of the relative phase difference between interferograms taken for different sample biases is conducted to capture the phase shift as a function of E_F. At each Fermi energy, an interferogram for different reference mirror displacements is taken. Due to the different absorptivity at each doping level, each biases' interferogram is normalized to its own peak value. We then take the midpoint of the normalized interferogram amplitude as a reference, and a relative phase shift from one bias to the other is calculated by recording the

displacement between the two interferograms at the reference amplitude. Factoring that the sample leg is an optical double pass, the relative phase difference is given by equation 4.1:

$$\Delta\phi = \frac{720\Delta x}{\lambda} \tag{4.1}$$

where ΔΦ is the phase difference between different sample responses in degrees, Δx is the displacement between interferograms, and λ is the wavelength of operation. Data collected for three Fermi energies at 8.70 μm and fitted to a linear regression for extracting phase based on the above equation are presented in Figure 4.3b. For straightforward comparison, the phase modulation is presented relative to zero phase difference at E_F = 0 eV. Linear regression fits to the data for all Fermi energies measured at 8.70 μm are presented in Figure 4.3c, and the extracted phase as a function of E_F is presented in Figure 4.3d. Discrepancies between the experimental data and fits, particularly at CNP, can be explained by the decreased reflection signal from the sample due its strong absorption on resonance. We additionally plot the reflectance as a function of Fermi energy in Figure 4.3d. This relatively low reflectance is primarily a result of the large losses in the SiN_x substrate and low mobility graphene, and additionally arises from the resonant mode used to attain a large phase shift. However, this mode has been utilized to design high efficiency tunable and static metasurfaces[14, 191], and the high losses are not fundamental to its implementation in phase modulation. We suggest that by using lossless silicon as the dielectric instead of SiN_x, and an insulating layer of h-BN (which is also lossless at the wavelengths considered here) to improve the mobility of the graphene, much higher reflection efficiencies could be realized.

To further highlight the broad utility of our device, phase modulation results are presented in Figure 4.4a at multiple wavelengths: 8.20, 8.50, and 8.70 μm. At an operating wavelength of 8.70 μm, continuous control of phase is achieved from 0° relative at CNP to 206° at E_F = 0.44 eV with excellent agreement to simulation. At 8.50 μm, this range increases to 237°, much greater than any observed in this wavelength range previously, though as noted above, the transition is very sharp. At the shorter wavelength of 8.20 μm, a modulation range of 38° is achieved, with excellent agreement to simulation,

demonstrating the different trends in phase control this structure presents at different wavelengths. Simulation parameters are presented in Appendix B. Deviation is primarily due to hysteresis effects in the nitride gate dielectric and sample inhomogeneity (e.g., bilayer graphene patches, polymer residue from fabrication, and cracks in the graphene). We summarize the experimental and simulation results at all wavelengths between 8.15 μm and 8.75 μm in Figure 4.4b, wherein we plot the tuning range at each wavelength, defined as the maximum difference of scattered phase between CNP and E_F = 0.44 eV. This Fermi energy range is limited by electrostatic breakdown of the SiN_x gate dielectric. By using high-k dielectric materials, such as HfO_2, this range could be improved. We can therefore highlight two features of this structure: at longer wavelengths, we observe experimentally a smooth transition of phase over more than 200°, and at slightly shorter wavelengths, we can accomplish a very large phase tuning range with the tradeoff of a large transition slope. It is also noteworthy that more than 200° active tunability is achieved between 8.50 μm and 8.75 μm, which is sufficient for active metasurface devices in the entire wavelength range.

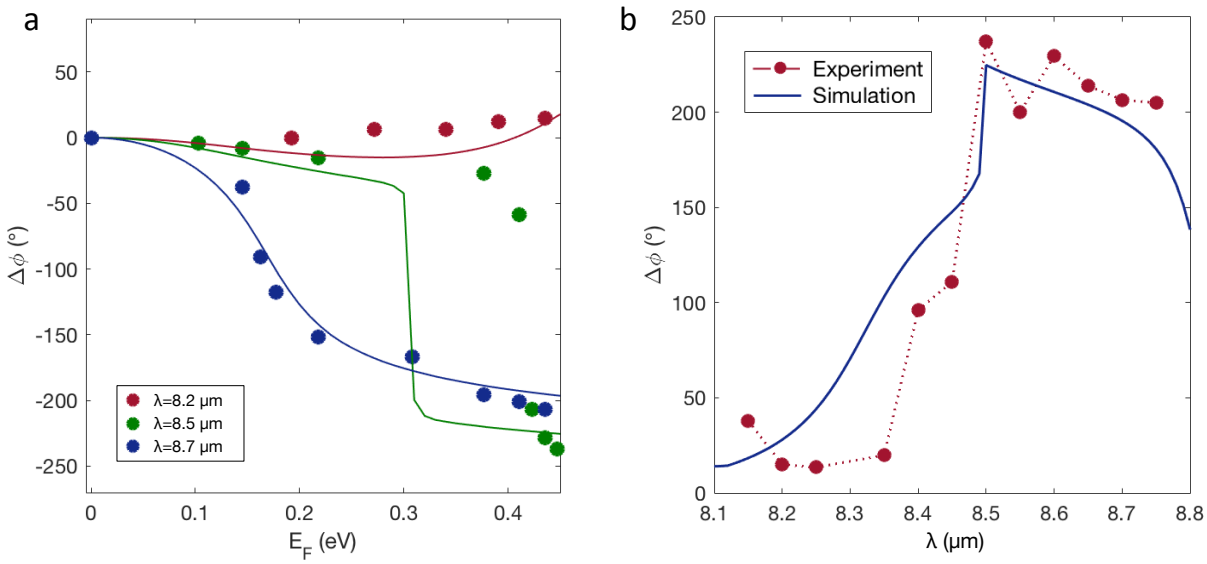

Figure 4.4: Demonstration of phase modulation over multiple wavelengths. (a) Phase modulation at wavelengths of 8.2 μm, 8.50 μm, and 8.7 μm (circles – experiment, line – simulation). (b) Maximum phase tuning achievable at wavelengths from 8.15 um to 8.75 um, simulation and experiment indicating up to 237° modulation.

4.1.4 Beam Steering Calculations

To illustrate the applicability of our design to reconfigurable metasurfaces, we calculate the efficiency of beam steering to different reflected angles as a function of active phase range for a linear array of independently gate-tunable elements as shown schematically in Figure 4.5a. We choose a linear array with polarization orthogonal to the steering direction to ensure minimal coupling between neighboring elements and a pitch of 5.50 μm to suppress spurious diffracted orders at a wavelengths of 8.50 μm. To quantify the beam steering feasibility of this metasurface, we frame the analysis in the formalism of antenna array theory, where the array can be considered as a discretized aperture. The far-field radiation pattern of such a discretized aperture can be analytically calculated by independently considering the physical array configuration (radiating element layout) and the radiating element properties, such as its amplitude, phase, and element far-field radiation pattern. For a general two-dimensional array, the far-field radiation pattern is given by the array factor weighted by the element's radiation pattern. The element pattern can be considered a weighting factor in the calculation of the far-field radiation pattern, where the array factor is only a function of the element placement and assumed isotropic radiators with a complex amplitude and phase. For relatively omnidirectional radiating elements, as in our case, the array factor captures the primary radiation pattern features, such as the main beam direction, main beam half power beam width (angular width of the main beam noted at half the main beam peak intensity), and major side lobes, reasonably well. The array factor for a general two-dimensional configuration is given as:[192]

$$AF(\theta,\varphi) = \sum_{n=1}^{N}\sum_{m=1}^{M} I_{mn} e^{j\alpha_{mn}} e^{j\gamma_{mn}} \tag{4.2}$$

$$\alpha_{mn} = -\beta[x'_{mn}\sin\theta_0\cos\varphi_0 + y'_{mn}\sin\theta_0\sin\varphi_0] \tag{4.3}$$

$$\gamma_{mn} = \beta\hat{r}\cdot\hat{r}'_{mn} = \beta[x'_{mn}\sin\theta\cos\varphi + y'_{mn}\sin\theta\sin\varphi] \tag{4.4}$$

where θ_0 and ϕ_0 are the elevation and azimuthal values of the main beam pointing direction, respectively, α_{mn} represents the element imparted phase that controls the beam direction, γ_{mn} represents the path length phase difference due to the element position $\hat{r}'_{mn}$ and the unit vector $\hat{r}$ from the array center to an observation angle, θ, φ. β is the free space propagation

constant, I_{mn} is the complex element amplitude and the double summations represent the row and column element placement of a general two-dimensional array.

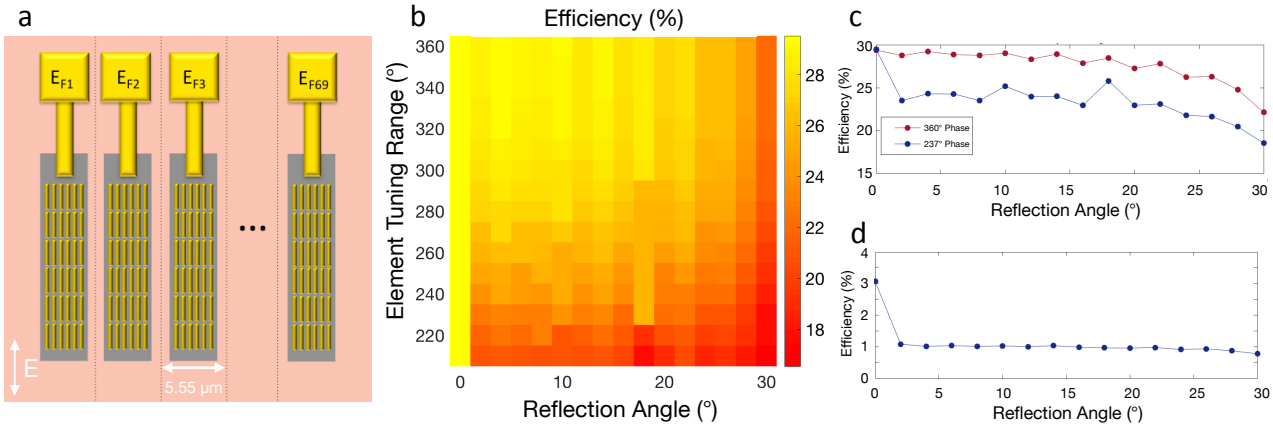

Figure 4.5: Calculation of proposed reconfigurable metasurface based on experimentally realized design. (a) Schematic of beam steering device, where each of the 69 unit cells is assigned a different E_F. (b) Steering efficiency, η, for a 69 element metasurface with a lattice spacing of 5.55 μm illuminated with a plane wave at 8.60 μm. (c) Steering efficiency calculated for 360° and 237° phase modulation with unity reflectance. (d) Steering efficiency for 215° phase modulation incorporating simulated absorption losses.

Considering only the array factor, we can analytically capture the beam steering characteristics of a metasurface as a function of the achievable element phase tuning range. In the microwave regime, where the achievable element phase tuning range is greater than 270°, beam attributes such as its pointing direction and side lobe levels, can be quantified as a function of the phase discretization; the phenomenon is known as quantization error[193]. Independent of quantization errors, it is informative to understand the consequence of an element phase tuning range well below the desired ideal 360°. We define a figure of merit, the beam efficiency η, to be the ratio of the power in the half power beam width (of the steered main beam) for a given phase tuning range relative to the total power of the entire beam from -90 to 90° for unity amplitude and 360° phase tunability, which gives the total power possible from the aperture. In our analysis we consider maximum phase tuning ranges as low as 200° and desired scan angles up to +/-30° relative to surface normal. For

phase ranges below 200°, the undesirable side lobes will equal or exceed the intensity of the primary beam and main beam pointing errors exceeding one degree can exist; therefore, we restrict our analysis for phase ranges greater than 200°. In a simplified analysis, a one-dimensional array is assumed (Fig. 4.5a). Since the focus of the analysis is only on the consequence of a limited element phase tuning range, the element amplitude is initially assumed to be equal and unity. Assuming a fine enough gating step size, a virtually continuous sampling of a given element phase tuning range, is possible and therefore quantization error is not an issue. In this analysis, for a calculated element phase value that was unachievable, the closest phase value achievable was assigned. Namely, either an element phase value of 0° or the maximum phase for the considered element phase tuning range. As shown in Figure 4.5b, regardless of the element phase tuning range, the main beam scanning direction of zero degrees represents the trivial case where a zero difference in beam efficiency is expected because all elements exhibit the same reflected phase (zero phase gradient along the metasurface). The analysis illustrates the trade space and allows us to quantitatively assess the effect of the experimentally verified phase range of 237° at 8.50 μm. For consideration of the influence of a non-ideal phase range, we present in Figure 4.5c a comparison of the steering efficiency of our designed metasurface with 360° and 237° phase tuning ranges, showing a small decrease due to the limited range up to 30° steering angle. Up to ±30°, an efficiency greater than 18% is calculated, with an average efficiency of 23%. Below this phase range, lower efficiency steering is observed; however, we note that down to 200°, the steered main beam signal still exceeds the intensity in the other lobes. We note that the fluctuating trends observed as a function of reflection angle are a result of the incomplete phase range, which manifests differently depending on the deviation from the ideal phase gradient needed.

This clearly illustrates the necessity of achieving at least 200° in active phase control in order to create viable reconfigurable metasurfaces. In addition, it is noteworthy that this calculation includes an assumption of all intermediate phase values being available, meaning that a smoothly varying phase response as a function of gate voltage is necessary, as demonstrated in our device. This highlights the potential applications of our structure to

metasurface devices, in which independently gateable elements can be used to generate arbitrary phase gradients in time and space.

To further analyze the applicability of our structure to real beam steering applications, we calculate the steering efficiency incorporating the absorption losses of our measured device. We perform this calculation using simulated reflectance and phase at a wavelength of 8.6 μm due to the smoothly varying phase observed here; although a larger phase range is predicted at shorter wavelengths, its sharp transition translates to a difficult realization of intermediate phase values, and therefore we sacrifice some phase modulation in exchange for necessary smoothness. The achievable efficiency is on average 1% up to ±30°, presented in Figure 4.5d. We note that all calculations presented in Figure 4.5 were calculated for an operation wavelength of 8.6 μm for ease of comparison.

4.2 Multi-Element Graphene-Gold Meta-Device for Active Beam Steering

The realization of active modulation of phase in graphene-gold metasurfaces exceeding 180° presented in the previous section opened an unprecedented capability to realize fully electrically reconfigurable meta-devices for beam steering. In this section, we design and fabricate a 28-element tunable meta-device for beam steering in the mid infrared, based on the unit cell presented above. We use 28 elements for ease of experimental realization. An optical image of the completed is presented in Figure 4.6a below. Multi-stage aligned electron beam lithography is used to define the graphene-gold resonators and then electrically isolate each pixel by using an oxygen reactive ion etch to remove the graphene between them (See Appendix A for details). 750 nm spacing is used to minimize electrostatic cross talk between elements, as shown in an SEM image in Figure 4.6b. A final aligned lithography step is used to define 5 nm Ti/250 nm Au electrical contacts to each isolated element.

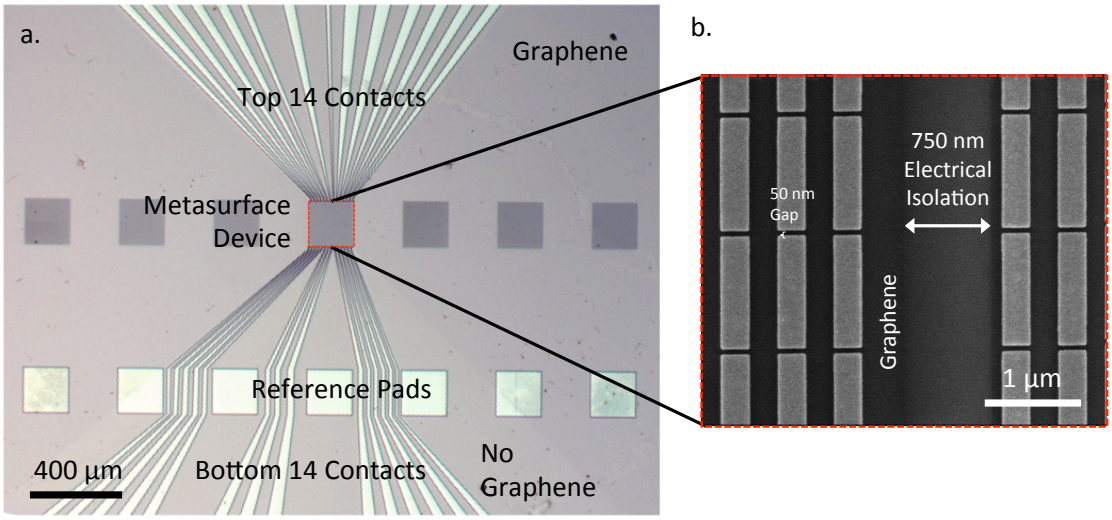

Figure 4.6: Fabricated tunable metadevice. (a) Optical microscope image of completed device with 28 independently gate-tunable elements. Other dark regions correspond to additional metasurface devices fabricated for performing a dose array to optimize the design. Gold reference pads are included for measurement ease. (b) Zoomed in SEM image of fabricated device showing gold resonators spaced by 50 nm and the electrical isolation between pixels.

We take advantage of a blazed grating style metasurface, using linear phase gradients of different pitches to redirect the reflected beam. These phase gradients approximate the saw tooth shape of a conventional blazed grating, wherein the reflection angle is selected by varying the pitch of the saw tooth. In the simplest implementation, we use the grating equation:

$$d\left(\sin\alpha+\sin\beta\right)=m\lambda \tag{4.5}$$

where d is the pitch of the repeat unit, α the incident angle (normal incidence for cases considered here), β the diffraction angle, λ the wavelength of incident light, and m the diffraction order (here we seek the first order peak).

This allows us to easily switch between reflection angles by varying the voltages applied to each pixel, and is more robust against phase errors (i.e., a phase range less than 2π). Two examples of designs being experimentally pursed currently are presented in Figure 4.7.

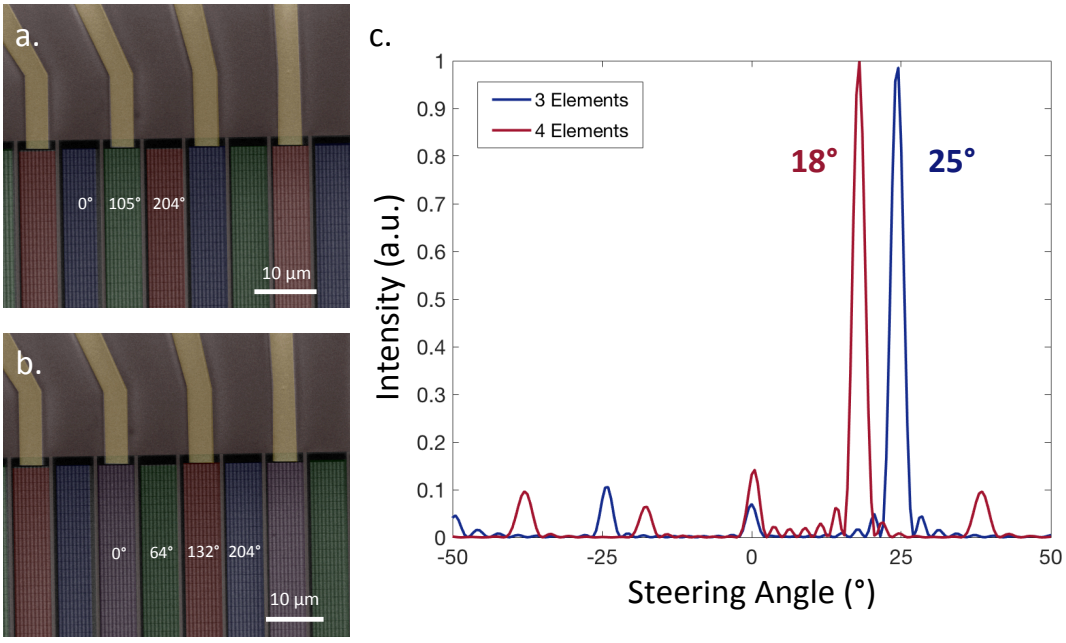

Figure 4.7: Beam steering designs for reconfigurable meta-device. (a) A three-element blazed grating style reflectarray with three phases of 0°, 105°, and 204° repeated across all 28 pixels. Steers to approximately 25°. (b) A four-element blazed grating style reflectarray with four phases of 0°, 64°, 132°, and 204° repeated across 28 pixels. Steers to approximately 18°. (c) Calculated steering angles for each configuration (a) and (b).

For the three-pixel repeat cell (d = 3 x 6.6 µm, λ = 8.5 µm) the grating equation yields a steering angle of 25°. For the four-pixel repeat cell, (d = 4 x 6.6 µm, λ = 8.5 µm), the grating equation yields a steering angle of 18°. These are in very good agreement with the results of full wave simulations presented in Figure 4.7c. We utilize the full range of achievable phases at 8.5 µm, with approximately equal spacing from 0° to 204°, corresponding to Fermi energies between 0 eV and 0.5 eV that we experimentally realized in the prior section with electrostatic gating. It is worth noting that, as discussed previously, for phase ranges below 180°, it is not possible to realize a steered beam of greater intensity than the side-lobes with steering error less than 1°.

Experimental work is ongoing with collaborators at Northrop Grumman to complete the characterization of the electrically reconfigurable metadevice that I have fabricated.

4.3 Conclusions and Outlook

In conclusion, we have demonstrated for the first time electrostatic tunability of phase from graphene gold antennas of 237° at a wavelength of 8.5 μm, more than 55° greater than has been demonstrated in the mid-IR in a different materials system. We additionally demonstrate phase modulation at multiple wavelengths, exceeding 200° from 8.50 to 8.75 μm. By calculating from antenna theory the fraction of power reflected to the desired angle as opposed to spurious side-lobes, we show that this design will enable beam steering with acceptable signal to noise ratio. We therefore conclude that this design is feasible for reconfigurable metasurfaces. We fabricate a 28-element tunable meta-device based on this design and present calculations for experimentally realizable beam steering configurations. These are particularly interesting for applications to LIDAR, a portmanteau of light and RADAR, which uses optical wavelengths to spatially map the environment with higher spatial resolution than is possible using radio waves. In LIDAR systems currently used in self-driving cars, a number of fixed-mount lasers and detectors are required to map the car's surroundings with sufficient speed and areal coverage. This results in very high costs. By using reconfigurable meta-devices, a much faster and less expensive form of LIDAR could be realized by electrically scanning reflected light over a wide angular range.

C h a p t e r 5

FIELD EFFECT OPTOELECTRONIC MODULATION OF QUANTUM-CONFINED CARRIERS IN BLACK PHOSPHORUS

"[Quantum mechanics] describes nature as absurd from the point of view of common sense. And yet it fully agrees with experiment. So I hope you can accept nature as She is - absurd."
-- Richard Feynman

1. William S. Whitney*, Michelle C. Sherrott*, Deep Jariwala, Wei-Hsiang Lin, Hans A. Bechtel, George R. Rossman, Harry A. Atwater, "Field Effect Optoelectronic Modulation of Quantum-Confined Carriers in Black Phosphorus", *Nano Lett.*, **2017**, *17* (1), pp 78–84
(*Equal author contributors)
DOI: 10.1021/acs.nanolett.6b03362

Few-layer black phosphorus is an appealing emerging van der Waals material, behaving like a naturally occurring quantum well with large in-plane anisotropy. In this chapter, we report measurements of the infrared optical response of thin black phosphorus under field-effect modulation. We interpret the observed spectral changes as a combination of an ambipolar Burstein-Moss (BM) shift of the absorption edge due to band-filling under gate control, and a quantum confined Franz-Keldysh (QCFK) effect, phenomena which have been proposed theoretically to occur for black phosphorus under an applied electric field. Distinct optical responses are observed depending on the flake thickness and starting carrier concentration. Transmission extinction modulation amplitudes of more than two percent are observed, suggesting the potential for use of black phosphorus as an active material in mid-infrared optoelectronic modulator applications.

5.1 Introduction

The emergence of a variety of two-dimensional materials has spurred tremendous research activity in the field of optoelectronics[194-197]. While gapless graphene can in principle exhibit an optoelectronic response at wavelengths ranging from the far infrared to the ultraviolet, its optoelectronic behavior is limited by a lack of resonant absorption and poor optical modulation in the absence of one-dimensional confinement. On the other hand, the

semiconducting molybdenum- and tungsten-based transition metal dichalcogenides have shown considerable prospects for visible frequency optoelectronics. Yet while these materials promise exciting new directions for optoelectronics and nanophotonics in the visible range, they have limited response for lower energy, infrared light.

The isolation of atomically thin black phosphorus in recent years has bridged the wavelength gap between graphene and transition metal dichalcogenides, as black phosphorus is an emerging two-dimensional semiconductor material with an infrared energy gap and typical carrier mobilities between those of graphene and transition metal dichalcogenides.[198-202] Since the first isolation of black phosphorus and demonstration of a field effect device, numerous reports investigating the synthesis and optoelectronic properties of this material have emerged, appropriately summarized in recent reviews.[198, 199, 203-205] Likewise a number of reports have also appeared on the applications of black phosphorus in fast photodetectors[206], polarization sensitive detectors,[207] waveguide integrated devices[208], multispectral photodetectors[209], visible to near-infrared absorbers[210] and emitters, [211-214] heterojunction[215] and split gate p-n homojunction photovoltaics[216], gate-tunable van der Waals heterojunctions for digital logic circuits[217, 218] and gigahertz frequency transistors in analog electronics[219]. A majority of the studies on both the fundamental optical properties of black phosphorus and applications in optoelectronic devices have explored only the visible frequency range[220-223]. Therefore, little is known about the intrinsic optical response of black phosphorus in the infrared range. As a narrow band-gap semiconductor, much of the potential for black phosphorus lies in these infrared optoelectronic applications – ranging from tunable infrared emitters[224] and absorbers for waste heat management/recovery[225] to thermophotovoltaics[226] and optical modulators for telecommunications[227]. Theoretical investigations of black phosphorus have suggested novel infrared optical phenomena, such as anisotropic plasmons[228, 229], field-effect tunable exciton stark shifts[230], and strong Burstein-Moss[231] and quantum-confined Franz-Keldysh effects[232] that promise to open new directions for both fundamental nanophotonics research and applications. In this work, we report the first experimental observations of the infrared optical response of ultrathin BP samples under field effect modulation. We observe

modulation of oscillations in the transmission spectra, which we attribute to a combination of an ambipolar Burstein-Moss shift and quantum-confined Franz-Keldysh behavior.

5.2 Experimental Design

Measurements were performed on black phosphorous flakes that were mechanically exfoliated in a glove box onto a 285 nm SiO_2/Si substrate. We analyzed three flakes of 6.5 nm, 7 nm, and 14 nm thickness, determined by Atomic Force Microscopy (AFM), and lateral dimensions of approximately 10 μm x 10 μm. A schematic of our experimental setup is shown in Figure 5.1a. Standard electron beam lithography and metal deposition methods were used to define Ni/Au electrodes to each exfoliated BP flake, described in Appendix E. The samples were then immediately coated in 90 nm PMMA for protection against environmental degradation. Once encapsulated in PMMA we observe minimum degradation of our samples to ambient exposure as verified by Raman spectroscopy[233] and reported in literature precedent[234]. Transmission measurements were obtained via Fourier Transform Infrared (FTIR) Spectroscopy. All optical measurements were done in a Linkam cryo-stage at a pressure of 3 mTorr and a temperature of 80 K. First, a room-temperature gate-dependent source-drain current was measured to extract approximate carrier densities as a function of gate bias. Transmission spectra were then gathered at different gate voltages applied between the flake and lightly doped Si substrate. We note that in our setup, the silicon substrate is grounded and BP experiences the applied voltage, so the sign of the applied voltages is reversed from the more common convention. In order to probe the electric field- and charge-carrier-dependent optical properties of the BP, all spectra were normalized to the zero-bias spectrum. The measured infrared optical properties result primarily from the unique band structure of thin BP, schematically depicted in Figure 5.1b. Quantized inter sub-band transitions provide the primary contribution to its zero-field optical conductivity.

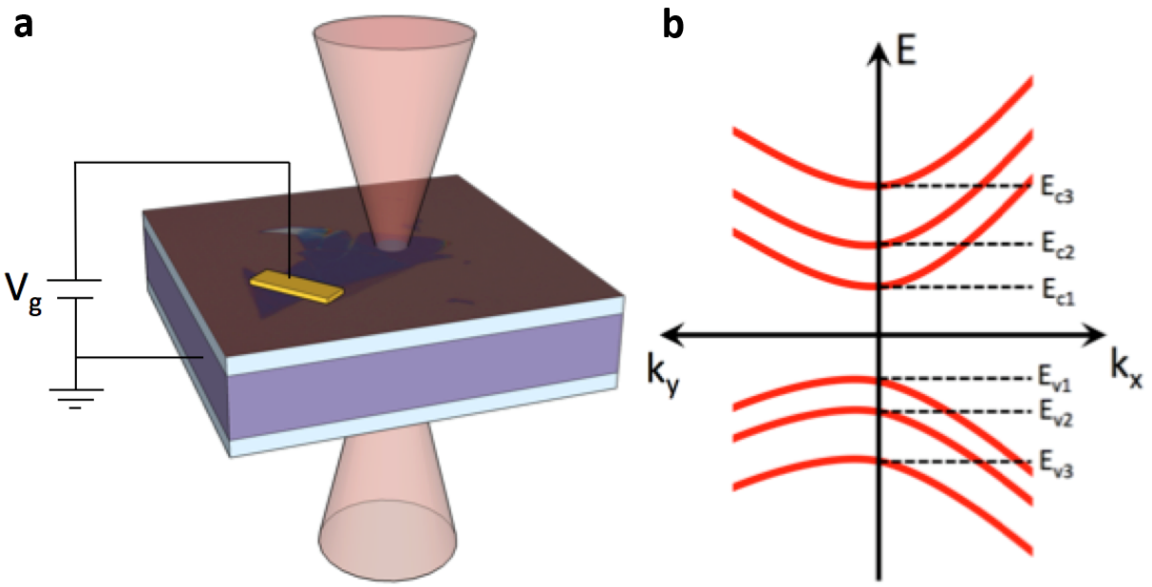

Figure 5.1: (a) Schematic illustration of transmission modulation experiment. Broadband mid-IR beam is transmitted through black phosphorus sample. Variable gate voltage applied across SiO_2 modulates transmission extinction. (b) Schematic band diagram of few-layer black phosphorus with subbands arising from vertical confinement

5.3 Tuning of Infrared Absorption in Few-Layer BP

5.3.1 BP Thickness #1

We first present results for the 7 nm thick BP flake, in Figure 5.2. An optical image is shown in Figure 5.2e. FTIR spectra were taken using a Thermo Electron iS50 FTIR spectrometer and Continuum microscope for which the light source is a broadband, unpolarized tungsten glow-bar. To improve signal/noise and minimize spatial drift, we surrounded the sample with a 150 nm thick gold reflector which also served as the gate electrode. The extinction modulation results are presented in Figure 5.2a. We observe two major features in this flake at energies of 0.5 eV (I) and 0.9 eV (II). The dip in extinction at 0.5 eV is present for both positive and negative gate voltages, as the sample is increasingly hole or electron doped, respectively. It grows in strength as the doping is further increased at larger gate-biases. The same trend is true for the feature at 0.9 eV, where a smaller peak in extinction modulation is observed for both polarities of voltage. This peak also is strengthened as the gate voltage is increased to +/- 120V. To gain insights into this behavior, we measure gate-dependent transport, using a scheme in which a positive bias

induces hole-doping, and a negative bias introduces electron-doping. We observe ambipolar transport at room temperature and atmospheric conditions, as shown in Figure 5.2b. Similar results have been shown in the literature with on/off ratios of ~10^4 for flakes thinner than the one considered here, at low temperature.[215, 235] From this, the CNP is observed to be at 20 V, and, using a standard parallel plate model the unbiased, n-type carrier concentration is estimated to be $1.5 \cdot 10^{12}$ cm^{-2}.

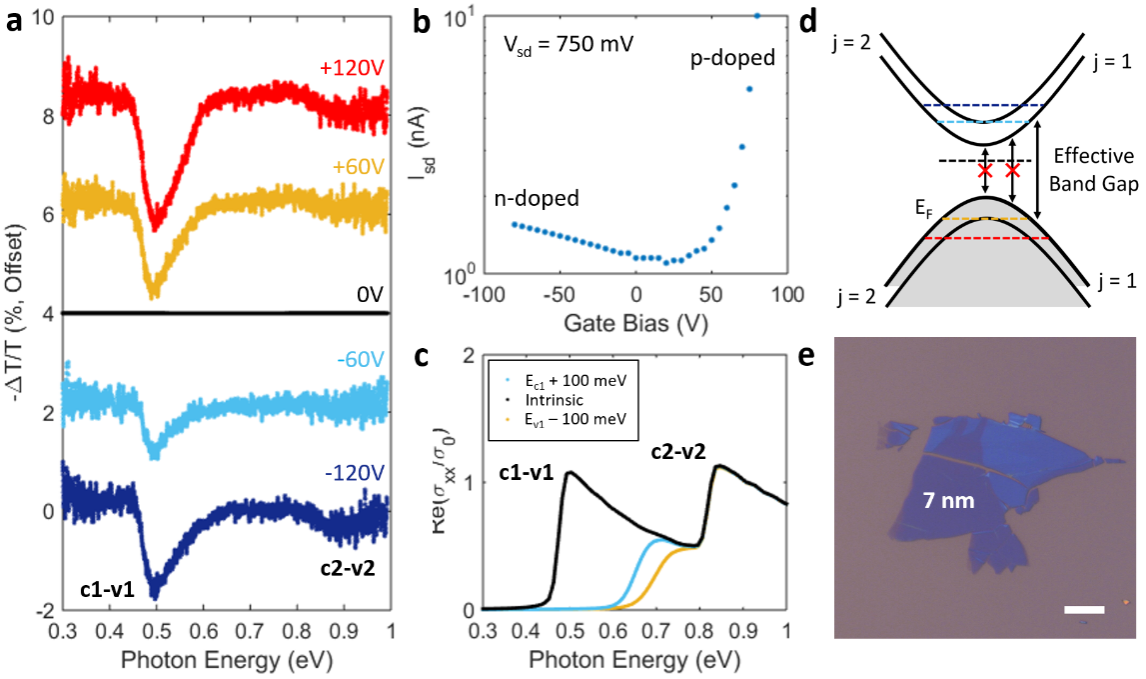

Figure 5.2: Gate modulation of lightly doped 7 nm flake. (a) FTIR transmission extinction vs photon energy normalized to zero bias. (b) Source-drain current vs gate voltage. Ambipolar conduction is seen. (c) Calculated optical conductivity of a 4.5 nm thick BP flake at different carrier concentrations, normalized to the universal conductivity of graphene. No field effects included. (d) Schematic of electronic band structure and allowed interband transitions at different voltages. (e) Optical microscope image of flake. Scale bar is 10 μm.

We can interpret our spectroscopic results with consideration of a Burstein-Moss shift, which is a well-known phenomenon in chemically doped narrow-band gap semiconductor materials. This effect, which changes the optical band gap of a semiconductor, results from band-filling. As the charge carrier density is increased and the Fermi level moves into the conduction or valence band, there are fewer unoccupied electronic states available, and

optical transitions to the occupied states are disallowed. This results in a decrease in the optical conductivity of the material at the energy of the transition, and is manifest in measurements as a decrease in absorption[236, 237]. Because this flake exhibits ambipolar transport behavior, we can explain both features (I) and (II) as arising from an ambipolar BM effect. At zero applied bias, the flake is very lightly doped, and all optical transitions are allowed. As a positive gate voltage is applied and the sample becomes hole doped, lower energy optical transitions become disallowed and the absorption of the flake decreases. Feature (I) corresponds to the band filling effect of the E_{11} intersubband transition, and feature (II) corresponds to the blocking of the E_{22} intersubband transition, shown schematically in Figure 2d. For a negative gate voltage, as the sample is electron-doped and the Fermi level moves into the conduction band, the E_{11} and E_{22} transitions are again blocked due to band filling, resulting again in a decrease in absorption. To support this explanation, we calculate the optical conductivity for the flake, as shown in Figure 5.2c to identify the appropriate energies of the intersubband transitions. To do so, we use the Kubo method described by Tony Low, et al.[231] The observed transitions energies are consistent with theoretical models that predict an increase in band gap energy from the bulk 0.3 eV value as the material thickness decreases to several layers or less.[222] This deviation from the bulk band gap indicates the influence of vertical confinement of charge carriers, a feature of the two-dimensionality of the material. We note that these transition energies suggest that the true thickness of our sample is thinner than 7 nm, at approximately 4.5 nm. This apparent variation between true and observed thickness from AFM topography is a result of surface oxidation, as has been recently reported.[238] The surface oxide on our samples is expected to be between 1-2 nm on either side, which appears inevitable despite following best practices, and is stable with no measurable degradation over an ambient exposure of > 18 hrs in ambient. It is noteworthy that we observe extinction modulation at relatively high photon energies, indicative of very large charge modulation taking place in the fraction of the BP nearest to the silicon oxide interface, with an accumulation/depletion layer that decays over the remainder of the flake. This is consistent with in-depth calculations of charge screening in BP using the Thomas-Fermi model done previously, reported by Tony Low, et al.[228] We estimate this screening length to be of order 3 nm for

our devices. This ambipolar, gate-modulated Burstein-Moss shift is the first observed in a two-dimensional semiconductor, to the best of our knowledge.

5.3.2 BP Thickness #2

We next present data for a BP flake of 14 nm thickness in Figure 5.3. An optical image is shown in Figure 3e. Extinction measurements are again taken with an iS50 FTIR spectrometer and Continuum microscope for which the light source is a tungsten glowbar. These results are presented in Figure 5.3a. Four prominent features are observed to modulate under application of a gate voltage, at energies of 0.35 eV, 0.41 eV, 0.55 eV, and 0.75 eV. As in the previous sample, they grow in strength with increased magnitude of the gate voltage, regardless of polarity. To better understand this behavior, we again measure gate-dependent transport, reported in Figure 4b. We observe ambipolar transport characteristics as in the previous flake, centered about a conductance minimum at approximately 20 V. Again using a parallel-plate capacitor model, we estimate an unbiased n-type carrier density of $1.5 \cdot 10^{12}$ cm^{-2} for a 20 V CNP.

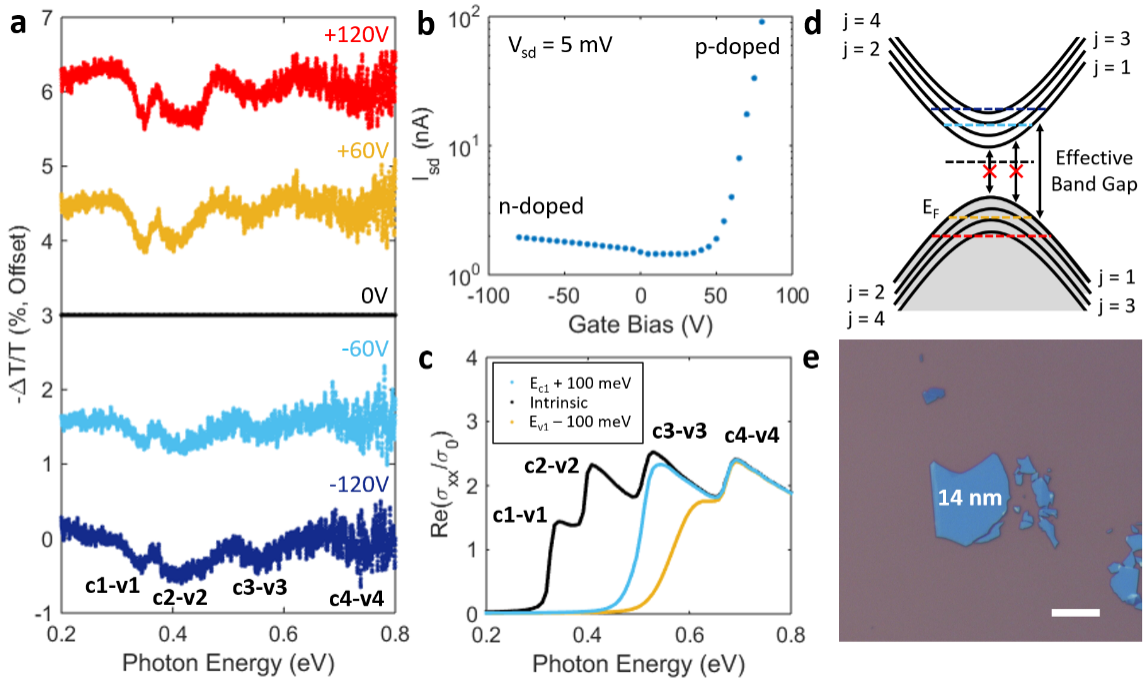

Figure 5.3: Gate modulation of lightly doped 14 nm flake. (a) FTIR transmission extinction vs photon energy normalized to zero bias (b) Source-drain current vs gate

voltage. Ambipolar conduction is seen. (c) Calculated optical conductivity of a 10 nm thick BP flake at different carrier concentrations, normalized to the universal conductivity of graphene. No field effects included. (d) Schematic of electronic band structure and allowed interband transitions at different voltages. (e) Optical microscope image of flake. Scale bar is 10 μm.

We propose that the optical modulation for this sample also results from an ambipolar Burstein-Moss effect. In this case, as the Fermi energy is moved into the conduction band of the BP under negative bias, transitions become disallowed and the transmission is increased at each of the $E_{11} - E_{44}$ energies. Under positive bias, as the Fermi energy is moved into the valence band, the band-filling effect of opposite charge carrier type results in negative extinction modulation peaks at the same energies of transitions $E_{11} - E_{44}$. As in the previous sample, we estimate an oxide layer of 1-2 nm has grown on our BP on either surface. Based on optical conductivity calculations presented in Figure 3c, we again estimate the adjusted thickness of our flake to be less than that measured by AFM, at approximately 10 nm. We further note that for this sample, the measurement extended beyond the area of the flake, to cover the flake and an area of bare silicon oxide roughly eight times the flake are. We thus suggest that the true modulation strength of this device is of order six percent, not the 0.75 percent indicated by the modulation of the entire area.

5.3.3 BP Thickness #3

Finally, results for the 6.5 nm thick flake are reported in Figure 5.4, for which an optical image is shown in Figure 5.4e. Unlike the previous two flakes, transmission measurements for this sample were taken using a Nicolet Magna 760 FTIR spectrometer coupled to a Nic-Plan infrared microscope on infrared Beamline 1.4.3 at the Advanced Light Source (ALS) at Lawrence Berkeley National Laboratory. This allowed us to perform measurements using a high brightness, diffraction-limited infrared beam, which is beneficial for accurately analyzing the small-area BP samples attainable by mechanical exfoliation. In contrast to the previous measurements, the incident light was elliptically polarized due to the synchrotron source, with an intensity ratio of two to one.

Figure 5.4a shows the primary result of this experiment, which is the modulated extinction of the sample at different voltages, normalized to the zero-bias extinction spectrum. Three prominent features are observed in these spectra. First, under negative applied bias (i.e.: when the sample is being depleted of holes), a negative peak (I) appears in transmission near 0.45 eV, which grows in amplitude and broadens to lower energies as the magnitude of the bias increases. Second, under positive applied bias (i.e., when the sample is being increasingly hole-doped), a positive peak (II) appears in transmittance near 0.5-0.7 eV. Lastly, these two effects, which we propose to depend on the Fermi level, are superimposed with an oscillatory feature (III) that varies with the magnitude of the applied field, but not its polarity, and which is most clearly visible in the negative bias spectra in the 0.5 - 0.7 eV range.

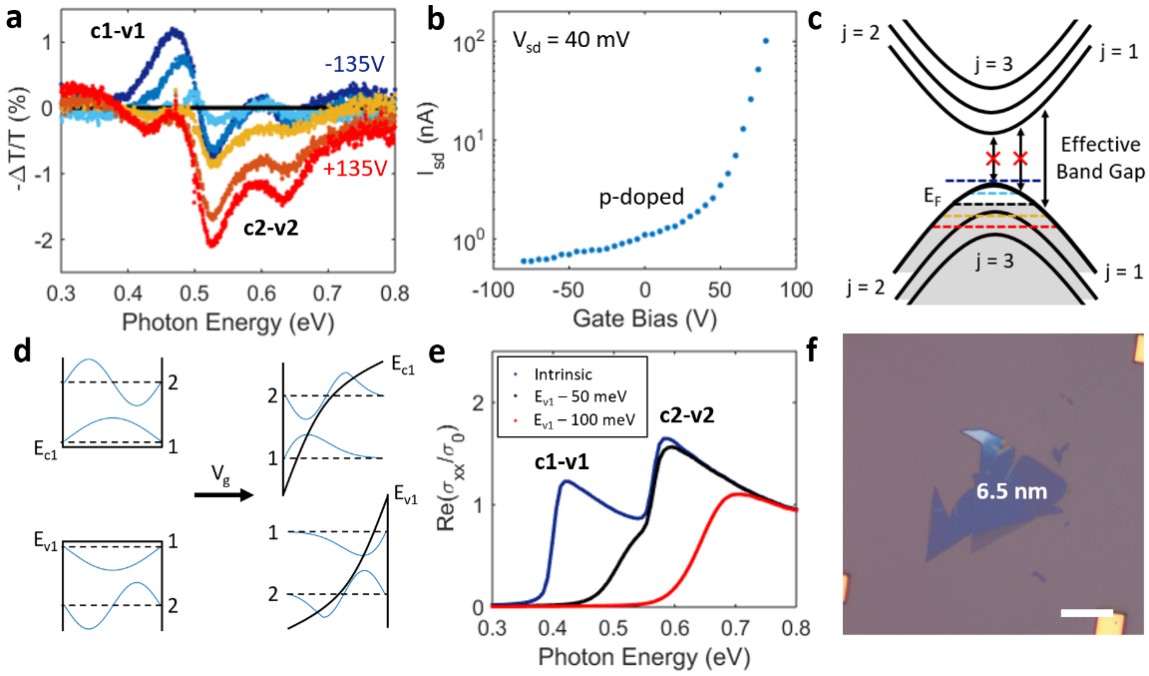

Figure 5.4: Gate modulation of a heavily doped 6.5 nm flake. (a) FTIR transmission extinction vs photon energy normalized to zero bias (b) Source-drain current vs gate voltage. Only hole-type conduction is seen. (c) Schematic of electronic band structure and allowed interband transitions at different voltages. (d) Schematic representation of quantum confined Franz-Keldysh Effect (e) Calculated optical conductivity of a 6.5 nm thick BP flake at different carrier concentrations, normalized to the universal conductivity of graphene. No field effects included (f) Optical microscope image of flake. Scale bar is 10 μp.

To better understand these results, transport measurements were again taken at room temperature under ambient conditions, as shown in Figure 5.4b. The gate dependence of the conductance indicates that, unlike the previous samples, this BP flake was initially heavily hole-doped, as ambipolar transport is not observed and only hole-type conduction is seen even at large negative bias.

Due to the distinct character of each feature and their relation to the transport measurements, we can understand the overall spectral shifts as arising from a combination of a Burstein-Moss (BM) shift and a quantum confined Franz-Keldysh (QCFK) effect, both of which have been predicted theoretically for gated BP flakes of this thickness.[232] In the bulk limit, the Franz-Keldysh effect refers to electron and hole wavefunctions leaking into the band gap, as described by Airy functions. This behavior introduces oscillatory features to the interband absorption spectrum, and redshifts the band edge. In confined systems, the quantum-confined Franz-Keldysh effect similarly modulates intersubband transitions.[239] As confinement becomes stronger and excitonic effects dominate, this phenomenon eventually gives way to the quantum-confined Stark effect. Because our flake exceeds a thickness of ~4 nm, we expect excitonic effects to be weak and therefore will not focus our discussion on the quantum-confined Stark effect or a normal-to-topological phase transition in our analysis.[222, 223, 230]

We suggest that peak (I) at 0.45 eV can be described by the onset of j = 1 intersubband transitions as the material is depleted of holes at negative gate voltages and the valence band is un-filled, in agreement with our transport measurements. We further suggest that peak (II) can be described primarily by the suppression of j = 2 inter sub-band transitions as more holes are accumulated in the flake at positive gate voltages. This behavior is shown schematically in Figure 4d, and is again supported by calculations of the optical conductivity of the flake for various doping levels, shown in Figure 4e. Our experimental results correspond to modulation of the calculated intersubband transitions only in part, suggesting that a simple Burstein-Moss shift is insufficient to explain this measurement. From these results, we assign the band gap energy of our flake to be approximately 0.4 eV.

Unlike our previous samples, the optical data indicates minimal oxide formation, as the E_{11} and E_{22} transition energies match well to theory for a 6.5 nm thick BP quantum well. Given we do not see the charge neutral point in transport, we do not assign a carrier density to this flake, but can say that with a charge neutral point of greater than -80 V, its p-type carrier density must be greater than $6 \cdot 10^{12}$ cm^{-2}.

We suggest that quantum-confined Franz-Keldysh effects lead to the appearance of the additional oscillatory spectral features we observe. Specifically, we point to the oscillations in the negative voltage extinction curves at energies above 0.5 eV – where Burstein-Moss considerations would predict zero modulation – and in the positive voltage extinction curves both in that same range – where Burstein-Moss behavior would predict only a single dip in extinction centered at the 0.575 transition energy – and at 0.45 eV. This oscillatory modulation increases with bias magnitude, but does not depend significantly on the sign of the bias – behavior which is consistent with shifting of the overlap of the first and second conduction and valence sub-band wavefunctions, as described by the quantum-confined Franz-Keldysh effect. This behavior is investigated theoretically for gated BP by Charles Lin, et al.[232] In addition, under a sufficiently strong electric field, hybrid optical transitions between sub-bands of different index (eg: E_{v1} to E_{c2}) that are nominally forbidden at zero field become allowed. In total, quantum-confined Franz-Keldysh effects in thin BP are expected to lead to behavior including redshifting of intersubband transitions, modification of intersubband selection rules (allowing hybrid transitions), or oscillatory, Airy function modulation of the absorption edge, all of which can be considered as consistent with our experimental observations. However, further theoretical work is needed to understand this effect satisfactorily; the same authors provide evidence in a more recent, experimental report that hybrid transitions may occur with zero applied field as well.[240] Interestingly, we see no evidence of a tunable plasma edge; investigations in the long-wave infrared wavelength range with larger samples would likely be needed to observe this feature. We suggest that far-infrared measurements on nanoresonators fabricated in few-layer BP might reveal gate-tunable plasmons, as was seen in monolayer graphene samples in Chapter 2.

The clear appearance of the QCFK effect in this measurement distinctly differs from our previous two samples, indicating that BP quantum wells of similar thickness may have very different optical responses. We suggest that the primary reason for this is that this flake is very heavily doped under zero bias, whereas our previous measurements were performed on nearly intrinsic flakes. In particular, in the intrinsic case, field strength and carrier concentration vary proportionally (i.e., under larger bias, there is a larger carrier concentration, and vice-versa). To the contrary, in our heavily doped sample, this proportionality is absent, leading to potentially competing effects and the clear emergence of oscillatory features. It is also worth noting that, while we see no clear evidence of the QCFK effect in our first two experiments, it is possible that the large BM shift is simply dominant over the QCFK effect, making the latter effect difficult to observe, or that our increased noise prevents the effect from obviously manifesting. A complete theoretical framework that addresses the interplay between zero-bias carrier concentration and field-effect has not yet been developed, and is beyond the scope of this paper. We also note that, while we see no clear evidence of excitonic effects, and it has been suggested theoretically and experimentally that such effects should not be present in flakes of this thickness, we do not rule out the possibility that they may be influencing our results.

We note that because of the complicated polarization state of incident light from the synchrotron, and because a previous study has extensively studied this effect experimentally[241], we do not address in detail the anisotropic optical properties of BP. However, due to the primary contribution to the optical conductivity arising from the σ_{xx} component, we argue that the only effect of elliptically polarized light is to scale the observed modulation.

5.4 Conclusions and Outlook

In conclusion, we have demonstrated experimentally that ultra-thin black phosphorus exhibits widely tunable, quantum well-like optical properties at mid-infrared wavelengths. In 7 and 14 nm, lightly doped flakes, we observe for the first time an ambipolar Burstein-Moss shift of intersubband transitions, which also varies with thickness as these transition

energies are changed. In a heavily doped 6.5 nm thick BP flake, modulation of infrared transmission takes place as a result of both a Burstein-Moss shift and additional, quantum-confined Franz-Keldysh effects. While our results verify some of the recent theoretical predictions about the electro-optical effects in few-layer BP, they also report new behavior and serve as motivation to further understand the BP optical response as function of sample thickness, doping and field. Our results indicate that BP is both an interesting system for exploring the fundamental behavior of quantum-confined carriers in two-dimensional semiconductors under field-effect modulation, and a promising candidate for tunable mid-infrared optical devices. While we do not see evidence of a plasma edge in the BP, we suggest that this should be present at lower energies; by adapting the nanoresonator geometry in Chapter 2, this may be measured. Moreover, due to the different effective masses along each crystallographic axis, these plasmons should appear at different wavelengths. It is possible that for certain carrier concentrations, the permittivity of the BP will be positive along one axis and negative along the other, supporting hyperbolic plasmon polaritons.

C h a p t e r 6

ELECTRICAL CONTROL OF LINEAR DICHROISM IN BLACK PHOSPHORUS FROM THE VISIBLE TO MID-INFRARED

"Thoroughly conscious ignorance is the prelude to every real advance in science."

– James Clerk Maxwell

1. **Michelle C. Sherrott*,** William S. Whitney*, Deep Jariwala, George R. Rossman, Harry A. Atwater, "Electrical Control of Linear Dichroism in Black Phosphorus from the Visible to Mid-Infrared", (***Equal author contributors)**
arXiv:1710.00131

The incorporation of electrically tunable materials into photonic structures such as waveguides and metasurfaces enables dynamic control of light propagation by an applied potential. While many materials have been shown to exhibit electrically tunable permittivity and dispersion, such as transparent conducting oxides (TCOs) and III-V semiconductor quantum wells, these materials are all optically isotropic. In this chapter, we report the first known example of electrically tunable linear dichroism, observed here in few-layer black phosphorus (BP). Building on results in Chapter 5, we measure active modulation of the linear dichroism from the mid-infrared to visible frequency range, suggesting BP is an ideal material system for actively controlling the complex polarization state of light – or even the propagation direction of surface waves – over a broad range of wavelengths. This novel phenomenon is driven by anisotropic quantum-confined Stark and Burstein-Moss effects and field-induced forbidden-to-allowed optical transitions, which we carefully separate via different gating schemes (something not addressed in the previous chapter). Moreover, we observe that these effects generate near-unity modulation of BP absorption for certain material thicknesses and photon energies. This suggests BP is a promising material for active infrared (and visible) nanophotonics.

6.1 Introduction

As photonic structures for controlling the near- and far-field propagation of light become increasingly complex and compact, the need for new materials that can exhibit unique, strong light-matter interactions in the ultra-thin limit is growing rapidly. Ultrathin van der Waals materials are especially promising for such applications, as they allow for the control of light at the atomic scale, and have properties that can be modulated actively using an external gate voltage[56, 242]. Of these, few-layer black phosphorus (BP) is particularly noteworthy due to its high electronic mobility, and a direct band gap that can be tuned as a function of thickness from 0.3 eV to 2 eV[34, 243]. This has enabled the realization of numerous optoelectronic devices with high performance, including photodetectors that can be easily integrated with other photonic elements such as waveguides[208, 244-248]. In addition to this static control, recent works using electrostatic gating and potassium ions have shown that the electronic band gap of BP may be tuned by an electric field. [249-251]

One of the most salient features of BP is its large in-plane structural anisotropy, leading to a polarization-dependent optical response[229, 252, 253] as well as mechanical[254], thermal[255], and electrical transport characteristics[256, 257] that vary with in-plane crystallographic orientation[258]. This optical anisotropy corresponds to a large, broadband birefringence[259], wherein the distinct optical index of refraction along each axis leads to a phase delay between polarization states of light. Moreover, mirror-symmetry in the x-z plane forbids intersubband optical transitions along the zigzag axis, and as a result, BP exhibits significant linear dichroism, wherein the material absorption depends strongly on the polarization state of exciting light[253, 260].

6.2 Experimental Isolation of Electro-Optic Effects

In this work, we experimentally demonstrate that the application of a static electric field enables the modulation of the linear dichroism of few-layer black phosphorus (BP). This response – which approaches near-unity modulation of the BP oscillator strength for some thicknesses and photon energies – is achieved by active control of quantum-confined Stark and Burstein-Moss effects, and of quantum-well selection rules. We observe anisotropic

modulation from the visible to mid-infrared (mid-IR) spectral regimes, behavior not seen in traditional electro-optic materials such as graphene[261], transparent conducting oxides[262, 263], silicon[264], and quantum wells[265]. This opens up the possibility of realizing novel photonic structures in which linear dichroism in the van der Waals plane can be continuously tuned with low power consumption, because the switching is electrostatic in nature. By controlling optical losses in the propagation plane, for example, efficient in-plane beam steering of surface plasmon polaritons or other guided modes is enabled. Moreover, a tunable polarizer could be realized by the tuning of the polarization state of light absorbed in a resonant structure containing BP. Because this modulation is strongest at infrared wavelengths, it could also enable control of the polarization state of thermal radiation[266-268].

In order to probe and distinguish the electro-optical tuning mechanisms evident in few-layer BP, we used a combination of gating schemes wherein the BP either floats in an applied field or is contacted, as shown in Fig. 6.1a and described further in Appendix E. Polarization-dependent optical measurements are taken aligned to the crystal axes, in order to probe the structural anisotropy shown in Fig. 6.1b. This enables us to isolate the contribution of charge-carrier density effects – i.e., a Burstein-Moss shift – and external field-effects – i.e., the quantum-confined Stark effect and control of forbidden transitions in the infrared – to the modulation of linear dichroism, qualitatively illustrated in Figures 6.1c and 6.1d[231, 249, 269, 270]. In the anisotropic Burstein-Moss (BM) shift, the optical band gap of the material is changed as a result of band filling and the consequent Pauli-blocking of intersubband transitions. As the carrier concentration of the sample is changed, the Fermi level moves into (out of) the conduction or valence band, resulting in a decrease (increase) of absorptivity due to the disallowing (allowing) of optical transitions[271, 272]. Because intersubband optical transitions are only allowed along the armchair axis of BP, this modulation occurs only for light polarized along this axis. In the quantum-confined Stark Effect, the presence of a strong electric field results in the leaking of electron and hole wave functions into the band gap as Airy functions, red-shifting the intersubband transitions energies[35]. In quantum well structures, this red-shifting is manifested for multiple subbands, and therefore can be observed over a wide range of energies above the

band gap. To assess the gate-tunable anisotropy of the optical response of BP, the armchair and zigzag axes, illustrated in Fig. 6.1b, of the samples considered are identified by a combination of cross-polarized visible microscopy, described in Appendix E, and either polarization-dependent Raman spectroscopy or infrared measurements, described below. Representative Raman spectra are presented for the visible frequency sample on $SrTiO_3$ in Figure 6.1e. The optically active armchair axis exhibits a maximum intensity of the A_g^2 resonant shift at 465 cm^{-1}, whereas this is a minimum for the zigzag axis[273].

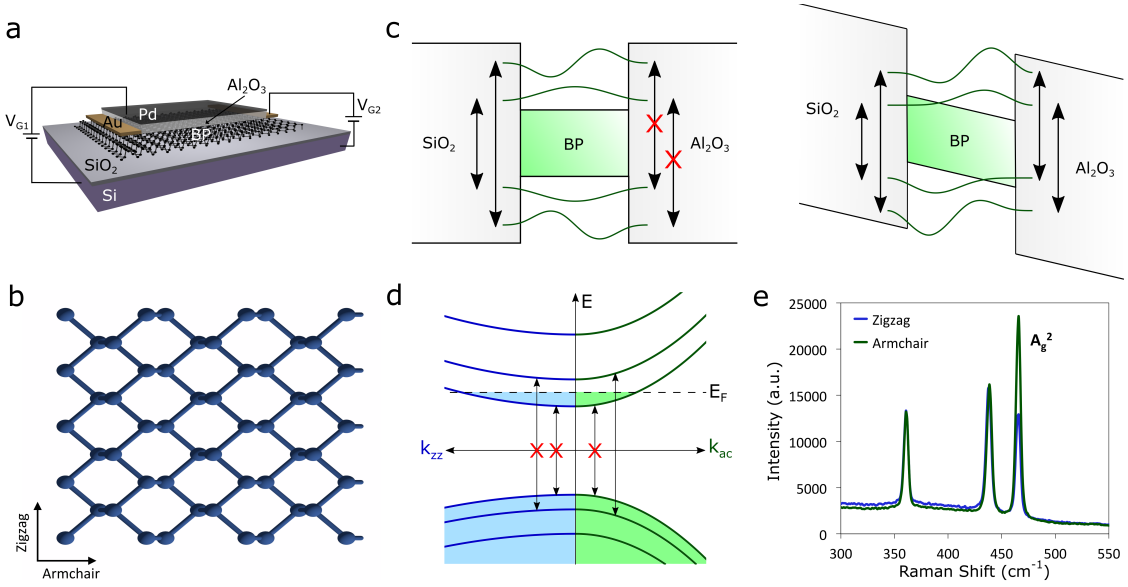

Figure 6.1: Anisotropic electro-optical effects in few-layer BP. (a) Schematic figure of infrared modulation devices. Few-layer BP is mechanically exfoliated on 285 nm SiO_2/Si and then capped with 45 nm Al_2O_3 by ALD. A semitransparent top contact of 5 nm Pd is used to apply field (V_{G1}) while the device floats and 20 nm Ni/200 nm Au contacts are used to gate (V_{G2}) the contacted device. (b) Crystal structure of BP with armchair and zigzag axes indicated. (c) Illustration of quantum-confined Stark effect and symmetry-breaking effect of external field. Under zero external field, only optical transitions of equal quantum number are allowed. An external field tilts the quantum well-like energy levels, causing a red-shifting of the optical band gap and allowing previously forbidden transitions. (d) Illustration of anisotropic Burstein-Moss shift in BP. Intersubband transitions are blocked due to the filling of the conduction band. Along the ZZ axis, all optical transitions are disallowed regardless of carrier concentration. (e) Raman spectra with excitation laser polarized along AC and ZZ axes. The strength of the A_g^2 peak is used to identify crystal axes.

To illustrate the mechanisms of tunable dichroism of BP in the mid-infrared, we measure modulation of transmittance using Fourier-Transform Infrared (FTIR) microscopy as a function of externally (V_{G1}) or directly applied bias (V_{G2}), presented for a 3.5 nm thick flake, as determined from atomic force microscopy (AFM), in Figure 6.2. Fig. 6.2a presents the raw extinction of the flake along the armchair axis at zero bias, obtained by normalizing the armchair axis to the optically inactive zigzag axis. A band edge of approximately 0.53 eV is measured, consistent with a thickness of 3.5 nm. A broad, weak shoulder feature is observed at approximately 0.75 eV. The corresponding calculated optical constants for the flake are presented in Figure 6.2c for comparison.

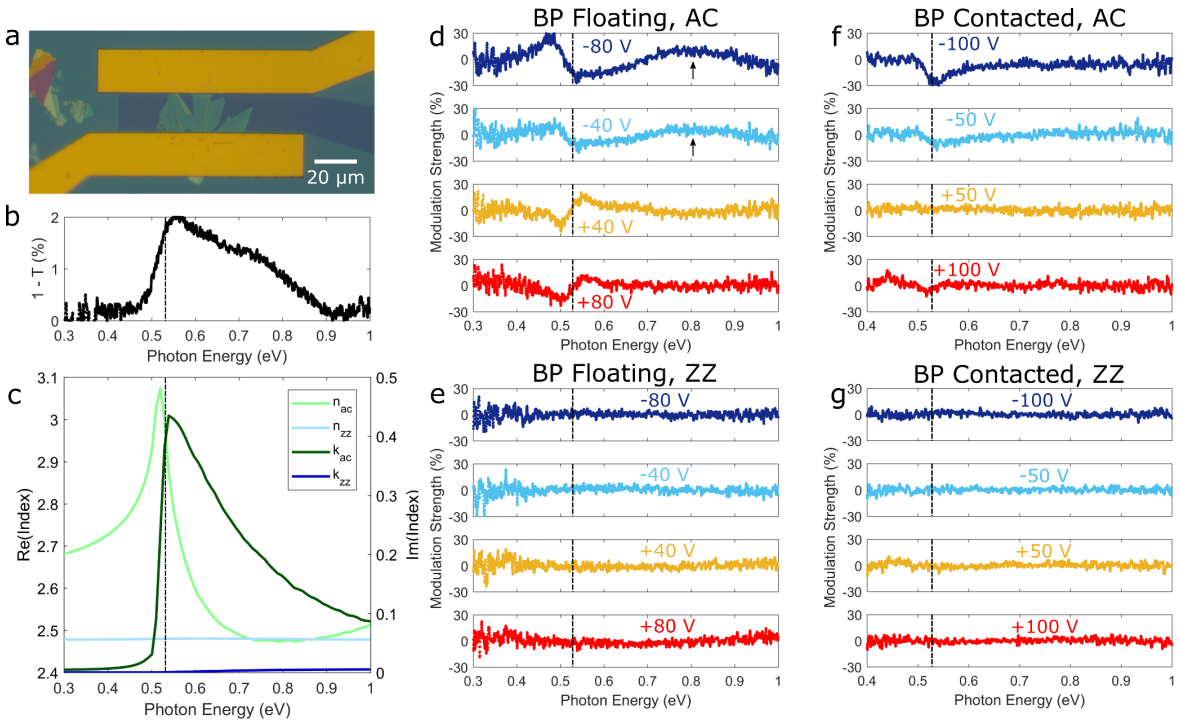

Figure 6.2: Electrically tunable linear dichroism: quantum-confined Stark and Burstein-Moss effects and forbidden transitions. (a) Optical image of fabricated sample. (b) Zero-bias infrared extinction of 3.5 nm flake, polarized along armchair (AC) axis. (c) Calculated index of refraction for 3.5 nm thick BP with a Fermi energy at mid-gap. (d) Modulation of BP oscillator strength with field applied to floating device, for light polarized along the AC axis. (e) Corresponding modulation for light polarized along the zigzag (ZZ) axis. (f) Modulation of BP oscillator strength with gating of contacted device, for light polarized along the AC axis. (g) Corresponding modulation for light polarized along the ZZ axis.

Figures 6.2d and 6.2e illustrate the influence of an external field on the extinction of BP with carrier concentration held constant (i.e., the BP is left floating). The extinction data for each voltage is normalized to the zero bias case and to the peak BP extinction seen in Figure 6.2b, to obtain a modulation strength percentage that quantifies the observed modulation of the BP oscillator strength. We note that this normalization scheme underestimates modulation strength away from the band edge, where BP extinction is maximal. Along the armchair axis, presented in Fig. 6.2d, two modulation features are measured near photon energies of 0.5 and 0.8 eV. We explain the first feature at 0.5 eV as arising from a shifting of the BP band edge due to the quantum-confined Stark effect. At negative bias, the band gap effectively shrinks and this is manifest as a redistribution of oscillator strength near the band edge to lower energies. As a result, an increase in absorptance is measured below the zero-bias optical band gap, and a decrease is seen above it. At positive bias, this trend is weakened and reversed. We propose two explanations for this asymmetry: the first is the influence of electrical hysteresis, and the second is the presence of a small internal field in the BP at zero bias, which has been observed in previous works on the infrared optical response of few-layer BP[253].

The second, higher energy feature observed in the measured spectrum does not correspond to any predicted intersubband transition. Rather, we propose it arises due to the allowing of an optical transition that was previously forbidden by quantum-well selection rule constraints dictated by symmetry (i.e., only transitions of equal quantum number are allowed under zero field[231]). We note that this feature is present in the 0 V extinction spectrum, consistent with a zero-bias internal field. As the symmetry is further broken with an externally-applied electric field, this transition is strengthened. Under positive bias, the internal and external fields are in competition, resulting in minimal change. This suppressed modulation can also be attributed to hysteresis, as before.

In Figure 6.2e, no modulation is measured for any applied bias for light polarized along the zigzag axis. This can be well understood due to the dependence of the Stark effect on the initial oscillator strength of an optical transition; because no intersubband optical transitions

are allowed along this axis, the field effect is weak. Similar behavior has been observed in excitons in ReS_2 based on an optical Stark effect[274]. Moreover, while the externally applied field can allow 'forbidden' transitions along the armchair axis by breaking the out-of-plane symmetry of the quantum well, in-plane symmetry properties and thus the selection rule precluding all zig-zag axis intersubband transitions are unaffected. This selection rule and the corresponding symmetry properties have been previously described [257].

In Figures 6.2f and 6.2g, we present the complementary data set of tunable dichroism measurements due to a directly applied gate bias with electrical contact made to the BP in a standard field-effect transistor (FET) geometry. Here, we observe modulation dominated by carrier concentration effects. At the band gap energy of approximately 0.53 eV, a simple decrease in absorptance is observed at negative and large positive biases, consistent with an ambipolar BM shift. Unlike the results of applying field while the BP floats, no modulation of the forbidden transition at 0.75 eV is observed; this is explained in part due to the screening of the electric field due to the carrier concentration modulation. We additionally may consider the possibility that this optical transition is disallowed by Pauli-blocking effects, negating the symmetry-breaking effect of the directly applied field. As in the case for the floating BP measurement, no modulation is observed along the zigzag axis.

6.3 Thickness-Dependent Tunability of Optical Response

The anisotropic electro-optical effects described above change character rapidly as the BP thickness – and hence band gap and band structure – is varied. Figure 6.3 presents analogous results on a flake of 8.5 nm thickness, determined by AFM, for which an optical image is presented in Fig. 6.3a. Due to the increased thickness, the energy separation between subbands is smaller, resulting in a narrower free-spectral range between absorptance features measured in the zero-bias spectrum, presented in Fig. 6.3b and for which corresponding calculated optical constants are presented in Fig. 6.3c. Results for modulation by an external field with the BP left floating are presented in Fig. 6.3d. As in the thin flake, substantial modulation of the absorptance at each intersubband transition is observed due to the QCSE red-shifting the energy of the subbands. Due to the large Stark

coefficient in BP – which increases with thickness in the few-layer limit – absorption is nearly 100% suppressed, resulting in an approximately isotropic optical response from the material[251, 275]. Unlike the previous sample, modulation of forbidden transitions is not apparent; all features correspond to transitions measured in the 0 V normalization scheme as well as the calculated optical constants for a thickness of 8.5 nm. As before, no modulation is seen along the zigzag axis. In Fig. 6.3e, the modulation for directly gated, contacted BP is shown. The observed modulation – a reduction in extinction centered at each of the calculated intersubband transition energies – is relatively weak and does not persist to high photon energies. This suggests that the dominant modulation mechanism is the ambipolar BM shift, rather than the QCSE.

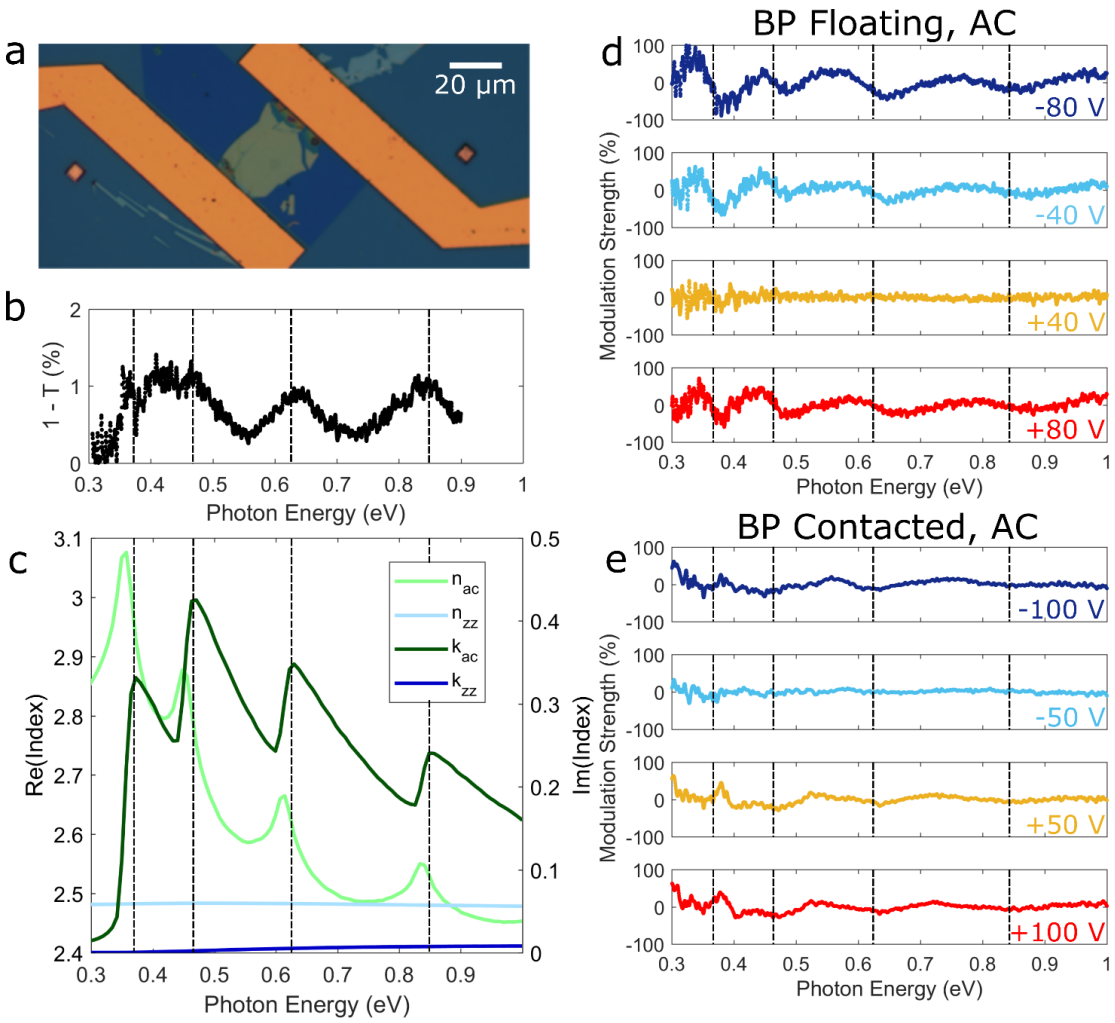

Figure 6.3: Variation of modulation with BP thickness. (a) Optical image of fabricated 8.5 nm sample. (b) Zero-bias extinction of 8.5 nm flake, polarized along AC axis. (c) Calculated index of refraction for 8.5 nm thick BP. (d) Modulation of BP oscillator strength with field applied to floating device, for light polarized along the AC axis. (e) Modulation of BP oscillator strength with gating of contacted device, for light polarized along the AC axis.

Additional data at lower energies is presented in Figure 6.4, more clearly illustrating the tuning of the band gap energy of this sample around 0.35 eV. This was done using a KBr beamsplitter instead of CaF_2 that was used for the rest of the measurements, allowing a better measurement at lower energies.

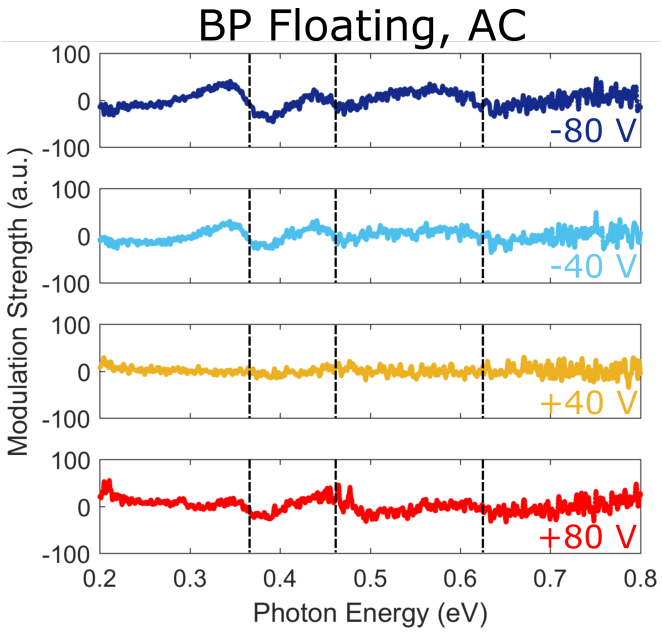

Figure 6.4: Lower photon energy spectra for the 8.5 nm flake. Modulation of BP oscillator strength with field applied to floating device, for light polarized along the AC axis, normalized to the maximum oscillator strength as previously.

6.4 Visible-Frequency Gate-Tunability

Finally, in Figure 6.5 we present results of gate-tunable dichroism at visible frequencies in a 20 nm thick flake, comparable to those considered for infrared modulation. A new device geometry is used to enable transmission of visible light, shown schematically in Fig. 6.5a and in an optical image in Fig. 6.5b. In this configuration, a $SrTiO_3$ substrate is utilized to allow transmission-mode measurements at visible wavelengths. A symmetric gating scheme is devised based on semi-transparent top and back gate electrodes of 5 nm Ni, as described in Appendix E. Only an applied field, floating BP measurement is utilized, as band-filling effects should be negligible at this energy range. In Fig. 6.5c, we present modulation results from 1.3 to 2 eV. Due to the QCSE, modulation is observed up to 1.8 eV, corresponding to red light. Thus we demonstrate that electro-optic modulation of linear dichroism is possible across an extraordinarily wide range of wavelengths in a single material system, enabling multifunctional photonic devices with broadband operation.

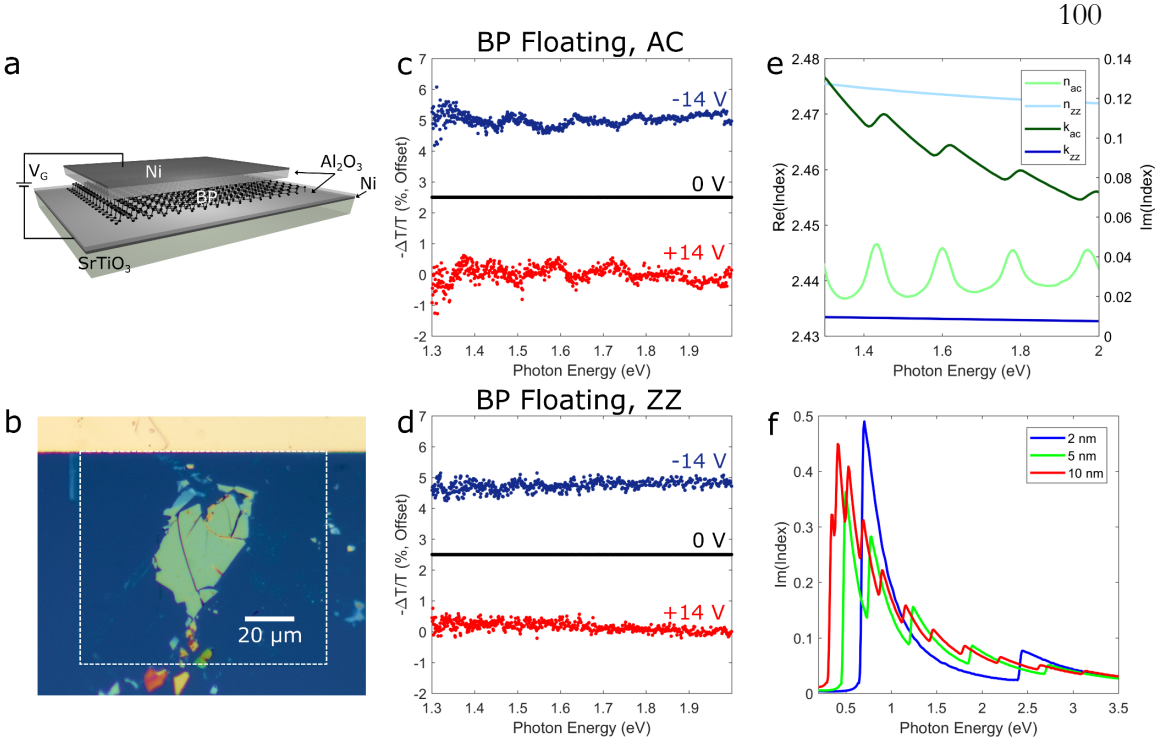

Figure 6.5: Modulation in the visible. (a) Schematic figure of visible modulation device. Few-layer BP is mechanically exfoliated on 45 nm Al_2O_3/5 nm Ni on $SrTiO_3$ and then coated with 45 nm Al_2O_3. A 5 nm thick semitransparent Ni top contact is used. (b) Optical image of fabricated sample with 20 nm thick BP. Dashed white line indicates the boundary of the top Ni contact. (c) Modulation of extinction with field applied to floating device, for light polarized along the AC axis. (d) Corresponding modulation for light polarized along the ZZ axis. (e) Calculated index of refraction for 20 nm thick BP for the measured energies. (f) Calculated imaginary index of refraction of several thicknesses of BP from the infrared to visible.

6.5 Conclusions and Outlook

The decay of BP intersubband oscillator strength at higher photon energies provides a spectral cutoff for QCSE-based modulation, but for 5 nm BP or thinner this oscillator strength is strong through the entire visible regime, as illustrated in Fig. 6.5f. We thus suggest that in very thin BP, strong modulation of absorption and dichroism is possible to even higher energies. By selecting a flake of 2 nm, for example, tunable linear dichroism is possible up to 3 eV from the band gap energy of 0.75 eV. A higher density of features, beginning at lower energies, may be introduced by utilizing a thicker flake, with slightly decreased modulation strength, as seen for 5 and 10 nm thickness flakes. We also note that

by substituting graphene top and bottom contacts or utilizing nanophotonic techniques to focus light in the BP, higher absolute modulation strength could be easily realized.

This phenomenon is in stark contrast to the gate-tunability of the optical response of other 2D materials, where substantial modulation is typically constrained to the narrowband energy of the primary exciton, as in MoS_2 and WS_2[242, 276]. In another van der Waals materials system, monolayer graphene, tunability is accessible over a broader wavelength range due to the Pauli-blocking of optical transitions at $2E_F$; however, this is limited to the range over which electrostatic gating is effective, typically between $E_F \sim 0$ to $E_F \sim 0.5$ eV[56, 277]. Moreover, these materials are not dichroic or birefringent in-plane, and so BP offers a novel phenomenon that can be taken advantage of to realize previously challenging or impossible photonic devices. The same restriction is true of bulk tunable materials such as quantum wells, transparent conducting oxides, and transition metal nitrides.

In summary, we have demonstrated broadly tunable linear dichroism in few-layer black phosphorus. We can explain this modulation as arising from a combination of quantum-confined Stark effects, ambipolar Burstein-Moss effects, and the allowing of forbidden optical transitions by the symmetry-breaking effects of the applied electric field. We identify the different physical mechanisms governing this tunability by comparing the modulation response from a dual gate wherein the BP is left floating to a single gate directly applied to the BP, leading to modulation of carrier concentration. By varying the thickness, and therefore band structure of the BP, we see that it is possible to control the spectroscopic modulation as well as the dominant physical mechanisms of modulation. We suggest that this phenomenon is a promising platform for controlling the in-plane propagation of surface or waveguide modes, as well as for polarization-switching, reconfigurable far-field metasurfaces. These applications are particularly promising in light of our observation that BP absorption can be modulated from anisotropic to nearly isotropic in-plane. Because van der Waals materials can be easily integrated into photonic devices, this promises to introduce new functionalities that cannot be realized by conventional electro-optic materials.

C h a p t e r 7

PERSPECTIVE AND FUTURE WORKS

"No man should escape our universities without knowing how little he knows."
– J. Robert Oppenheimer

In this thesis, we have commented on two van der Waals materials, graphene and few-layer black phosphorus, as promising materials for active nanophotonic devices in the mid-infrared. We have made progress to create a complete 'tool-kit' for controlling all aspects of infrared light in absorption, reflection, and emission using graphene nanostructures. We have additionally introduced few-layer black phosphorus as a promising new material for actively tunable nanophotonic structures from the visible to mid-infrared based on its natural quantum well electronic band structure. We also explored the in-plane optical anisotropy of BP, which yields a tunable linear dichroism, the first material to show such a feature to the best of our knowledge. In this chapter, we extend these concepts and present some future directions for research on van der Waals materials for nanophotonics. We additionally make a brief comment on the long-term viability of both materials in commercial technology. Finally, we note that these nanophotonic approaches are applicable to other van der Waals systems, including semiconducting transition metal dichalcogenides (TMDCs), and present a method for enhancing absorption in monolayer WS_2.

7.1 Graphene Research

Fundamental research on graphene at the lab scale has largely moved beyond the basic physics problems into more applied topics, as well as the development of heterostructures that take advantage of graphene's unique properties in combination with other van der Waals materials (semiconducting, superconducting, and insulating). This is allowing for an in-depth study of van der Waals/low-dimensional quasiparticles, their coupling, and their response to an external bias[278]. Moreover, graphene can be easily incorporated as a semi-transparent electrical contact in many devices based on other van der Waals materials,

which may be useful for integrated optoelectronic devices (e.g. LEDs and photovoltaics may benefit from such a device geometry)[279]. As new methods for growing large-scale 2D materials, such as metal-organic chemical vapor deposition for transition metal dichalcogenides, mature, there will be new opportunities for commercialization of devices based on such heterostructures[280, 281]. So, as the research on other van der Waals materials matures, new opportunities for graphene may emerge.

In addition, the tunable optical properties of graphene in the mid-infrared discussed in this thesis may lend it to applications in a number of spaces. Because graphene can be utilized to control amplitude, phase, and polarization in the infrared, it may enable new functions for tunable sensors (biological or chemical because of the well-defined infrared signatures of molecular species) and thermal radiation control in the near- and far-field. It is also possible that these topics may be merged, enabling multifunctional devices in the infrared. Comments on another exciting potential application for phase control, LIDAR, were made in Chapter 4.

7.1.1 Control of Far-Field Thermal Radiation

In this thesis, we discussed the control of the amplitude and polarization of thermal radiation in the far-field. We additionally demonstrated active modulation of reflected phase using graphene-gold nanoantennas. It would be of great interest to consider the combination of such projects, enabling active control of the phase of emitted thermal radiation. Based on the reciprocity between absorptivity and emissivity, it stands to reason that the phase relation between two different resonant elements would be preserved when the exciting field is thermal oscillations (such as from the substrate on which they are fabricated) instead of an incident light source (typically required to be a laser). If we could then engineer the phase profile at a surface into a metasurface using these tunable resonant elements, we could create a self-contained tunable metasurface device that provides both the light source and the optical functionality (e.g., focusing, steering, etc). For this to be realized, we require spatial coherence to be preserved, such that the phase fronts from each position can interfere in the far-field. Works from J. J. Greffet et al. have shown that

coherence can be preserved in thermally excited surface phonon polaritons over long distances, up to 10s of μms in polar dielectrics.[282] So, by taking advantage of this, we could realize a proper emission-type reconfigurable metasurface.

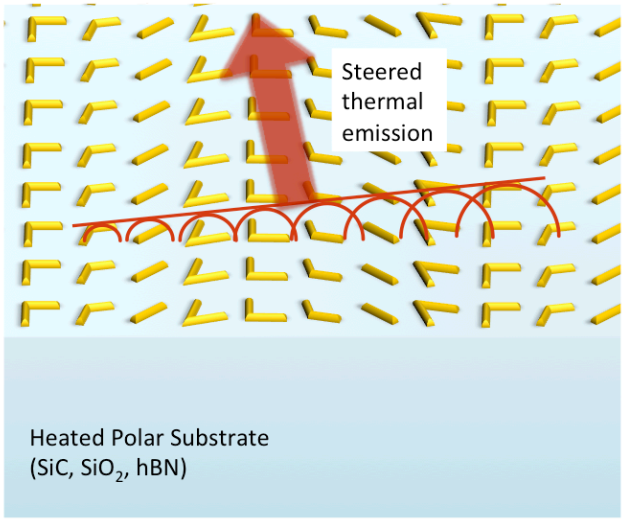

Figure 7.1: A conceptual representation of the steering of thermal radiation using a metasurface with a linear phase gradient on a heated polar substrate for steering of radiation. Active control could be incorporated by using graphene as a tunable dielectric environment.

7.1.2 Control of Near-Field Heat Transfer

Near-field heat transfer has become an exciting research topic over the past decade as it allows us to exceed the Stefan-Boltzmann law that restricts the power density of thermal radiation in proportion to T^4 in the far field. As we move into the near-field, where we are operating at length scales comparable to the wavelength of the emitted light, the coupling of surface modes between objects leads to radiative heat transfer that significantly exceeds the Stefan-Boltzmann law[283]. This has interesting implications for new types of energy-harvesting devices such as thermo-photovoltaics that operate based on thermal emission, or using radiative heat transfer for refrigeration.

A remaining challenge in this field is how to actively control near-field heat transfer (NFHT) with rapid switching speeds, typically not accessible with the slow time scales needed for heating and cooling bulk objects. By using the electrically tunable plasmons and coupled plasmon-phonon polaritons supported by graphene on a polar substrate, it should

be possible to control the near-field heat transfer between two graphene sheets with rapid switching speeds. This operates based on the principle that when the spectral overlap between surface waves is large, near-field heat transfer is efficient, and when there is no overlap, the NFHT is suppressed, schematically shown in Figure 7.2. So, by electrically tuning the graphene plasmon resonance using an external gate, the degree of spectral overlap can be controlled, and therefore the NFHT can be modulated at speeds characteristic of carrier relaxation times in graphene.

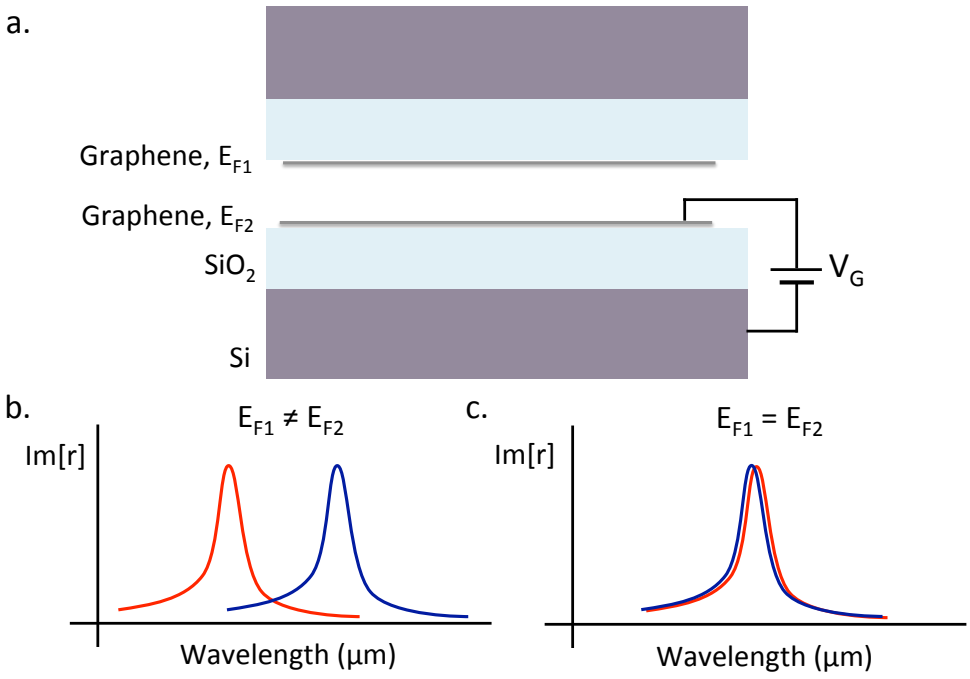

Figure 7.2: (a) Schematic of experimentally realistic structure for tunable near-field heat transfer. (b) Spectral absorption coefficients for unequal Fermi energies on the top and bottom sheets, minimizing heat transfer. (c) Spectral absorption coefficients for equal Fermi energies, maximizing NFHT. Electrostatic gating can be used to tune the Fermi energies to be matched/unmatched.

There have been a number of theoretical works on this topic[284, 285]; however, the experimental realization of such a structure has remained elusive, in part because many of the theoretical works neglect important features such as substrate contributions and the

challenges associated with placing two objects in very close proximity (~100s of nm). Along with collaborators Nate Thomas and Prof. Austin Minnich, we suggest that by using a straightforward planar geometry of two graphene sheets on SiO_2/Si substrates, this experiment could be done.

7.1.3 Graphene-Based Sensors

Because graphene plasmons are active in the mid-infrared, their coupling to molecular vibrations can produce a very strong optical signal. This was shown in a recent publication from D. Rodrigo et al., where the plasmon resonance of graphene nanoribbons was modified by the presence of different molecular species and the active tunability of the plasmon gave an additional degree of sensitivity[286]. Moreover, because of the strong field enhancement in the near-field of the graphene resonators, it is suggested that very small concentrations of molecules may be detected. One application space where this might be interesting is in tracking the time evolution of different chemical reactions. Because the response time of graphene carriers is very fast, its time-dependent optical response could give new insights into the different molecules present throughout the course of a chemical reaction, such as the important and complex process of CO_2 reduction, of interest in the Department of Energy Joint Center for Artificial Photosynthesis. By better understanding the different species that are evolved over time, more efficient photocatalysts could be developed that target the specific intermediate steps observed. Such experiments would necessitate ultrafast detection schemes, but would be consistent with time scales achievable for graphene charge carriers.

7.1.4 Graphene Devices in the High-Carrier Concentration Limit

For many years, a major goal of the graphene community has been the realization of tunable plasmon devices in the technologically important telecommunications band (1550 nm), or higher energies. There exist two major barriers to realizing this: this first being the achievement of sufficiently high carrier concentrations, and the second being the fabrication of nanoresonators of sufficiently small dimensions, as the plasmon frequency of

graphene (as noted previously) has a dependence as $\omega_p \propto n^{1/4}$, $\omega_p \propto \frac{1}{W^{1/2}}$. Therefore, in order to measure plasmons in the near-infrared, nanoresonators widths down to ~5 nm are needed, as well as carrier concentrations on the order of 10^{14} cm^{-2}.

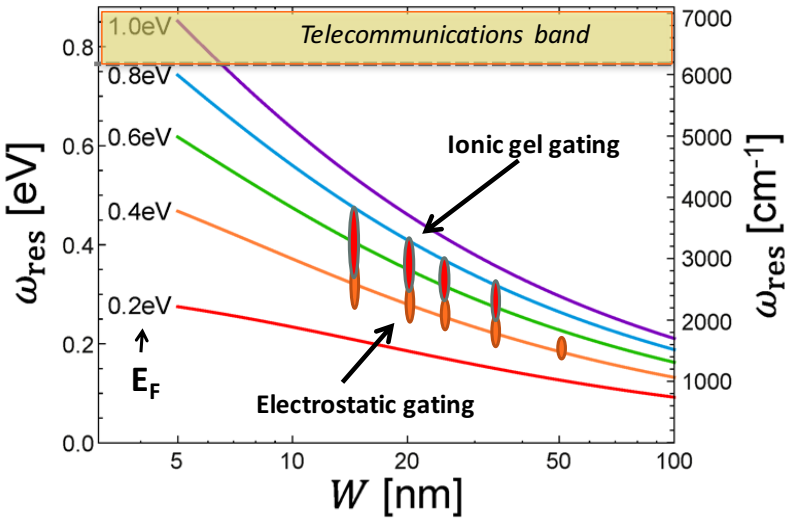

Figure 7.3: A map of the thickness and carrier concentration dependence of the plasmon resonance of graphene, illustrating the importance of small resonators and high carrier concentration to reach high energies.

To date, using electron beam nanolithography, we have been able to obtain plasmon resonance spectra from graphene nanoribbons as small as 15 nm. These nanoresonators have displayed resonant frequencies across the mid-IR, to wavelengths as short as 4 μm, and, notably, above the graphene optical phonon energy at 200 meV.

To address this challenge, we suggest the possibility of extending the range of these graphene nanoresonators by patterning them to the 3-5 nm length scale in order to achieve near-infrared resonances, and to explore Fermi level modulation gating techniques that will allow for higher charge densities and thus access to a larger plasmon frequency range.

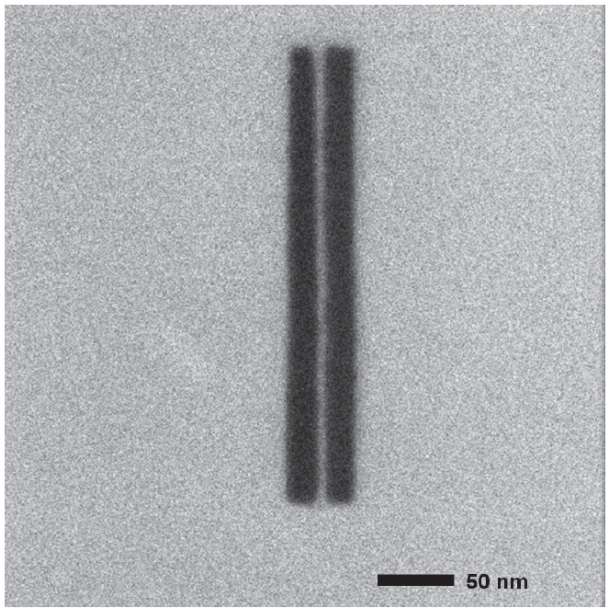

Figure 7.4: Suspended graphene nanoresonator of 5 nm width and an aspect ratio of 60:1 fabricated by He ion FIB. From Zeiss white paper., ref [289]

We will employ the use of ionic liquids as well as high static permittivity and ferroelectric substrates (e.g., $SrTiO_3$ and $BaTiO_3$) in order to achieve these goals. In particular, we will explore the use of materials with extremely high DC permittivities for gate dielectrics. A recent report demonstrated that only 15 V is needed across a 500 μm thick gate dielectric of single-crystal $SrTiO_3$ to dope graphene from its charge neutral point (CNP) to a carrier density of $4x10^{12}$ cm^{-2} at low temperatures, due to the divergent dielectric constant of $SrTiO_3$ (~20,000 at a temperature of 4K).[287] Higher carrier concentrations have not yet been achieved due to the charged surface states of the $SrTiO_3$ pinning the Fermi energy of the graphene.[288] We suggest that by employing a geometry consisting of graphene nanoresonators on 100 μm thick $SrTiO_3$ substrates passivated by 10 nm Al_2O_3 films deposited by atomic layer deposition, carrier concentrations of close to 10^{15} cm^{-2} could be reached, an order of magnitude larger than has been achieved to date in solid-state systems. In addition, we will take advantage of the ultra-high resolution patterning of monolayer materials enabled by He^+ ion focused ion beam lithography (Zeiss Orion FIB). By using the shorter de Broglie wavelength of high energy 30 keV He^+ ions it is possible to directly pattern resonators into monolayer materials which weakly back-scatter the incident ions.

Use of the Zeiss Orion FIB instrument for fabrication of graphene nanoribbons with 5 nm feature sizes has been demonstrated, as seen in Fig. 15.[289]

7.2 Graphene-Integrated Devices (Commercialization)

While the excitement surrounding graphene has dimmed since its initial discovery in 2004, it now has reached a level of maturity where we can assess the real opportunities for incorporating it into devices, and its longer-term potential. The Graphene Flagship project in Europe has set ambitious goals to commercialize graphene-based products, such as photodetectors and biosensors, investing €1 billion to bring lab-scale research to market. So far, no major company has emerged that is competing with the state of the art; however, it appears possible that niche markets will emerge in which graphene's high conductivity and mechanical flexibility could make it the superior material for devices, and a number of start-up companies have launched. This is particularly interesting for wearable technologies and implantable devices. As growth and roll-to-roll transfer processes become more sophisticated and less expensive, it is possible that graphene will eventually live up to its hype. If we consider graphene in the context of the 'Gartner Hype Cycle', Figure 7.5 below, it looks like the field has survived the 'trough of disillusionment' that came not long after the Nobel Prize in Physics was awarded in 2010 for its discovery, and may move into a comfortable 'plateau of productivity'. By throwing out our expectations that graphene would revolutionize all realms of technology, there may be real opportunities for it to make an impact, though none have yet come to fruition.

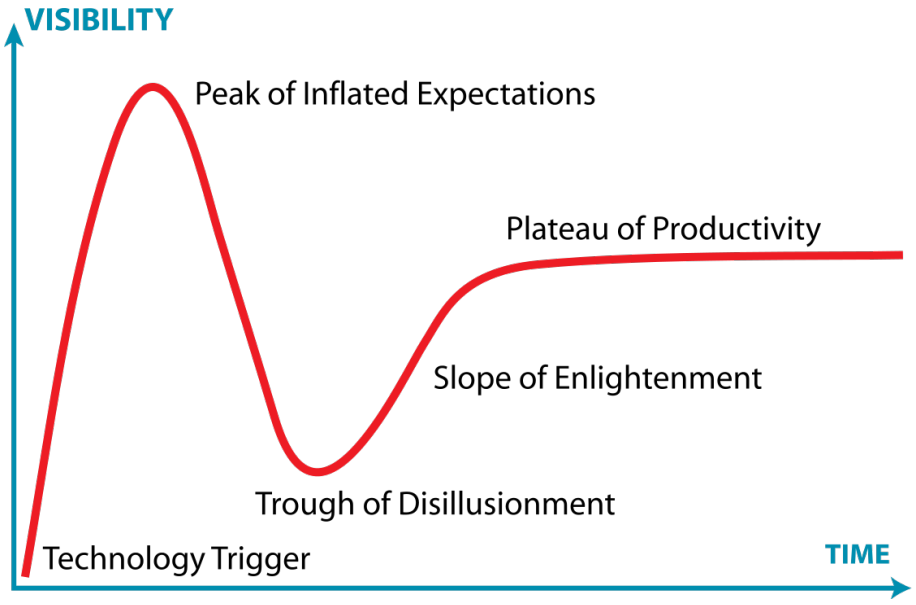

Figure 7.5: Gartner Hype Cycle. A visualization of the phases of maturity of new technologies, useful (if not scientifically validated) for understanding the life cycle of graphene to date. Adapted from [290]

7.3 Black Phosphorus Research and Development

Unlike graphene, black phosphorus is in a much earlier stage of research, and indeed its most fundamental optical properties are still not fully characterized. While our works have attempted to answer some of these questions, one of the major limitations is the absence of large-area samples needed for measurements like infrared ellipsometry to determine the complex index of refraction. Efforts in a number of labs are ongoing to grow large-scale BP; however, these are often nanocrystalline in nature, and therefore the electronic quality is low, and the in-plane anisotropy – one of black phosphorus' most desirable properties – is lost. The primary challenge here is that black phosphorus is the high-temperature and high-pressure phase of phosphorus, and therefore its growth relies on extremely high temperatures and pressures, introducing safety hazards and preventing economical growth conditions from being realized. It is possible that there will be major breakthroughs in growth in the future; however, until this time, BP will remain an exciting material at the lab scale only. Optimistically, one might imagine that if a unique application for BP is realized, there will be sufficient motivation in the academic community to develop exotic new

growth schemes for large are black phosphorus films. Below, we comment on a few interesting nanophotonic structures using black phosphorus.

7.3.1 Black Phosphorus for In-Plane Beam Steering

One of the most interesting properties of black phosphorus is that it is optically inactive along one axis (absorption pathways are forbidden), and, by using an external gate, its oscillator strength along the other axis can be completely suppressed at a given energy corresponding to one of its intersubband transitions. This means that BP can effectively be tuned from optically anisotropic to isotropic in plane. One consequence of this is it may enable in-plane beam steering by changing the local dielectric environment of a plasmonic material such as gold or silver. By changing the degree of anisotropy of the BP, the propagation of a surface plasmon polariton could be redirected, as shown schematically in Figure 7.6, below.

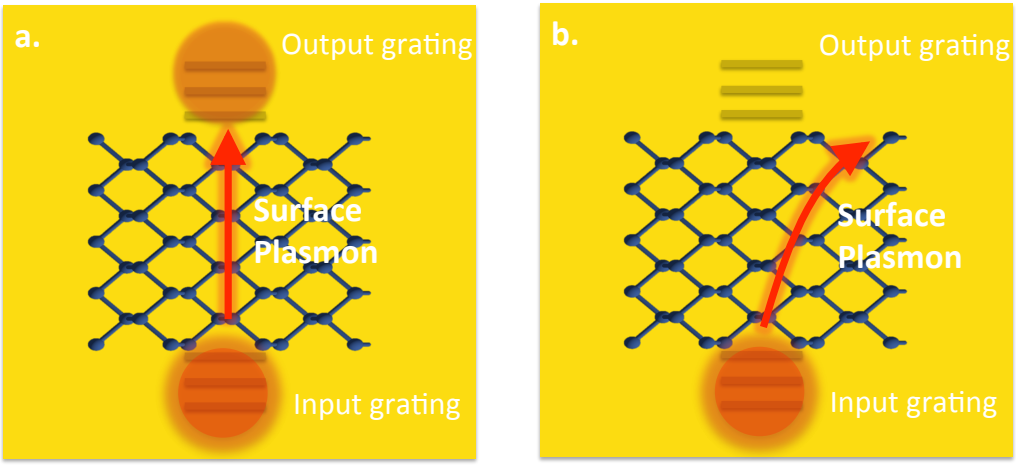

Figure 7.6: A schematic proposal of using black phosphorus as an active dielectric material for steering of surface plasmons. (a) When BP is optically isotropic, the surface plasmon propagates in a straight line from input to output gratings. (b) When the optical anisotropy of the BP is increased, the surface plasmon is redirected. In this case, we simply use this as a switch; multiple gratings or multiple branches of a slot waveguide mode could be used to route light.

In its simplest configuration, this could be utilized as a switch, redirecting light away from the output grating on a plasmonic surface. However, by carefully designing different

branches of a waveguide structure (e.g. silicon slab or slot waveguides), it is possible that the preferential propagation through each branch could be achieved. By taking advantage of the anisotropy of BP, we may open up an interesting new design space for integrated photonics. To date, BP has never been experimentally integrated into a nanophotonic structure/device; we suggest that this is a promising avenue to explore.

7.3.2 Black Phosphorus for Far-Field Polarization Control

One of the simplest ways to take advantage of the anisotropic optical response of BP is by integrating it into an external cavity for efficiently switching the absorbed polarization state of light. On its own, black phosphorus only interacts with a small fraction of light due to its deep subwavelength thickness; photonic design is required to realize highly efficient modulators. An isotropic resonant structure could be used, taking advantage of the BP to introduce varying degrees of anisotropy. The simplest way to approach this would be to incorporate BP into a ‘perfect absorber’ or gap mode based on a square array of gold disks aligned with the two axes of the BP, schematically presented in Figure 7.7. In this way, the polarization component of light absorbed depends on the differential absorption between the two axes of the BP, enhanced by the resonant design. This is a very straightforward design; more complex designs that include phase and polarization control could likely be realized through careful design and optimization.

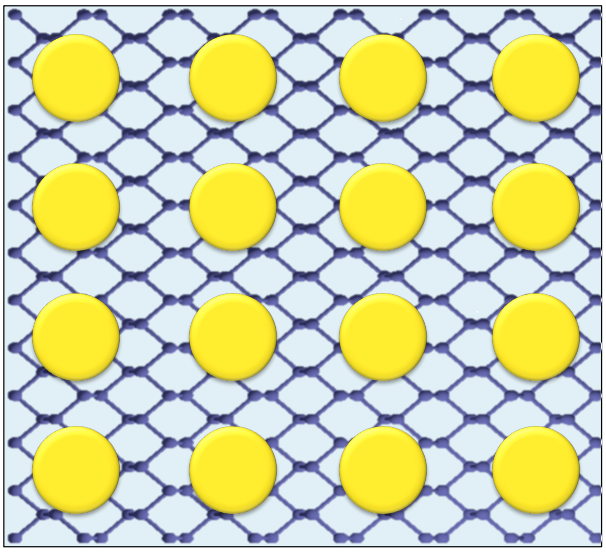

Figure 7.7: A schematic representation (top-down) of a nanophotonic structure that could be used for actively controlling the polarization of absorbed (or thermally emitted) light using the tunable linear dichroism of BP.

7.4 Nanophotonics and other van der Waals Materials

In addition to black phosphorus and graphene, other van der Waals materials are of great interest in nanophotonic designs, highlighted in a recent review from F. Xia et al.[197] In this chapter we briefly describe designs for enhancing the absorption in a monolayer van der Waals semiconductor in the visible. Other works from our group have tackled the problem of absorption in few-layer TMDCs[279, 291]; however, to maintain the high external quantum efficiency in these materials, devices that operate with monolayer samples (which are direct band gap materials, whereas in the few layer limit, TMDCs are indirect band gap semiconductors) are desirable.

We take advantage of a dual-resonant cavity based on high index TiO_2 resonators fabricated on monolayer TMDCs. The second resonance is introduced by a Ag back-reflector separated by 20 nm from the TMDC, as shown in Figure 7.8 below.

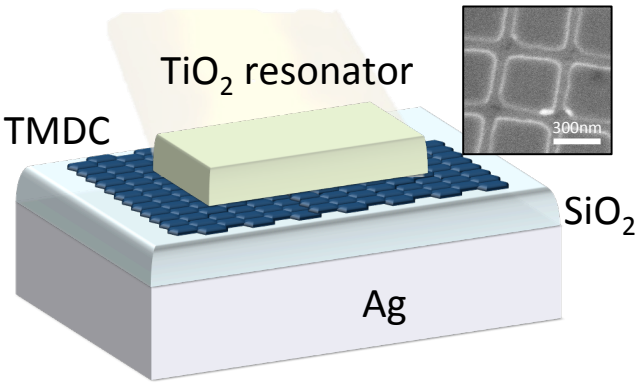

Figure 7.8: Schematic of resonant geometry designed for enhancing absorption in monolayer TMDCs. Insert in upper right is a SEM image of fabricated TiO_2 resonators.

By using different TMDCs, and varying the dimension of the TiO2 dielectric resonators, it is possible to target narrow- or broad-band absorption (and therefore luminescence) enhancement, depending on the goal. For designing a highly efficient emitter, we use monolayer WS_2 as our TMDC, and a resonator width of 350 nm, spaced by 100 nm. Because of the low losses of the TiO_2, almost all the enhancement of absorption is into the WS_2, shown in Figure 7.9 below.

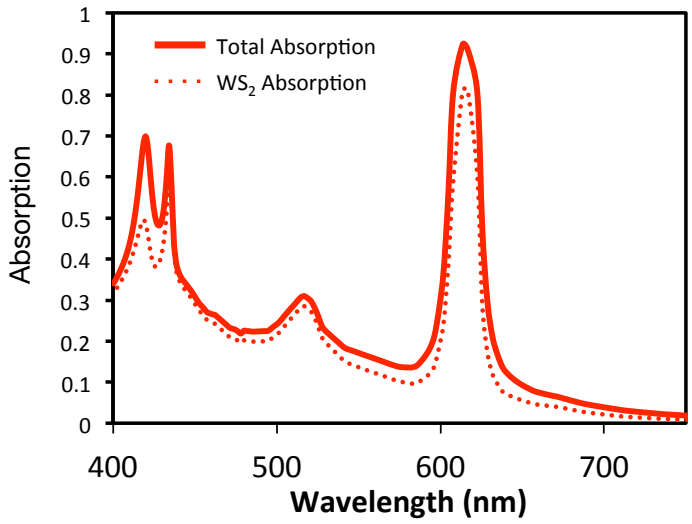

Figure 7.9: Simulated absorption of TiO_2/WS_2 resonant structure. 85% of absorption is into the monolayer WS_2 at its exciton peak of 625 nm.

This geometry is of interest in particular because it is known that the excitonic emission of TMDCs can be controlled with an external gate voltage[292], enabling an electrically switched emitter.

In considering designs for a photovoltaic device, broadband absorption into a monolayer TMDC is desirable. In this case, we take advantage of the variation in peak absorption in the TiO_2 resonators with resonator width combined with WSe_2, which absorbs light strongly across the visible, unlike WS_2 with a narrow exciton absorption line. By sweeping the width of the resonators from 135 to 295 nm, WSe_2 absorption can be enhanced across the visible. We can then imagine designing a trapezoid structure based on this range of widths in order to enhance the absorption across that entire range, analogous to the broadband perfect absorber developed by K. Aydin et al using silver trapezoid absorbers.[186] The simulated WSe_2 absorption is presented in Figure 7.10, below.

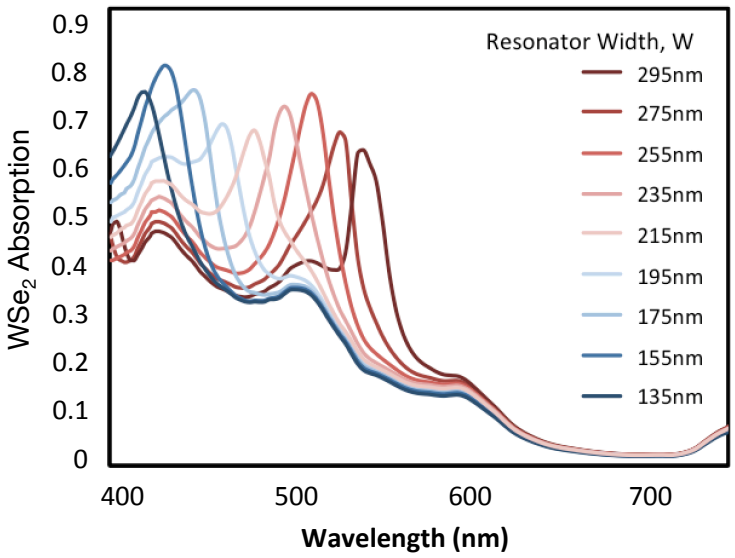

Figure 7.10: Simulated absorption in WSe2 using TiO_2 resonators on an Ag back reflector, with varying width of the TiO_2 and a fixed separation between resonators of 100 nm.

There are many exciting opportunities for incorporating TMDCs into photovoltaic devices, particularly because of their very high luminescence quantum yield in monolayer form[293],

and band gap energies that would make them an excellent tandem partner to silicon based on the Shockley Quissier limit. The further exploration of nanophotonic designs to optimize these devices may be a research topic of great interest in the future.

7.5 Endless Opportunities

As more 2D materials are discovered and explored, the opportunities to combine them with different nanophotonic designs will expand greatly. Even now, with the recent discovery of monolayer magnetic materials and the excitement surrounding layered topological insulators, we can imagine exotic new physics will emerge that we can exploit for new photonic functions. The challenges of large-scale integration remain; however great progress is being made in this field, and roll-to-roll manufacturing of some of these materials is not out of reach. Van der Waals materials give us an amazing set of properties that we can combine together at will, and by incorporating them with nanophotonics, the possibilities for new devices and emergent physics are immense.

BIBLIOGRAPHY

1. Maier, S. A.; Brongersma, M. L.; Kik, P. G.; Meltzer, S.; Requicha, A. A. G.; Atwater, H. A. *Advanced Materials* **2001,** 13, (19), 1501-+.
2. Maier, S. A.; Kik, P. G.; Atwater, H. A.; Meltzer, S.; Harel, E.; Koel, B. E.; Requicha, A. A. G. *Nature Materials* **2003,** 2, (4), 229-232.
3. Yokogawa, S.; Burgos, S. P.; Atwater, H. A. *Nano Letters* **2012,** 12, (8), 4349-4354.
4. Arbabi, A.; Horie, Y.; Bagheri, M.; Faraon, A. *Nature Nanotechnology* **2015,** 10, (11), 937-U190.
5. Khorasaninejad, M.; Chen, W. T.; Devlin, R. C.; Oh, J.; Zhu, A. Y.; Capasso, F. *Science* **2016,** 352, (6290), 1190-1194.
6. Willets, K. A.; Van Duyne, R. P. *Annu Rev Phys Chem* **2007,** 58, 267-297.
7. Homola, J.; Yee, S. S.; Gauglitz, G. *Sensor Actuat B-Chem* **1999,** 54, (1-2), 3-15.
8. Hsiao, H. H.; Chu, C. H.; Tsai, D. P. *Small Methods* **2017,** 1, (4).
9. Hungate, W., *Hyperspectral Remote Sensing: Principles and Applications*. Taylor and Francis: 2008.
10. Maier, S., *Plasmonics: Fundamentals and Applications*. Springer: 2007.
11. Yu, N. F.; Genevet, P.; Kats, M. A.; Aieta, F.; Tetienne, J. P.; Capasso, F.; Gaburro, Z. *Science* **2011,** 334, (6054), 333-337.
12. Ni, X.; Emani, N. K.; Kildishev, A. V.; Boltasseva, A.; Shalaev, V. M. *Science* **2012,** 335, (6067), 427.
13. Yu, N.; Aieta, F.; Genevet, P.; Kats, M. A.; Gaburro, Z.; Capasso, F. *Nano Lett* **2012,** 12, (12), 6328-33.
14. Wood, J. D.; Wells, S. A.; Jariwala, D.; Chen, K.-S.; Cho, E.; Sangwan, V. K.; Liu, X.; Lauhon, L. J.; Marks, T. J.; Hersam, M. C. *Nano Letters* **2014,** 14, (12), 6964-6970.
15. Ni, X.; Kildishev, A. V.; Shalaev, V. M. *Nature Communications* **2013,** 4, 2807.
16. Ni, X.; Wong, Z. J.; Mrejen, M.; Wang, Y.; Zhang, X. *Science* **2015,** 349, (6254), 1310-4.
17. Minovich, A. E.; Miroshnichenko, A. E.; Bykov, A. Y.; Murzina, T. V.; Neshev, D. N.; Kivshar, Y. S. *Laser Photonics Rev* **2015,** 9, (2), 195-213.
18. Genevet, P.; Capasso, F. *Rep Prog Phys* **2015,** 78, (2).
19. Zhao, Y.; Liu, X. X.; Alu, A. *J Optics-Uk* **2014,** 16, (12).
20. Chen, H. T.; Taylor, A. J.; Yu, N. F. *Rep Prog Phys* **2016,** 79, (7).
21. Augustine, M. U.; Zubin, J.; Luca Dal, N.; Nader, E.; Boardman, A. D.; Egan, P.; Alexander, B. K.; Vinod, M.; Marcello, F.; Nathaniel, K.; Clayton, D.; Jongbum, K.; Vladimir, S.; Alexandra, B.; Jason, V.; Carl, P.; Anthony, G.; Evgenii, N.; Linxiao, Z.; Shanhui, F.; Andrea, A.; Ekaterina, P.; Natalia, M. L.; Mikhail, A. N.; Kevin, F. M.; Eric, P.; Xiaoying, L.; Paul, F. N.; Cherie, R. K.;

Christopher, B. M.; Dorota, A. P.; Igor, I. S.; Vera, N. S.; Debashis, C. *J Optics-Uk* **2016,** 18, (9), 093005.
22. Meinzer, N.; Barnes, W. L.; Hooper, I. R. *Nature Photonics* **2014,** 8, (12), 889-898.
23. Yu, N. F.; Capasso, F. *Nature Materials* **2014,** 13, (2), 139-150.
24. Patrice Genevet, F. C., Francesco Aieta, Mohammadreza Khorasaninejad, and Robert Devlin. *Optica* **2017,** 4, (1), 139-152.
25. Geim, A. K.; Novoselov, K. S. *Nature Materials* **2007,** 6, (3), 183-191.
26. Novoselov, K. S.; Geim, A. K.; Morozov, S. V.; Jiang, D.; Zhang, Y.; Dubonos, S. V.; Grigorieva, I. V.; Firsov, A. A. *Science* **2004,** 306, (5696), 666-669.
27. Castro Neto, A. H.; Guinea, F.; Peres, N. M. R.; Novoselov, K. S.; Geim, A. K. *Rev Mod Phys* **2009,** 81, (1), 109-162.
28. Novoselov, K. S.; Fal'ko, V. I.; Colombo, L.; Gellert, P. R.; Schwab, M. G.; Kim, K. *Nature* **2012,** 490, (7419), 192-200.
29. Allen, M. J.; Tung, V. C.; Kaner, R. B. *Chem Rev* **2010,** 110, (1), 132-145.
30. Jablan, M.; Buljan, H.; Soljacic, M. *Physical Review B* **2009,** 80, (24).
31. Falkovsky, L. A. *J Phys Conf Ser* **2008,** 129.
32. Falkovsky, L. A.; Pershoguba, S. S. *Physical Review B* **2007,** 76, (15).
33. Li, L. K.; Yu, Y. J.; Ye, G. J.; Ge, Q. Q.; Ou, X. D.; Wu, H.; Feng, D. L.; Chen, X. H.; Zhang, Y. B. *Nature Nanotechnology* **2014,** 9, (5), 372-377.
34. Ling, X.; Wang, H.; Huang, S.; Xia, F.; Dresselhaus, M. S. *Proceedings of the National Academy of Sciences* **2015,** 112, (15), 4523-4530.
35. Miller, D. A. B.; Chemla, D. S.; Damen, T. C.; Gossard, A. C.; Wiegmann, W.; Wood, T. H.; Burrus, C. A. *Physical Review Letters* **1984,** 53, (22), 2173-2176.
36. Raether, H., *Surface plasmons on smooth and rough surfaces and on gratings*. Springer: Berlin, 1988.
37. Polman, A. *Science* **2008,** 322, (5903), 868-869.
38. Chang, D. E.; Sørensen, A. S.; Hemmer, P. R.; Lukin, M. D. *Phys Rev Lett* **2006,** 97, (5), 053002.
39. Nagpal, P.; Lindquist, N. C.; Oh, S.-H.; Norris, D. J. *Science* **2009,** 325, (5940), 594-597.
40. Tassin, P.; Koschny, T.; Kafesaki, M.; Soukoulis, C. M. *Nat Photonics* **2012,** 6, (4), 259-264.
41. Boltasseva, A.; Atwater, H. A. *Science* **2011,** 331, (6015), 290-291.
42. Sarid, D. *Phys Rev Lett* **1981,** 47, 1927-1930.
43. Miyazaki, H. T.; Kurokawa, Y. *Phys Rev Lett* **2006,** 96, (9).
44. Jones, W. E.; Kliewer, K. L.; Fuchs, R. *Physical Review* **1969,** 178, (3), 1201-1203.
45. Economou, E. N. *Physical Review* **1969,** 182, 539-554.
46. Dionne, J. A.; Sweatlock, L. A.; Atwater, H. A.; Polman, A. *Phys Rev B* **2005,** 72, (7), 075405.
47. Burke, J. J.; Stegeman, G. I.; Tamir, T. *Phys Rev B* **1986,** 33, (8), 5186-5201.
48. Berini, P. *Opt Lett* **1999,** 24, (15), 1011-1013.

49. Koppens, F. H. L.; Chang, D. E.; García de Abajo, F. J. *Nano Letters* **2011,** 11, (8), 3370-3377.
50. Jablan, M.; Buljan, H.; Soljačić, M. *Phys. Rev. B* **2009,** 80, (24), 245435.
51. Hwang, E. H.; Das Sarma, S. *Phys. Rev. B* **2007,** 75, (20), 205481.
52. Polini, M.; Tomadin, A.; Asgari, R.; MacDonald, A. H. *Phys. Rev. B* **2008,** 78, (11), 115426.
53. Yan, H.; Li, Z.; Li, X.; Zhu, W.; Avouris, P.; Xia, F. *Nano Letters* **2012,** 12, (7), 3766-3771.
54. Yan, H.; Li, X.; Chandra, B.; Tulevski, G.; Wu, Y.; Freitag, M.; Zhu, W.; Avouris, P.; Xia, F. *Nature Nanotechnology* **2012,** 7, (5), 330-334.
55. Ju, L.; Geng, B.; Horng, J.; Girit, C.; Martin, M.; Hao, Z.; Bechtel, H. A.; Liang, X.; Zettl, A.; Shen, Y. R.; Wang, F. *Nature Nanotechnology* **2011,** 6, (10), 630-634.
56. Fei, Z.; Rodin, A. S.; Andreev, G. O.; Bao, W.; McLeod, A. S.; Wagner, M.; Zhang, L. M.; Zhao, Z.; Thiemens, M.; Dominguez, G.; Fogler, M. M.; Neto, A. H. C.; Lau, C. N.; Keilmann, F.; Basov, D. N. *Nature* **2012,** 487, (7405), 82 - 85.
57. Chen, J.; Badioli, M.; Alonso-González, P.; Thongrattanasiri, S.; Huth, F.; Osmond, J.; Spasenović, M.; Centeno, A.; Pesquera, A.; Godignon, P.; Zurutuza Elorza, A.; Camara, N.; de Abajo, F. J. G.; Hillenbrand, R.; Koppens, F. H. L. *Nature* **2012,** 487, (7405), 77-81.
58. Fang, Z.; Thongrattanasiri, S.; Schlather, A.; Liu, Z.; Ma, L.; Wang, Y.; Ajayan, P. M.; Nordlander, P.; Halas, N. J.; García de Abajo, F. J. *Acs Nano* **2013,** 7, (3), 2388-2395.
59. Wendler, L.; Haupt, R. *Journal of Physics C: Solid State Physics* **1986,** 19, (11), 1871.
60. Arakelian, V. H.; Hovsepian, N. M. **1991,** 164, (1), 155.
61. Li, X.; Magnuson, C. W.; Venugopal, A.; An, J.; Suk, J. W.; Han, B.; Borysiak, M.; Cai, W.; Velamakanni, A.; Zhu, Y.; Fu, L.; Vogel, E. M.; Voelkl, E.; Colombo, L.; Ruoff, R. S. *Nano Letters* **2010,** 10, (11), 4328-4334.
62. Li, X.; Cai, W.; An, J.; Kim, S.; Nah, J.; Yang, D.; Piner, R.; Velamakanni, A.; Jung, I.; Tutuc, E.; Banerjee, S. K.; Colombo, L.; Ruoff, R. S. *Science* **2009,** 324, (5932), 1312-1314.
63. Novoselov, K. S.; Geim, A. K.; Morozov, S. V.; Jiang, D.; Katsnelson, M. I.; Grigorieva, I. V.; Dubonos, S. V.; Firsov, A. A. *Nature* **2005,** 438, (7065), 197-200.
64. Christensen, J.; Manjavacas, A.; Thongrattanasiri, S.; Koppens, F. H. L.; García de Abajo, F. J. *Acs Nano* **2012,** 6, (1), 431-440.
65. Falkovsky, L. A.; Varlamov, A. A. **2007,** - 56, (- 4), - 284.
66. Palik, E. D., *Handbook of Optical Constants of Solids*. Academic Press: 1998.
67. Fei, Z.; Andreev, G. O.; Bao, W. Z.; Zhang, L. F. M.; McLeod, A. S.; Wang, C.; Stewart, M. K.; Zhao, Z.; Dominguez, G.; Thiemens, M.; Fogler, M. M.; Tauber, M. J.; Castro-Neto, A. H.; Lau, C. N.; Keilmann, F.; Basov, D. N. *Nano Letters* **2011,** 11, (11), 4701-4705.
68. Brar, V. W.; Jang, M. S.; Sherrott, M.; Lopez, J. J.; Atwater, H. A. *Nano Letters* **2013,** 13, (6), 2541-2547.

69. Yan, H.; Low, T.; Zhu, W.; Wu, Y.; Freitag, M.; Li, X.; Guinea, F.; Avouris, P.; Xia, F. *Nat Photon* **2013,** 7, (5), 394-399.
70. Liu, Y.; Willis, R. F. *Phys Rev B* **2010,** 81, (8).
71. Koch, R. J.; Seyller, T.; Schaefer, J. A. *Phys Rev B* **2010,** 82, (20).
72. Li, Y.; Yan, H.; Farmer, D. B.; Meng, X.; Zhu, W.; Osgood, R. M.; Heinz, T. F.; Avouris, P. *Nano Letters* **2014,** 14, (3), 1573-1577.
73. Li, Z. Q.; Henriksen, E. A.; Jiang, Z.; Hao, Z.; Martin, M. C.; Kim, P.; Stormer, H. L.; Basov, D. N. *Nat Phys* **2008,** 4, (7), 532.
74. Wang, F.; Zhang, Y. B.; Tian, C. S.; Girit, C.; Zettl, A.; Crommie, M.; Shen, Y. R. *Science* **2008,** 320, (5873), 206.
75. Geick, R.; Perry, C. H.; Rupprecht, G. *Physical Review* **1966,** 146, (2), 543-547.
76. Falkovsky, L. A.; Varlamov, A. A. *Eur. Phys. J. B* **2007,** 56, (4), 281-284.
77. Novotny, L. *Am J Phys* **2010,** 78, (11), 1199-1202.
78. Dintinger, J.; Klein, S.; Bustos, F.; Barnes, W. L.; Ebbesen, T. W. *Phys Rev B* **2005,** 71, (3).
79. Sugawara, Y.; Kelf, T. A.; Baumberg, J. J.; Abdelsalam, M. E.; Bartlett, P. N. *Phys Rev Lett* **2006,** 97, (26).
80. Neubrech, F.; Pucci, A.; Cornelius, T. W.; Karim, S.; Garcia-Etxarri, A.; Aizpurua, J. *Phys Rev Lett* **2008,** 101, (15).
81. Adato, R.; Yanik, A. A.; Amsden, J. J.; Kaplan, D. L.; Omenetto, F. G.; Hong, M. K.; Erramilli, S.; Altug, H. *P Natl Acad Sci USA* **2009,** 106, (46), 19227-19232.
82. Hakala, T. K.; Toppari, J. J.; Kuzyk, A.; Pettersson, M.; Tikkanen, H.; Kunttu, H.; Torma, P. *Phys Rev Lett* **2009,** 103, (5).
83. Nau, D.; Seidel, A.; Orzekowsky, R. B.; Lee, S. H.; Deb, S.; Giessen, H. *Opt Lett* **2010,** 35, (18), 3150-3152.
84. Mak, K. F.; Ju, L.; Wang, F.; Heinz, T. F. *Solid State Commun* **2012,** 152, (15), 1341.
85. Nair, R. R.; Blake, P.; Grigorenko, A. N.; Novoselov, K. S.; Booth, T. J.; Stauber, T.; Peres, N. M. R.; Geim, A. K. *Science* **2008,** 320, (5881), 1308.
86. Emani, N. K.; Chung, T. F.; Kildishev, A. V.; Shalaev, V. M.; Chen, Y. P.; Boltasseva, A. *Nano Letters* **2014,** 14, (1), 78-82.
87. Grande, M.; Stomeo, T.; Bianco, G. V.; Vincenti, M. A.; de Ceglia, D.; Petruzzelli, V.; Bruno, G.; De Vittorio, M.; Scalora, M.; D'Orazio, A. *Applied Physics Letters* **2013,** 102, (23).
88. Yao, Y.; Kats, M. A.; Genevet, P.; Yu, N. F.; Song, Y.; Kong, J.; Capasso, F. *Nano Letters* **2013,** 13, (3), 1257-1264.
89. Yao, Y.; Kats, M. A.; Shankar, R.; Song, Y.; Kong, J.; Loncar, M.; Capasso, F. *Nano Letters* **2014,** 14, (1), 214-219.
90. Zhu, X. L.; Shi, L.; Schmidt, M. S.; Boisen, A.; Hansen, O.; Zi, J.; Xiao, S. S.; Mortensen, N. A. *Nano Letters* **2013,** 13, (10), 4690-4696.
91. Furchi, M.; Urich, A.; Pospischil, A.; Lilley, G.; Unterrainer, K.; Detz, H.; Klang, P.; Andrews, A. M.; Schrenk, W.; Strasser, G.; Mueller, T. *Nano Letters* **2012,** 12, (6), 2773-2777.

92. Gan, X. T.; Mak, K. F.; Gao, Y. D.; You, Y. M.; Hatami, F.; Hone, J.; Heinz, T. F.; Englund, D. *Nano Letters* **2012,** 12, (11), 5626-5631.
93. Majumdar, A.; Kim, J.; Vuckovic, J.; Wang, F. *Nano Letters* **2013,** 13, (2), 515-518.
94. Liu, M.; Yin, X. B.; Ulin-Avila, E.; Geng, B. S.; Zentgraf, T.; Ju, L.; Wang, F.; Zhang, X. *Nature* **2011,** 474, (7349), 64-67.
95. Pospischil, A.; Humer, M.; Furchi, M. M.; Bachmann, D.; Guider, R.; Fromherz, T.; Mueller, T. *Nat Photonics* **2013,** 7, (11), 892-896.
96. Fang, Z. Y.; Thongrattanasiri, S.; Schlather, A.; Liu, Z.; Ma, L. L.; Wang, Y. M.; Ajayan, P. M.; Nordlander, P.; Halas, N. J.; de Abajo, F. J. G. *Acs Nano* **2013,** 7, (3), 2388-2395.
97. Fang, Z. Y.; Wang, Y. M.; Schather, A. E.; Liu, Z.; Ajayan, P. M.; de Abajo, F. J. G.; Nordlander, P.; Zhu, X.; Halas, N. J. *Nano Letters* **2014,** 14, (1), 299-304.
98. Yan, H. G.; Li, X. S.; Chandra, B.; Tulevski, G.; Wu, Y. Q.; Freitag, M.; Zhu, W. J.; Avouris, P.; Xia, F. N. *Nature nanotechnology* **2012,** 7, (5), 330-334.
99. Avitzour, Y.; Urzhumov, Y. A.; Shvets, G. *Physical Review B* **2009,** 79, (4), 045131.
100. Landy, N. I.; Sajuyigbe, S.; Mock, J. J.; Smith, D. R.; Padilla, W. J. *Phys Rev Lett* **2008,** 100, (20).
101. Liu, N.; Mesch, M.; Weiss, T.; Hentschel, M.; Giessen, H. *Nano Letters* **2010,** 10, (7), 2342-2348.
102. Mason, J. A.; Smith, S.; Wasserman, D. *Applied Physics Letters* **2011,** 98, (24).
103. Wu, C.; Neuner, B., III; Shvets, G.; John, J.; Milder, A.; Zollars, B.; Savoy, S. *Physical Review B* **2011,** 84, (7), 075102.
104. Salisbury, W. W. Absorbent Body for Electromagnetic Waves. 1952.
105. Tittl, A.; Mai, P.; Taubert, R.; Dregely, D.; Liu, N.; Giessen, H. *Nano Letters* **2011,** 11, (10), 4366-4369.
106. Alaee, R.; Farhat, M.; Rockstuhl, C.; Lederer, F. *Opt. Express* **2012,** 20, (27), 28017-28024.
107. Thongrattanasiri, S.; Koppens, F. H. L.; de Abajo, F. J. G. *Physical Review Letters* **2012,** 108, (4).
108. Ju, L.; Geng, B. S.; Horng, J.; Girit, C.; Martin, M.; Hao, Z.; Bechtel, H. A.; Liang, X. G.; Zettl, A.; Shen, Y. R.; Wang, F. *Nature nanotechnology* **2011,** 6, (10), 630-634.
109. Yan, H. G.; Low, T.; Zhu, W. J.; Wu, Y. Q.; Freitag, M.; Li, X. S.; Guinea, F.; Avouris, P.; Xia, F. N. *Nat Photonics* **2013,** 7, (5), 394-399.
110. Cataldo, G.; Beall, J. A.; Cho, H. M.; McAndrew, B.; Niemack, M. D.; Wollack, E. J. *Opt Lett* **2012,** 37, (20), 4200-4202.
111. Hwang, E. H.; Sensarma, R.; Das Sarma, S. *Physical Review B* **2010,** 82, (19), 195406.
112. Greffet, J.; Carminati, R.; Joulain, K.; Mulet, J.; Mainguy, S.; Chen, Y. *Nature* **2002,** 416, (6876), 61-64.
113. Han, S. E.; Norris, D. J. *Optics Express* **2010,** 18, (5), 4829-4837.

114. Cornelius, C.; Dowling, J. *Physical Review A* **1999,** 59, (6), 4736-4746.
115. Schuller, J. A.; Taubner, T.; Brongersma, M. L. *Nature Photonics* **2009,** 3, (11), 658-661.
116. Liu, X.; Tyler, T.; Starr, T.; Starr, A. F.; Jokerst, N. M.; Padilla, W. J. *Physical Review Letters* **2011,** 107, (4), 045901.
117. Kats, M. A.; Blanchard, R.; Zhang, S.; Genevet, P.; Ko, C.; Ramanathan, S.; Capasso, F. *Physical Review X* **2013,** 3, (4), 041004.
118. Vassant, S.; Doyen, I. M.; Marquier, F.; Pardo, F.; Gennser, U.; Cavanna, A.; Pelouard, J. L.; Greffet, J. J. *Applied Physics Letters* **2013,** 102, (8), 081125.
119. Mak, K. F.; Ju, L.; Wang, F.; Heinz, T. F. *Solid State Commun* **2012,** 152, (15), 1341-1349.
120. Horng, J.; Chen, C.-F.; Geng, B.; Girit, C.; Zhang, Y.; Hao, Z.; Bechtel, H. A.; Martin, M.; Zettl, A.; Crommie, M. F.; Shen, Y. R.; Wang, F. *Physical Review B* **2011,** 83, (16), 165113.
121. Freitag, M.; Chiu, H.-Y.; Steiner, M.; Perebeinos, V.; Avouris, P. *Nat Nano* **2010,** 5, (7), 497-501.
122. Hwang, E. H.; Das Sarma, S. *Phys Rev B* **2007,** 75, (20), 205418.
123. Jablan, M.; Buljan, H.; Soljacic, M. *Physical Review B* **2009,** 80, (24), 245435.
124. Polini, M.; Asgari, R.; Borghi, G.; Barlas, Y.; Pereg-Barnea, T.; MacDonald, A. H. *Phys Rev B* **2008,** 77, (8), 081411.
125. Chaplik, A. V. *Surface Science Reports* **1985,** 5, (7), 289-335.
126. Otsuji, T.; Popov, V.; Ryzhii, V. *J Phys D Appl Phys* **2014,** 47, (9), 094006.
127. Rana, F. *Ieee T Nanotechnol* **2008,** 7, (1), 91-99.
128. Rana, F.; George, P. A.; Strait, J. H.; Dawlaty, J. *2008 33rd International Conference on Infrared, Millimeter and Terahertz Waves, Vols 1 and 2* **2008**, 356-358.
129. Brar, V. W.; Jang, M. S.; Sherrott, M.; Kim, S.; Lopez, J. J.; Kim, L. B.; Choi, M.; Atwater, H. *Nano Letters* **2014,** 14, (7), 3876-3880.
130. Ju, L.; Geng, B.; Horng, J.; Girit, C.; Martin, M.; Hao, Z.; Bechtel, H. A.; Liang, X.; Zettl, A.; Shen, Y. R.; Wang, F. *Nat Nano* **2011,** 6, (10), 630-634.
131. Svetovoy, V. B.; van Zwol, P. J.; Chevrier, J. *Physical Review B* **2012,** 85, (15), 155418.
132. van Zwol, P. J.; Thiele, S.; Berger, C.; de Heer, W. A.; Chevrier, J. *Physical Review Letters* **2012,** 109, (26), 264301.
133. Koppens, F. H. L.; Chang, D. E.; Javier Garcia de Abajo, F. *Nano Letters* **2011,** 11, (8), 3370-3377.
134. Jang, M. S.; Brar, V. W.; Sherrott, M. C.; Lopez, J. J.; Kim, L.; Kim, S.; Choi, M.; Atwater, H. A. *Physical Review B* **2014,** 90, (16), 165409.
135. Thongrattanasiri, S.; Koppens, F. H. L.; García de Abajo, F. J. *Physical Review Letters* **2012,** 108, (4), 047401.
136. Dogan, A. The Reliability of the Silicon Nitride Dielectric in Capacitive MEMS Switches. The Pennsylvania State University, 2005.
137. Principi, A.; Vignale, G.; Carrega, M.; Polini, M. *Physical Review B* **2013,** 88, (19), 195405.

138. Biteen, J. S.; Sweatlock, L. A.; Mertens, H.; Lewis, N. S.; Polman, A.; Atwater, H. A. *Journal of Physical Chemistry C* **2007,** 111, (36), 13372-13377.
139. Gersten, J.; Nitzan, A. *Journal of Chemical Physics* **1981,** 75, (3), 1139-1152.
140. Kummerlen, J.; Leitner, A.; Brunner, H.; Aussenegg, F.; Wokaun, A. *Molecular Physics* **1993,** 80, (5), 1031-1046.
141. Novotny, L.; van Hulst, N. *Nature Photonics* **2011,** 5, (2), 83-90.
142. Fei, Z.; Andreev, G. O.; Bao, W.; Zhang, L. M.; A, S. M.; Wang, C.; Stewart, M. K.; Zhao, Z.; Dominguez, G.; Thiemens, M.; Fogler, M. M.; Tauber, M. J.; Castro-Neto, A. H.; Lau, C. N.; Keilmann, F.; Basov, D. N. *Nano Lett* **2011,** 11, (11), 4701–4705.
143. Gaudreau, L.; Tielrooij, K. J.; Prawiroatmodjo, G. E. D. K.; Osmond, J.; Garcia de Abajo, F. J.; Koppens, F. H. L. *Nano Letters* **2013,** 13, (5), 2030-2035.
144. Mortimer, R. J. *Chemical Society Reviews* **1997,** 26, (3), 147-156.
145. Purcell, E. M. *Phys Rev* **1946,** 69, (11-1), 681-681.
146. Francardi, M.; Balet, L.; Gerardino, A.; Chauvin, N.; Bitauld, D.; Li, L. H.; Alloing, B.; Fiore, A. *Appl Phys Lett* **2008,** 93, (14), 143102.
147. Kumar, N. R.; Messer, K.; Eggleston, M.; Wu, M. C.; Yablonovitch, E. *2012 Ieee Photonics Conference (Ipc)* **2012**, 612-613.
148. Lau, E. K.; Lakhani, A.; Tucker, R. S.; Wu, M. C. *Opt Express* **2009,** 17, (10), 7790-7799.
149. Okamoto, K.; Niki, I.; Scherer, A.; Narukawa, Y.; Mukai, T.; Kawakami, Y. *Appl Phys Lett* **2005,** 87, (7), 071102.
150. Vuckovic, J.; Loncar, M.; Scherer, A. *Ieee J Quantum Elect* **2000,** 36, (10), 1131-1144.
151. Sidiropoulos, T. P. H.; Roder, R.; Geburt, S.; Hess, O.; Maier, S. A.; Ronning, C.; Oulton, R. F. *Nat Phys* **2014,** 10, (11), 870-876.
152. Cai, T.; Wang, G. M.; Zhang, X. F.; Liang, J. G.; Zhuang, Y. Q.; Liu, D.; Xu, H. X. *Ieee T Antenn Propag* **2015,** 63, (12), 5629-5636.
153. Guo, W. L.; Wang, G. M.; Ding, S. S.; Li, H. P.; Cai, T. *Chinese Phys B* **2016,** 25, (8).
154. Guo, W. L.; Wang, G. M.; Li, H. P.; Zhuang, Y. Q.; Shuai, C. Y. *Appl Phys a-Mater* **2017,** 123, (1).
155. Guo, W. L.; Wang, G. M.; Li, T. J. *9th International Conference on Microwave and Millimeter Wave Technology Proceedings, Vol. 1, (Icmmt 2016)* **2016**, 458-460.
156. Guo, Z. Y.; Zhu, L.; Shen, F.; Zhou, H. P.; Gao, R. K. *Rsc Adv* **2017,** 7, (16), 9872-9879.
157. Khorasaninejad, M.; Zhu, W.; Crozier, K. B. *Optica* **2015,** 2, (4), 376-382.
158. Kim, J.; Choudbury, S.; DeVault, C.; Zhao, Y.; Kildishev, A. V.; Shalaev, V. M.; Alu, A.; Boltasseva, A. *Acs Nano* **2016,** 10, (10), 9326-9333.
159. Slovick, B. A.; Zhou, Y.; Yu, Z. G.; Kravchenko, I. I.; Briggs, D. P.; Moitra, P.; Krishnamurthy, S.; Valentine, J. *Philos T R Soc A* **2017,** 375, (2090).
160. Xiang, J.; Li, J. X.; Li, H.; Zhang, C. Y.; Dai, Q. F.; Tie, S. L.; Lan, S. *Opt Express* **2016,** 24, (11), 1420-1434.

161. Yang, Y. M.; Kelley, K.; Sachet, E.; Campione, S.; Luk, T. S.; Maria, J. P.; Sinclair, M. B.; Brener, I. *Nat Photonics* **2017,** 11, (6), 390-+.
162. Dean, C. R.; Young, A. F.; Meric, I.; Lee, C.; Wang, L.; Sorgenfrei, S.; Watanabe, K.; Taniguchi, T.; Kim, P.; Shepard, K. L.; Hone, J. *Nat Nanotechnol* **2010,** 5, (10), 722-726.
163. Ni, G. X.; Wang, L.; Goldflam, M. D.; Wagner, M.; Fei, Z.; McLeod, A. S.; Liu, M. K.; Keilmann, F.; Ozyilmaz, B.; Neto, A. H. C.; Hone, J.; Fogler, M. M.; Basov, D. N. *Nat Photonics* **2016,** 10, (4), 244-+.
164. Sun, S. L.; Yang, K. Y.; Wang, C. M.; Juan, T. K.; Chen, W. T.; Liao, C. Y.; He, Q.; Xiao, S. Y.; Kung, W. T.; Guo, G. Y.; Zhou, L.; Tsai, D. P. *Nano Lett* **2012,** 12, (12), 6223-6229.
165. Park, J.; Kang, J. H.; Liu, X.; Brongersma, M. L. *Scientific reports* **2015,** 5, 15754.
166. Dicken, M. J.; Aydin, K.; Pryce, I. M.; Sweatlock, L. A.; Boyd, E. M.; Walavalkar, S.; Ma, J.; Atwater, H. A. *Opt Express* **2009,** 17, (20), 18330-18339.
167. Li, Z.; Yu, N. *Appl Phys Lett* **2013,** 102, (13), 131108.
168. Ou, J. Y.; Plum, E.; Zhang, J. F.; Zheludev, N. I. *Nat Nanotechnol* **2013,** 8, (4), 252-255.
169. Zheludev, N. I.; Kivshar, Y. S. *Nat Mater* **2012,** 11, (11), 917-924.
170. Ma, F. S.; Lin, Y. S.; Zhang, X. H.; Lee, C. *Light-Sci Appl* **2014,** 3.
171. Zhu, A. Y.; Kuznetsov, A. I.; Luk'yanchuk, B.; Engheta, N.; Genevet, P. *Nanophotonics* **2016**.
172. Shaltout, A. M.; Kinsey, N.; Kim, J.; Chandrasekar, R.; Ndukaife, J. C.; Boltasseva, A.; Shalaev, V. M. *P Ieee* **2016,** 104, (12), 2270-2287.
173. de Abajo, F. J. G.; Koppens, F. H. L.; Chang, D. E.; Thongrattanasiri, S. *Aip Conf Proc* **2011,** 1398.
174. Falkovsky, L. A. *Journal of Physics: Conference Series* **2008,** 129, (1), 012004.
175. Koppens, F. H. L.; Chang, D. E.; de Abajo, F. J. G. *Nano Lett* **2011,** 11, (8), 3370-3377.
176. Bonaccorso, F.; Sun, Z.; Hasan, T.; Ferrari, A. C. *Nat Photonics* **2010,** 4, (9), 611-622.
177. Geim, A. K.; Novoselov, K. S. *Nat Mater* **2007,** 6, (3), 183-91.
178. Fei, Z.; Rodin, A. S.; Andreev, G. O.; Bao, W.; McLeod, A. S.; Wagner, M.; Zhang, L. M.; Zhao, Z.; Thiemens, M.; Dominguez, G.; Fogler, M. M.; Castro Neto, A. H.; Lau, C. N.; Keilmann, F.; Basov, D. N. *Nature* **2012,** 487, (7405), 82-85.
179. Li, Z. Q.; Henriksen, E. A.; Jiang, Z.; Hao, Z.; Martin, M. C.; Kim, P.; Stormer, H. L.; Basov, D. N. *Nat Phys* **2008,** 4, (7), 532-535.
180. Phare, C. T.; Lee, Y. H. D.; Cardenas, J.; Lipson, M. *Nat Photonics* **2015,** 9, (8), 511-+.
181. Resler, D. P.; Hobbs, D. S.; Sharp, R. C.; Friedman, L. J.; Dorschner, T. A. *Optics letters* **1996,** 21, (9), 689-691.
182. Shim, S. H.; Strasfeld, D. B.; Fulmer, E. C.; Zanni, M. T. *Optics letters* **2006,** 31, (6), 838-840.

183. Shelton, D. J.; Coffey, K. R.; Boreman, G. D. *Opt Express* **2010,** 18, (2), 1330-1335.
184. Dabidian, N.; Dutta-Gupta, S.; Kholmanov, I.; Lai, K. F.; Lu, F.; Lee, J.; Jin, M. Z.; Trendafilov, S.; Khanikaev, A.; Fallahazad, B.; Tutuc, E.; Belkin, M. A.; Shvets, G. *Nano Lett* **2016,** 16, (6), 3607-3615.
185. Park, J.; Kang, J.-H.; Kim, S. J.; Liu, X.; Brongersma, M. L. *Nano Lett* **2016**.
186. Aydin, K.; Ferry, V. E.; Briggs, R. M.; Atwater, H. A. *Nature Communications* **2011,** 2.
187. Wu, C. H.; Neuner, B.; Shvets, G.; John, J.; Milder, A.; Zollars, B.; Savoy, S. *Phys Rev B* **2011,** 84, (7).
188. Avitzour, Y.; Urzhumov, Y. A.; Shvets, G. *Phys Rev B* **2009,** 79, (4).
189. Levesque, P. L.; Sabri, S. S.; Aguirre, C. M.; Guillemette, J.; Siaj, M.; Desjardins, P.; Szkopek, T.; Martel, R. *Nano Lett* **2011,** 11, (1), 132-137.
190. Jang, M. S.; Brar, V. W.; Sherrott, M. C.; Lopez, J. J.; Kim, L.; Kim, S.; Choi, M.; Atwater, H. A. *Phys Rev B* **2014,** 90, (16).
191. Huang, Y. W.; Lee, H. W. H.; Sokhoyan, R.; Pala, R. A.; Thyagarajan, K.; Han, S.; Tsa, D. P.; Atwater, H. A. *Nano Lett* **2016,** 16, (9), 5319-5325.
192. Stutzman, W. L.; Thiele, G. A., *Antenna Theory and Design*. John Wiley & Sons: 1998.
193. Steinberg, B. D., *Principles of Aperture and Array System Design Including Random and Adaptive Arrays*. John Wiley & Sons: 1976.
194. Koppens, F. H. L.; Mueller, T.; Avouris, P.; Ferrari, A. C.; Vitiello, M. S.; Polini, M. *Nature nanotechnology* **2014,** 9, (10), 780-793.
195. Sun, Z. P.; Martinez, A.; Wang, F. *Nat Photonics* **2016,** 10, (4), 227-238.
196. Wang, Q. H.; Kalantar-Zadeh, K.; Kis, A.; Coleman, J. N.; Strano, M. S. *Nature nanotechnology* **2012,** 7, (11), 699-712.
197. Xia, F. N.; Wang, H.; Xiao, D.; Dubey, M.; Ramasubramaniam, A. *Nature Photonics* **2014,** 8, (12), 899-907.
198. Castellanos-Gomez, A. *The Journal of Physical Chemistry Letters* **2015,** 6, (21), 4280-4291.
199. Ling, X.; Wang, H.; Huang, S. X.; Xia, F. N.; Dresselhaus, M. S. *Proc. Natl. Acad. Sci. U.S.A.* **2015,** 112, (15), 4523-4530.
200. Li, L.; Yu, Y.; Ye, G. J.; Ge, Q.; Ou, X.; Wu, H.; Feng, D.; Chen, X. H.; Zhang, Y. *Nat. Nanotechnol.* **2014,** 9, (5), 372-7.
201. Xia, F. N.; Wang, H.; Jia, Y. C. *Nat Commun* **2014,** 5.
202. Liu, H.; Neal, A. T.; Zhu, Z.; Luo, Z.; Xu, X. F.; Tomanek, D.; Ye, P. D. *Acs Nano* **2014,** 8, (4), 4033-4041.
203. Du, Y.; Liu, H.; Deng, Y.; Ye, P. D. *Acs Nano* **2014,** 8, (10), 10035-10042.
204. Liu, H.; Du, Y.; Deng, Y.; Ye, P. D. *Chemical Society Reviews* **2015,** 44, (9), 2732-2743.
205. Xia, F.; Wang, H.; Jia, Y. *Nat Commun* **2014,** 5, 4458.
206. Buscema, M.; Groenendijk, D. J.; Blanter, S. I.; Steele, G. A.; van der Zant, H. S. J.; Castellanos-Gomez, A. *Nano Letters* **2014,** 14, (6), 3347-3352.
207. Yuan, H. T.; Liu, X. G.; Afshinmanesh, F.; Li, W.; Xu, G.; Sun, J.; Lian, B.; Curto, A. G.; Ye, G. J.; Hikita, Y.; Shen, Z. X.; Zhang, S. C.; Chen, X. H.;

Brongersma, M.; Hwang, H. Y.; Cui, Y. *Nat. Nanotechnol.* **2015,** 10, (8), 707-713.
208. Youngblood, N.; Chen, C.; Koester, S. J.; Li, M. *Nature Photonics* **2015,** 9, (4), 247-252.
209. Engel, M.; Steiner, M.; Avouris, P. *Nano Letters* **2014,** 14, (11), 6414-6417.
210. Woomer, A. H.; Farnsworth, T. W.; Hu, J.; Wells, R. A.; Donley, C. L.; Warren, S. C. *Acs Nano* **2015,** 9, (9), 8869-8884.
211. Yang, J.; Xu, R. J.; Pei, J. J.; Myint, Y. W.; Wang, F.; Wang, Z.; Zhang, S.; Yu, Z. F.; Lu, Y. R. *Light-Sci Appl* **2015,** 4.
212. Zhang, S.; Yang, J.; Xu, R. J.; Wang, F.; Li, W. F.; Ghufran, M.; Zhang, Y. W.; Yu, Z. F.; Zhang, G.; Qin, Q. H.; Lu, Y. R. *Acs Nano* **2014,** 8, (9), 9590-9596.
213. Surrente, A.; Mitioglu, A. A.; Galkowski, K.; Klopotowski, L.; Tabis, W.; Vignolle, B.; Maude, D. K.; Plochocka, P. *Phys Rev B* **2016,** 94, (7).
214. Surrente, A.; Mitioglu, A. A.; Galkowski, K.; Tabis, W.; Maude, D. K.; Plochocka, P. *Phys Rev B* **2016,** 93, (12).
215. Deng, Y.; Luo, Z.; Conrad, N. J.; Liu, H.; Gong, Y.; Najmaei, S.; Ajayan, P. M.; Lou, J.; Xu, X.; Ye, P. D. *Acs Nano* **2014,** 8, (8), 8292-8299.
216. Buscema, M.; Groenendijk, D. J.; Steele, G. A.; van der Zant, H. S. J.; Castellanos-Gomez, A. *Nat Commun* **2014,** 5.
217. Peng, C.; Jianyong, X.; Hua, Y.; Jing, z.; Guibai, X.; Shuang, W.; Xiaobo, L.; Guole, W.; Jing, Z.; Fusheng, W.; Zhongyuan, L.; Rong, Y.; Dongxia, S.; Guangyu, Z. *2d Mater* **2015,** 2, (3), 034009.
218. Jeon, P. J.; Lee, Y. T.; Lim, J. Y.; Kim, J. S.; Hwang, D. K.; Im, S. *Nano letters* **2016,** 16, (2), 1293-1298.
219. Wang, H.; Wang, X.; Xia, F.; Wang, L.; Jiang, H.; Xia, Q.; Chin, M. L.; Dubey, M.; Han, S.-j. *Nano Letters* **2014,** 14, (11), 6424-6429.
220. Likai Li, J. K., Chenhao Jin, Guojun Ye, Diana Y. Qiu, Felipe H. da Jornada, Zhiwen Shi, Long Chen, Zuocheng Zhang, Fangyuan Yang, Kenji Watanabe, Takashi Taniguchi, Wencai Ren, Steven G. Louie, Xianhui Chen, Yuanbo Zhang and Feng Wang. *arXiv:1601.03103* **2016**.
221. Wang, X. M.; Jones, A. M.; Seyler, K. L.; Tran, V.; Jia, Y. C.; Zhao, H.; Wang, H.; Yang, L.; Xu, X. D.; Xia, F. N. *Nature nanotechnology* **2015,** 10, (6), 517-521.
222. Tran, V.; Soklaski, R.; Liang, Y. F.; Yang, L. *Physical Review B* **2014,** 89, (23).
223. Kim, J.; Baik, S. S.; Ryu, S. H.; Sohn, Y.; Park, S.; Park, B. G.; Denlinger, J.; Yi, Y.; Choi, H. J.; Kim, K. S. *Science* **2015,** 349, (6249), 723-6.
224. Brar, V. W.; Sherrott, M. C.; Jang, M. S.; Kim, S.; Kim, L.; Choi, M.; Sweatlock, L. A.; Atwater, H. A. *Nat. Commun.* **2015,** 6.
225. De Zoysa, M.; Asano, T.; Mochizuki, K.; Oskooi, A.; Inoue, T.; Noda, S. *Nature Photon.* **2012,** 6, (8), 535-539.
226. Bermel, P.; Ghebrebrhan, M.; Chan, W.; Yeng, Y. X.; Araghchini, M.; Hamam, R.; Marton, C. H.; Jensen, K. F.; Soljačić, M.; Joannopoulos, J. D.; Johnson, S. G.; Celanovic, I. *Opt. Express* **2010,** 18, (S3), A314-A334.

227. Liu, M.; Yin, X.; Ulin-Avila, E.; Geng, B.; Zentgraf, T.; Ju, L.; Wang, F.; Zhang, X. *Nature* **2011,** 474, (7349), 64-67.
228. Low, T.; Roldán, R.; Wang, H.; Xia, F.; Avouris, P.; Moreno, L. M.; Guinea, F. *Phys. Rev. Lett.* **2014,** 113, (10), 106802.
229. Liu, Z.; Aydin, K. *Nano Letters* **2016,** 16, (6), 3457-3462.
230. Chaves, A.; Low, T.; Avouris, P.; Cakir, D.; Peeters, F. M. *Phys. Rev. B* **2015,** 91, (15).
231. Low, T.; Rodin, A. S.; Carvalho, A.; Jiang, Y.; Wang, H.; Xia, F.; Castro Neto, A. H. *Physical Review B* **2014,** 90, (7), 075434.
232. Lin, C.; Grassi, R.; Low, T.; Helmy, A. S. *Nano letters* **2016,** 16, (3), 1683-9.
233. Favron, A.; Gaufres, E.; Fossard, F.; Phaneuf-L'Heureux, A. L.; Tang, N. Y. W.; Levesque, P. L.; Loiseau, A.; Leonelli, R.; Francoeur, S.; Martel, R. *Nat Mater* **2015,** 14, (8), 826-+.
234. Tayari, V.; Hemsworth, N.; Fakih, I.; Favron, A.; Gaufres, E.; Gervais, G.; Martel, R.; Szkopek, T. *Nat Commun* **2015,** 6.
235. Castellanos-Gomez, A.; Vicarelli, L.; Prada, E.; Island, J. O.; Narasimha-Acharya, K. L.; Blanter, S. I.; Groenendijk, D. J.; Buscema, M.; Steele, G. A.; Alvarez, J. V.; Zandbergen, H. W.; Palacios, J. J.; van der Zant, H. S. J. *2d Mater* **2014,** 1, (2).
236. Burstein, E. *Phys Rev* **1954,** 93, (3), 632-633.
237. Moss, T. S. *P Phys Soc Lond B* **1954,** 67, (418), 775-782.
238. Tian, H.; Guo, Q.; Xie, Y.; Zhao, H.; Li, C.; Cha, J. J.; Xia, F.; Wang, H. *Advanced Materials* **2016,** 28, (25), 4991-4997.
239. Miller, D. A. B.; Chemla, D. S.; Schmitt-Rink, S. *Phys. Rev. B* **1986,** 33, (10), 6976-6982.
240. Zhang, G.; Chaves, A.; Huang, S.; Song, C.; Low, T.; Yan, H., Infrared fingerprints of few-layer black phosphorus. In *ArXiv e-prints*, 2016; Vol. 1607.
241. Guowei Zhang, A. C., Shenyang Huang, Chaoyu Song, Tony Low,; Yan, H. *arXiv:1607.08049* **2016**.
242. Mak, K. F.; He, K.; Lee, C.; Lee, G. H.; Hone, J.; Heinz, T. F.; Shan, J. *Nature Materials* **2013,** 12, (3), 207-211.
243. Li, D.; Xu, J.-R.; Ba, K.; Xuan, N.; Chen, M.; Sun, Z.; Zhang, Y.-Z.; Zhang, Z. *2D Materials* **2017,** 4, (3), 031009.
244. Chen, C.; Youngblood, N.; Li, M. *2015 Optoelectron. Glob. Conf. OGC* **2015,** 2015, 1 - 3.
245. Chen, C.; Youngblood, N.; Peng, R.; Yoo, D.; Mohr, D. A.; Johnson, T. W.; Oh, S.-H.; Li, M. *Nano Letters* **2017,** 17, (2), 985 - 991.
246. Huang, M.; Wang, M.; Chen, C.; Ma, Z.; Li, X.; Han, J.; Wu, Y. *Advanced Materials* **2016,** 28, (18), 3481 - 3485.
247. Wang, T.; Hu, S.; Chamlagain, B.; Hong, T.; Zhou, Z.; Weiss, S. M.; Xu, Y.-Q. *Advanced Materials* **2016,** 28, (33), 7162-7166.
248. Youngblood, N.; Chen, C.; Koester, S. J.; Li, M. *2015 Conference on Lasers and Electro-Optics (CLEO)* **2015**, 1-2.

249. Deng, B.; Tran, V.; Xie, Y.; Jiang, H.; Li, C.; Guo, Q.; Wang, X.; Tian, H.; Koester, S. J.; Wang, H.; Cha, J. J.; Xia, Q.; Yang, L.; Xia, F. *Nature Communications* **2017,** 8, (14474).
250. Kim, J.; Baik, S. S.; Ryu, S. H.; Sohn, Y.; Park, S.; Park, B.-G.; Denlinger, J.; Yi, Y.; Choi, H. J.; Kim, K. S. *Science* **2015,** 349, (6249), 723 - 726.
251. Liu, Y.; Qiu, Z.; Carvalho, A.; Bao, Y.; Xu, H.; Tan, S. J. R.; Liu, W.; Castro Neto, A. H.; Loh, K. P.; Lu, J. *Nano Letters* **2017,** 17, (3), 1970-1977.
252. Wang, X.; Jones, A. M.; Seyler, K. L.; Tran, V.; Jia, Y.; Zhao, H.; Wang, H.; Yang, L.; Xu, X.; Xia, F. *Nature Nanotechnology* **2015,** 10, (6), 517-521.
253. Zhang, G.; Huang, S.; Chaves, A.; Song, C.; Özçelik, V. O.; Low, T.; Yan, H. *Nature Communications* **2017,** 8, 14071.
254. Wei, Q.; Peng, X. *Applied Physics Letters* **2014,** 104, (25), 251915.
255. Luo, Z.; Maassen, J.; Deng, Y.; Du, Y.; Garrelts, R. P.; Lundstrom, M. S.; Ye, P. D.; Xu, X. *Nature Communications* **2015,** 6.
256. Liao, B.; Zhao, H.; Najafi, E.; Yan, X.; Tian, H.; Tice, J.; Minnich, A. J.; Wang, H.; Zewail, A. H. *Nano Letters* **2017,** 17, (6), 3675-3680.
257. Yuan, H.; Liu, X.; Afshinmanesh, F.; Li, W.; Xu, G.; Sun, J.; Lian, B.; Curto, A. G.; Ye, G.; Hikita, Y.; Shen, Z.; Zhang, S.-C.; Chen, X.; Brongersma, M.; Hwang, H. Y.; Cui, Y. *Nature Nanotechnology* **2015,** 10, (8), 707-713.
258. Xia, F.; Wang, H.; Jia, Y. *Nature Communications* **2014,** 5, 5458.
259. Lan, S.; Rodrigues, S.; Kang, L.; Cai, W. *ACS Photonics* **2016,** 3, (7), 1176 - 1181.
260. Qiao, J.; Kong, X.; Hu, Z.-X.; Yang, F.; Ji, W. *Nature Communications* **2014,** 5, 5475.
261. Sherrott, M. C.; Hon, P. W. C.; Fountaine, K. T.; Garcia, J. C.; Ponti, S. M.; Brar, V. W.; Sweatlock, L. A.; Atwater, H. A. *Nano Letters* **2017,** 17, (5), 3027-3034.
262. Huang, Y.-W.; Lee, H. W. H.; Sokhoyan, R.; Pala, R. A.; Thyagarajan, K.; Han, S.; Tsai, D. P.; Atwater, H. A. *Nano Letters* **2016,** 16, (9), 5319 - 5325.
263. Park, J.; Kang, J.-H.; Kim, S. J.; Liu, X.; Brongersma, M. L. *Nano Letters* **2017,** 17, (1), 407-413.
264. Xu, Q.; Schmidt, B.; Pradhan, S.; Lipson, M. *Nature* **2005,** 435, (7040), 325-327.
265. Kuo, Y.-H.; Lee, Y. K.; Ge, Y.; Ren, S.; Roth, J. E.; Kamins, T. I.; Miller, D. A. B.; Harris, J. S. *Nature* **2005,** 437, (7063), 1334 - 1336.
266. Brar, V. W.; Sherrott, M. C.; Jang, M. S.; Kim, S.; Kim, L.; Choi, M.; Sweatlock, L. A.; Atwater, H. A. *Nature Communications* **2015,** 6, 7032.
267. Coppens, Z. J.; Valentine, J. G. *Advanced Materials* 29, (39), 1701275.
268. Inoue, T.; Zoysa, M. D.; Asano, T.; Noda, S. *Nature Materials* **2014,** 13, (10), 928 - 931.
269. Lin, C.; Grassi, R.; Low, T.; Helmy, A. S. *Nano Letters* **2016,** 16, (3), 1683-1689.
270. Whitney, W. S.; Sherrott, M. C.; Jariwala, D.; Lin, W.-H.; Bechtel, H. A.; Rossman, G. R.; Atwater, H. A. *Nano Letters* **2017,** 17, (1), 78-84.
271. Burstein, E. **1954,** 93, (3), 632-633.

272. Moss, T. S. *Proceedings of the Physical Society. Section B* **1957,** 70, (2), 247.
273. Ling, X.; Huang, S.; Hasdeo, E. H.; Liang, L.; Parkin, W. M.; Tatsumi, Y.; Nugraha, A. R. T.; Puretzky, A. A.; Das, P. M.; Sumpter, B. G.; Geohegan, D. B.; Kong, J.; Saito, R.; Drndic, M.; Meunier, V.; Dresselhaus, M. S. *Nano Letters* **2016,** 16, (4), 2260-2267.
274. Sim, S.; Lee, D.; Noh, M.; Cha, S.; Soh, C. H.; Sung, J. H.; Jo, M.-H.; Choi, H. *Nature Communications* **2016,** 7, 13569.
275. Dolui, K.; Quek, S. Y. *Scientific Reports* **2015,** 5, (11699).
276. Chernikov, A.; van der Zande, A. M.; Hill, H. M.; Rigosi, A. F.; Velauthapillai, A.; Hone, J.; Heinz, T. F. *Physical Review Letters* **2015,** 115, (12), 126802.
277. Brar, V. W.; Jang, M. S.; Sherrott, M.; Lopez, J. J.; Atwater, H. A. **2013,** 13, (6), 2547.
278. Basov, D. N.; Fogler, M. M.; de Abajo, F. J. G. *Science* **2016,** 354, (6309).
279. Wong, J.; Jariwala, D.; Tagliabue, G.; Tat, K.; Davoyan, A. R.; Sherrott, M. C.; Atwater, H. A. *Acs Nano* **2017,** 11, (7), 7230-7240.
280. Kang, K.; Lee, K. H.; Han, Y. M.; Gao, H.; Xie, S. E.; Muller, D. A.; Park, J. *Nature* **2017,** 550, (7675), 229-233.
281. Lin, Z.; McCreary, A.; Briggs, N.; Subramanian, S.; Zhang, K. H.; Sun, Y. F.; Li, X. F.; Borys, N. J.; Yuan, H. T.; Fullerton-Shirey, S. K.; Chernikov, A.; Zhao, H.; McDonnell, S.; Lindenberg, A. M.; Xiao, K.; LeRoy, B. J.; Drndic, M.; Hwang, J. C. M.; Park, J.; Chhowalla, M.; Schaak, R. E.; Javey, A.; Hersam, M. C.; Robinson, J.; Terrones, M. *2d Materials* **2016,** 3, (4).
282. Greffet, J. J.; Carminati, R.; Joulain, K.; Mulet, J. P.; Mainguy, S. P.; Chen, Y. *Nature* **2002,** 416, (6876), 61-64.
283. St-Gelais, R.; Zhu, L. X.; Fan, S. H.; Lipson, M. *Nature Nanotechnology* **2016,** 11, (6), 515-+.
284. Ilic, O.; Jablan, M.; Joannopoulos, J. D.; Celanovic, I.; Buljan, H.; Soljacic, M. *Physical Review B* **2012,** 85, (15).
285. Zhao, B.; Guizal, B.; Zhang, Z. M. M.; Fan, S. H.; Antezza, M. *Physical Review B* **2017,** 95, (24).
286. Rodrigo, D.; Limaj, O.; Janner, D.; Etezadi, D.; de Abajo, F. J. G.; Pruneri, V.; Altug, H. *Science* **2015,** 349, (6244), 165-168.
287. Couto, N. J. G.; Sacépé, B.; Morpurgo, A. F. *Physical Review Letters* **2011,** 107, (22), 225501.
288. Sachs, R., Electron Transport and Scattering in Graphene Devices Transferred to SrTiO3 Substrates. Thesis; University of California Riverside: Physics, 2013.
289. Buchheim, J.; Wyss, R. M.; Shorubalko, I.; Park, H. G. *Nanoscale* **2016,** 8, (15), 8345-8354.
290. Hype Cycle Research Methodology | Gartner Inc. https://http://www.gartner.com/technology/research/methodologies/hype-cycle.jsp (December 17),

291. Jariwala, D.; Dayoyan, A. R.; Tagliabue, G.; Sherrott, M. C.; Wong, J.; Atwater, H. A. *Nano Letters* **2016,** 16, (9), 5482-5487.
292. Chernikov, A.; van der Zande, A. M.; Hill, H. M.; Rigosi, A. F.; Velauthapillai, A.; Hone, J.; Heinz, T. F. *Physical Review Letters* **2015,** 115, (12).
293. Amani, M.; Lien, D. H.; Kiriya, D.; Xiao, J.; Azcatl, A.; Noh, J.; Madhvapathy, S. R.; Addou, R.; Santosh, K. C.; Dubey, M.; Cho, K.; Wallace, R. M.; Lee, S. C.; He, J. H.; Ager, J. W.; Zhang, X.; Yablonovitch, E.; Javey, A. *Science* **2015,** 350, (6264), 1065-1068.
294. Palik, E. D., *Handbook of Optical Constants of Solids*. Academic Press: 1988.
295. Cataldo, G.; Beall, J. A.; Cho, H. M.; McAndrew, B.; Niemack, M. D.; Wollack, E. J. *Optics letters* **2012,** 37, (20), 4200-2.
296. Wang, X.; Lan, S. *Advances in Optics and Photonics* **2016,** 8, (4), 618-655.
297. Mao, N.; Tang, J.; Xie, L.; Wu, J.; Han, B.; Lin, J.; Deng, S.; Ji, W.; Xu, H.; Liu, K.; Tong, L.; Zhang, J. *Journal of the American Chemical Society* **2016,** 138, (1), 300-305.

Appendix A

GRAPHENE FABRICATION METHODS

Graphene Transfer (Chapters 2 – 4)

Following CVD graphene growth (or purchasing from Graphenea or Graphene Supermarket), the Cu foil is etched in iron chloride solutions, and the graphene is transferred to double-side polished oxidized Si wafers with 285 nm SiO_2 on 10 Ohm-cm Si using a poly(methyl methacrylate) (PMMA) transfer technique:

PMMA 950 A4 is spin coated on the graphene/Cu foil at 3000 rpm for 1 minute, and then baked at 180°C for 2 minutes and 30 seconds to evaporate the solvent. The graphene/Cu foil is then cut using a razor blade into squares slightly smaller than 1 cm x 1 cm. This process is done utilizing two razor blades: the first holds the foil in place (by vertically pressing it down at the position where the cut will be made), and the second cuts the foil by carefully and in slow steps making cuts working from the inside out with the corner of the blade. The foil is then placed on top of the ferric chloride etchant solution (Transene, CE-100) for approximately 20 minutes until the copper is fully removed, leaving the graphene/PMMA film floating on the surface. A plastic spoon is then used to scoop up the graphene/PMMA film and place it into a water bath, typically a 3 in diameter shallow dish. The graphene is left for ~5 minutes in the first bath, and then moved into a second for 10 minutes, and a third for 10 more minutes. Finally, the graphene is transferred by spoon into a smaller beaker of water for 20 minutes, after which it is scooped up onto the substrate of choice (in this case, 285nm SiO_2/Si chips). The water is baked off of the chip for at least 8 hours at 40 - 50°C) and then the PMMA is removed in acetone or Remover PG (Microchem) for 45 minutes. If needed, the acetone/Remove PG may be heated to 40°C to more completely remove the PMMA residue.

Electron Beam Lithography and Graphene Etch (Chapters 2 and 3):

Nanoresonator arrays are patterned in the graphene using 100 keV electron beam lithography (Raith EBPG 5000+ in Caltech's Kavli Nanoscience Institute) on 90 nm thick 950 A2 PMMA (MicroChem). The 950 A2 PMMA is spin-coated at 3000 rpm for 1 minute, and then baked for 2 minutes and 30 seconds. For very small features, a longer bake time (5 minutes) may be used. The exposed PMMA is developed in 3:1 isopropanol (IPA):methyl isobutyl ketone (MIBK) for 45 s followed by a rinse step with IPA for several seconds. The freezer in the Atwater Group labs (251a) is used to keep the MIBK cold and improve the resolution of the patterning. The pattern is etched into the graphene using oxygen plasma at 20 mTorr, a flow rate of 10 sccm, and power of 80 W for 15 s. If the plasma strikes to a high DC voltage (in excess of 50 V within 8 seconds), the etch is stopped after 11 seconds. In order to tune and monitor the carrier density of our device in situ, source and drain contacts (3 nm Cr, 100 nm Au) are deposited on the bare graphene areas adjacent to the nanoresonator arrays using a shadow mask (purchased from Photo Etch Technology), and the sample is connected in a field effect transistor (FET) configuration, with the Si layer acting as the backgate electrode.

Graphene-Gold Resonator Fabrication (Chapter 4):

Cu foil was etched away in iron chloride solution, and the graphene was transferred to a suspended SiN_x membrane obtained commercially from Norcada, part #NX10500E. A back-reflector/back-gate of 2 nm Ti/200 nm Au was evaporated on the back of the membrane by electron beam deposition. 100 keV electron beam lithography was then used to fabricate the device. First, arrays of gold resonators were patterned in 300 nm thick 950 PMMA (MicroChem) developed in cold 3:1 isopropanol:methyl isobutyl ketone (MIBK) for one minute. The sample was then etched for five seconds in a RIE oxygen plasma at 10 sccm, 20 mTorr, and 80 W to partially remove the exposed graphene and enable easier liftoff. 3 nm Ti/60 nm Au was then deposited by electron beam evaporation in the CHA (small gap sizes require a long throw distance provided only by this tool in the KNI), and liftoff was

done in acetone heated to 45°C. A second electron beam lithography step was used to define contacts of 10 nm Ti/150 nm Au. Wire bonding was done to electrically address the electrode.

For the multi-pixel device, as described in Chapter 4.2, additional aligned lithography steps are used to electrically isolate each array of gold antennas (RIE for 15 seconds, three times – not a single 45 second etch, as the striking time of the plasma is significant) and then define contacts of 10 nm Ti/150 nm Au to each pixel. Alignment marks are defined as "p20" in the EBPG: typically 10 nm Ti/100 nm Au thick, 20 μm on a side squares spaced by 1500 μm. Alignment errors are typically ~100 nm using this approach.

A p p e n d i x B

GRAPHENE ELECTROMAGNETIC SIMULATIONS

Throughout this thesis two different simulation methods have been used for graphene:

1) For most 2D simulations, we rigorously solve Maxwell's equation by using the finite element method (commercially available software, COMSOL). We model graphene as a thin film of the thickness δ and impose the relative permittivity $\varepsilon_G = 1 + 4\pi i\sigma/\omega\delta\varepsilon_0$. σ(ω) is the complex optical conductivity of graphene evaluated within the local random phase approximation from [31]. δ is chosen to be 0.1 nm which shows good convergence with respect to the $\delta \rightarrow 0$ limit. The complex dielectric function of SiO_2, ε_{SiO2} (ω), was taken from Palik.[294] The complex dielectric constant of SiN_x was fit using IR ellipsometry based on the model in ref [[295]].
2) For larger, three-dimensional simulations such as those presented in Chapter 4, we use finite difference time domain (FDTD) simulations (commercially available software, Lumerical). Graphene is modeled as a surface conductivity adapted again from ref [[174]]. We use a scattering rate of 20 fs for the graphene, which provides the optimum fit to experimental results and is consistent with previous experimental works using patterned CVD graphene on SiN_x.[190]

The agreement between approaches is excellent, and agreement to experiment is good.

Appendix C

BLACKBODY EMISSION MEASUREMENTS

For blackbody emission measurements, the device was connected to a temperature-controlled stage (Linkam) consisting of a 100 μm thick layer of sapphire on 2 mm copper on a heated silver block that can vary in temperature from room temperature to 250°C. The stage temperature was monitored via a thermocouple mounted in the silver block, and the temperature on the SiN_x membrane was confirmed to be no more than 15°C less than the thermocouple temperature by placing a series of temperature indicating laquers (Omegalaq®) on an equivalent SiN_x membrane. The device and stage were held at a pressure of 1-2 mTorr during emission measurements. Gate-dependent emission spectra were measured using a Fourier transform infrared (FTIR) microscope operating such that emitted light from the heated device passes through a KBr window and is collected in a Cassegrain objective, collimated, and passed through the interferometer in the FTIR before being focused on a liquid nitrogen-cooled HgCdTe detector. For polarization dependent measurements a wire grid polarizer was placed in the collimated beam path. As a reference a SiN_x/Au membrane was coated with an optically thick layer of black soot deposited using a candle. Soot is known to be a thermal emitter that approximates an ideal blackbody with emissivity approaching unity across the mid-IR.[117]

Appendix D

INTERFEROMETRY MEASUREMENTS

A custom built mid-IR, free-space Michelson interferometer built with collaborators at Northrop Grumman Corporation (Philip Hon, Juan Garcia) was used to characterize the electrically tunable optical reflection phase from the graphene-gold metasurface. The integrated quantum cascade laser source, MIRcat, from Daylight Solutions provided an operating wavelength range from 6.9 μm to 8.8 μm, which was a sufficiently large enough wavelength range to characterize the absorption spectra and phase of the designed metasurface. A ZnSe lens with a focal length of 75 mm was used to focus the beam onto the sample. The near-field beam waist was 2.5 mm and the far-field beam waist was 90 μm and was measured with a NanoScan beam profiler. The reference and sample legs have independent automated translations, namely, the reference mirror is mounted on a Newport VP-25XA automated linear translation stage with a typical bi-directional repeatability of +/- 50 nm and the sample stage is automated in all three dimensions to give submicron alignment accuracy with the Newport LTA-HS. The propagating beams from the sample and reference legs combine after a two inch Germanium beam splitter. Two ZnSe lenses, one with a focal length of 100 mm and another with 1000 mm image the beam at the sample plane with a ~10 times expansion. Control of the source, translation stages, pyroelectric power detector, and the Keithley source used to bias the metasurface is conducted through a Labview automation script.

Appendix E

BLACK PHOSPHORUS EXFOLIATION AND FABRICATION METHODS

Infrared Sample Preparation (Chapters 5 and 6)

Samples for infrared measurements are fabricated by mechanically exfoliating few-layer BP onto double-side polished 285 nm SiO_2/Si chips in a glove box environment. Contacts of 20 nm Ni/200 nm Au are fabricated by electron beam lithography, electron beam evaporation, and liftoff. Alignment of the contacts to the flakes is done by the patterning of four reference marks of 5nm Ti/100 nm Au in a square around the flake typically separated by 100 μm. Metal thickness for the reference marks doesn't matter as long as they are visible in the microscope with well-defined edges. An image is then taken in a confocal microscope at 50 or 100X magnification. The image is imported into AutoCAD and used as the basis for creating the contact files for electron beam lithography.

To prevent sample degradation in air (BP is sensitive to light, oxygen, and water), two different capping layers have been used:

1) PMMA 950 A8 is spin-coated at 3000 rpm for 1 minute on top of the BP and fabricated contacts in a glove box environment. 1 minute 30 seconds baking time at 180°C is sufficient to remove the solvent and protect the BO. Electrical access to the contacts is made by exposing the PMMA using electron beam lithography on top of the contacts and then wire-bonding.
2) A top gate dielectric or capping layer of 45 nm Al_2O_3 is deposited by atomic layer deposition (ALD) following the technique in ref[14]. This entails an initial 10 pulses of the Al_2O_3 precursor to saturate the surface (and protect it from the H_2O pulse that follows) followed by the deposition of 5 nm Al2O3 at 50°C following standard ALD procedures. The sample and chamber are then heated up to 150°C for the remaining 40 nm, again with standard conditions.

When top-gating is used, a semi-transparent top contact of 5 nm Ni is deposited by electron beam evaporation and liftoff. A second lithography step is used to fabricate a thicker top contact of 20 nm Ni/150 nm Au in electrical contact with the first, but with the bond pad far away from the sample that can then be wire-bonded.

Visible Sample Preparation:

Samples for visible measurements are fabricated by depositing a 5 nm thick semi-transparent back contact of Ni, followed by 45 nm Al_2O_3 by ALD on a 0.5 mm thick $SrTiO_3$ substrate. Few-layer BP is then mechanically exfoliated and a top gate and electrical contacts are fabricated as above.

Black Phosphorus Calculations:

Calculations of the optical constants of BP are based on the formalism developed in ref[231]. Optical conductivity σ is calculated using the Kubo formula within an effective low-energy Hamiltonian for different thicknesses. The permittivity is calculated as $\varepsilon(\omega) = \varepsilon_\infty + i\sigma/\omega\delta$, where δ is the thickness of the BP, and the high-frequency permittivity ε_∞ is taken from ref[296]

Identification of Crystal Axes of BP:

The x (armchair) and y (zig-zag) crystal lattice directions are determined by polarization-dependent visible reflectance measurements. At each angle of polarization an image is recorded, and pixel RGB values are sampled from both the BP flake and nearby substrate. The ratio of green channel values from flake to substrate is averaged over three sample positions, and plotted as a function of polarization angle in Figure E1. Maxima and minima in green reflectance determine the armchair and zig-zag directions, respectively.[297]

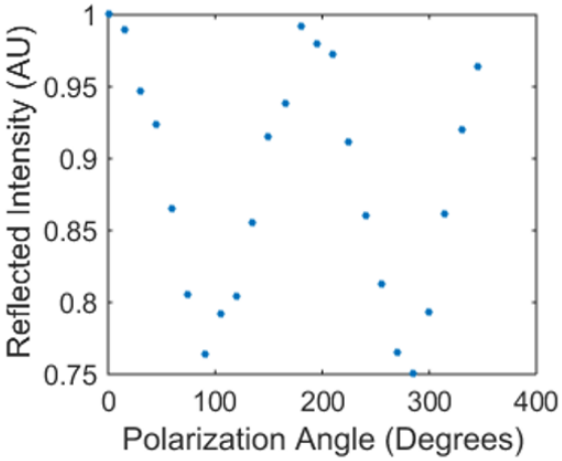

Figure E1: Intensity of the green channel of light reflected from BP flakes as the linear polarization of the incident light is rotated for the 6.5 nm flake from Chapter 5. In both cases, the polarization angle is defined as the angle between the x (armchair) crystal axis and the linear polarizer. The green component of the pixel RGB of the flakes is normalized to that of the adjacent substrate.